HELLENIC REPUBLIC

UNIVERSITY OF IOANNINA

SCHOOL OF ENGINEERING

DEPARTMENT OF MATERIALS SCIENCE AND ENGINEERING

"Synthesis and Characterization of Magnetic Nanoparticles for Applications in the Oil and Gas Industry"

Mohammed Subrati

DOCTORAL THESIS

Ioannina, January 2020

ΕΛΛΗΝΙΚΗ ΔΗΜΟΚΡΑΤΙΑ

ΠΑΝΕΠΙΣΤΗΜΙΟ ΙΩΑΝΝΙΝΩΝ

ΠΟΛΥΤΕΧΝΙΚΗ ΣΧΟΛΗ

ΤΜΗΜΑ ΜΗΧΑΝΙΚΩΝ ΕΠΙΣΤΗΜΗΣ ΥΛΙΚΩΝ

"ΣΥΝΘΕΣΗ ΚΑΙ ΧΑΡΑΚΤΗΡΙΣΜΟΣ ΜΑΓΝΗΤΙΚΩΝ ΝΑΝΟΣΩΜΑΤΙΔΙΩΝ ΓΙΑ ΕΦΑΡΜΟΓΕΣ ΣΤΗ ΒΙΟΜΗΧΑΝΙΑ ΠΕΤΡΕΛΑΙΟΥ ΚΑΙ ΑΕΡΙΟΥ"

Mohammed Subrati

ΔΙΔΑΚΤΟΡΙΚΗ ΔΙΑΤΡΙΒΗ

Ιωάννινα, Ιανουάριος 2020

Η έγκριση της διδακτορικής διατριβής από το Τμήμα Μηχανικών Επιστήμης Υλικών της Πολυτεχνικής Σχολής του Πανεπιστημίου Ιωαννίνων δεν υποδηλώνει αποδοχή των γνωμών του συγγραφέα Ν. 5343/32, άρθρο 202, παράγραφος 2.

HELLENIC REPUBLIC

UNIVERSITY OF IOANNINA

SCHOOL OF ENGINEERING

DEPARTMENT OF MATERIALS SCIENCE AND ENGINEERING

Synthesis and Characterization of Magnetic Nanoparticles for Applications in the Oil and Gas Industry

Mohammed Subrati

DOCTORAL THESIS

Ioannina, January 2020

«The approval of a Doctoral Dissertation by the Department of Materials Engineering of the University of Ioannina does not imply the acceptance of the author's opinion» (Law. 5343/32, Article 202, Paragraph 2).

Ημερομηνία αίτησης του κ. Mohammed Saleem Subrati Yadulla: 04.11.2015

Ημερομηνία ορισμού Τριμελούς Συμβουλευτικής Επιτροπής: 24.11.2015

Μέλη Τριμελούς Συμβουλευτικής Επιτροπής:

Επιβλέπων
Δημήτριος Γουρνής, Καθηγητής του Τμήματος Μηχανικών Επιστήμης Υλικών της Πολυτεχνικής Σχολής του Παν/μίου Ιωαννίνων

Μέλη
Γεώργιος Παπαβασιλείου, Διευθυντής Ερευνών του Ινστιτούτου Νανοεπιστήμης και Νανοτεχνολογίας του ΕΚΕΦΕ «Δημόκριτος»,
Saeed M. Alhassan, Associate Professor, Department of Chemical Engineering, Khalifa University of Science and Technology, Abu Dhabi.

Ημερομηνία ορισμού θέματος: 24.11.2015
«Synthesis and Characterization of Nanoparticles with Application for the Oil and Gas Industry»

ΔΙΟΡΙΣΜΟΣ ΕΠΤΑΜΕΛΟΥΣ ΕΞΕΤΑΣΤΙΚΗΣ ΕΠΙΤΡΟΠΗΣ : 346/4.12.2019

1.Δημήτριος Γουρνής, Καθηγητής του Τμήματος Μηχανικών Επιστήμης Υλικών της Πολυτεχνικής Σχολής του Πανεπιστημίου Ιωαννίνων,
2.Γεώργιος Παπαβασιλείου, Διευθυντής Ερευνών του Ινστιτούτου Νανοεπιστήμης και Νανοτεχνολογίας του ΕΚΕΦΕ «ΔΗΜΟΚΡΙΤΟΣ»,
3.Saeed M. Alhassan, Associate Professor, Department of Chemical Engineering, Khalifa University of Science and Technology, Abu Dhabi,
4.Μιχαήλ Καρακασίδης, Καθηγητής του Τμήματος Μηχανικών Επιστήμης Υλικών της Πολυτεχνικής Σχολής του Πανεπιστημίου Ιωαννίνων,
5. Αλκιβιάδης Παϊπέτης, Καθηγητής του Τμήματος Μηχανικών Επιστήμης Υλικών της Πολυτεχνικής Σχολής του Πανεπιστημίου Ιωαννίνων,
6. Γεώργιος Ρωμανός, Ερευνητής Α΄ του Ινστιτούτου Νανοεπιστήμης και Νανοτεχνολογίας του ΕΚΕΦΕ «ΔΗΜΟΚΡΙΤΟΣ»,
7. Μιχαήλ Φαρδής, Ερευνητής Α΄ του Ινστιτούτου Νανοεπιστήμης και Νανοτεχνολογίας του ΕΚΕΦΕ «ΔΗΜΟΚΡΙΤΟΣ».

Έγκριση Διδακτορικής Διατριβής με βαθμό **«ΑΡΙΣΤΑ»** στις **23.01.2020**

Ο Πρόεδρος του Τμήματος

Αλκιβιάδης Παϊπέτης
Καθηγητής

Η Γραμματέας του Τμήματος

Μαρία Κόντου

Date of application of Mr. Mohammed Saleem Subrati Yadulla: 04.11.2015

Date of appointing of Three Membered Advisory committee: 24.11.2015

Three Membered Advisory committee:

Supervisor

Dimitrios Gournis, Professor in the Department of Materials Science and Engineering, School of Engineering, University of Ioannina.

Members

George Papavassiliou, Director of Research in Institute of Nanoscience and Nanotechnology, NCSR "Demokritos",

Saeed M. Alhassan, Associate Professor in the Department of Chemical Engineering, Khalifa University of Science and Technology, Abu Dhabi.

Date of thesis definition: 24.11.2015

«Synthesis and Characterization of Nanoparticles with Application for the Oil and Gas Industry»

SEVEN MEMBERED COMMITTEE ASSIGNATION : 346/4.12.2019

1.Dimitrios Gournis, Professor in the Department of Materials Science and Engineering, School of Engineering, University of Ioannina,

2.George Papavassiliou, Director of Research in Institute of Nanoscience and Nanotechnology, NCSR "Demokritos",

3.Saeed M. Alhassan, Associate Professor in Department of Chemical Engineering, Khalifa University of Science and Technology, Abu Dhabi,

4.Michael Karakassides, Professor in the Department of Materials Science and Engineering, School of Engineering, University of Ioannina,

5.Alkiviades Paipetis, Professor in the Department of Materials Science and Engineering, School of Engineering, University of Ioannina,

6.George Romanos, Researcher A΄ in Institute of Nanoscience and Nanotechnology, NCSR "Demokritos",

7.Michael Fardis, Researcher A΄ in Institute of Nanoscience and Nanotechnology, NCSR "Demokritos".

Approval Dissertation with grade **«EXCELLENT»** on **23.01.2020**

The President of the Department

Alkiviades Paipetis
Professor

The Secretary of the Department

Maria Kontou

Abstract

Over the past three decades, superparamagnetic iron oxide nanoparticles (SPIONs) have been extensively studied as contrast agents for magnetic resonance imaging (MRI) [1-3]. This is particularly due to their unique magnetic properties, inherent biocompatibility, and low cost [4]. Despite the difference in the technological physical background, SPIONs have great potential as contrast agents for large-scale electromagnetic tomography (EMT) of oil reservoirs [5].

Conventionally, crosswell EMT is an electromagnetic imaging technique based upon measuring the difference between the electrical conductivity of reservoir fluids (i.e. oil and formation water) and other subsurface entities [6]. Alternatively, flooding the porous texture of the reservoir with stable dispersions of SPIONs would result in having an enhanced EMT contrast that is based on the altered magnetic permeability of the reservoir [5].

The research presented in this dissertation is focused on developing SPIONs that can be used as contrast agents for the large-scale imaging of reservoirs. To begin with, finite element simulations were used to validate the proposed technology using simple rules of thumb reported in the literature for the design of conventional conductivity-based crosswell EMT systems. Based upon these rules of thumb, we have successfully managed to exclusively track the anomalous response of a magnetic slug propagating in the proximity of a formation water-saturated conductive reservoir layer at audio frequencies. The effective medium theory was then employed to demonstrate the correlation of magnetic susceptibility of the injected ferrofluid with residual oil saturation and rock porosity. A laboratory-scale pilot EMT system was also implemented as an experimental proof of concept, and to verify the simulation results for the large-scale system. From the material development perspective, a facile large-scale low-cost synthesis of SPIONs is reported. The SPIONs were functionalized with citric acid as a hydrophilic ligand to enhance the

colloidal stability of the as-synthesized particles in aqueous media. The quality of the particles was examined by means of transmission electron microscopy, x-ray diffractometry, and magnetic measurements. Chemical and thermal analyses were used to examine the binding characteristics of the ligand under high-temperature conditions similar to those in reservoirs. Finally, for the ferrofluid injection strategy, a candidate aqueous carrier fluid prepared from several dilutions of seawater was considered. The optimum number of seawater dilutions required to produce a stable ferrofluid injection was determined after thoroughly studying the particle cluster-cluster aggregation kinetics in high-salinity media.

Περίληψη

Τις τελευταίες τρεις δεκαετίες, τα υπερπαραμαγνητικά νανοσωματίδια οξειδίου του σιδήρου (SPIONs) έχουν μελετηθεί εκτενώς ως παράγοντες αντίθεσης για απεικόνιση μαγνητικού συντονισμού (MRI) [1-3]. Αυτό οφείλεται ιδιαίτερα στις μοναδικές μαγνητικές τους ιδιότητες, στην εγγενή βιοσυμβατότητα και στο χαμηλό κόστος [4]. Παρά τη διαφορά στο τεχνολογικό φυσικό υπόβαθρο, τα SPIONs έχουν μεγάλες δυνατότητες ως παράγοντες αντίθεσης για ηλεκτρομαγνητική τομογραφία μεγάλης κλίμακας (EMT) δεξαμενών πετρελαίου [5].

Συμβατικά, η EMT είναι μια τεχνική ηλεκτρομαγνητικής απεικόνισης που βασίζεται στη μέτρηση της διαφοράς μεταξύ της ηλεκτρικής αγωγιμότητας των υγρών των δεξαμενών (δηλαδή του πετρελαίου και του σχηματιζόμενου νερού) και άλλες υπόγειων ουσιών [6]. Εναλλακτικά, η συσσώρευση της πορώδους υφής της δεξαμενής με σταθερές διασπορές SPIONs θα είχε ως αποτέλεσμα την αυξημένη αντίθεση EMT που βασίζεται στην μεταβαλλόμενη μαγνητική διαπερατότητα της δεξαμενής [5].

Η έρευνα που παρουσιάζεται σε αυτή τη διατριβή επικεντρώνεται στην ανάπτυξη SPIONs που μπορούν να χρησιμοποιηθούν ως παράγοντες αντίθεσης για την απεικόνιση μεγάλης κλίμακας των δεξαμενών. Κατ 'αρχάς, χρησιμοποιήθηκαν προσομοιώσεις πεπερασμένων στοιχείων για την επικύρωση της προτεινόμενης τεχνολογίας χρησιμοποιώντας απλούς κανόνες που αναφέρονται στη βιβλιογραφία για το σχεδιασμό συμβατικών συστημάτων EMT βασισμένων στην αγωγιμότητα. Με βάση αυτούς τους πρακτικούς κανόνες, καταφέραμε με επιτυχία να παρακολουθούμε αποκλειστικά την ανώμαλη απόκριση ενός μαγνητικού μετάλλου που διαδίδεται κοντά σε ένα στρώμα αγώγιμης δεξαμενής κορεσμένο με νερό σε ηχητικές συχνότητες. Στη συνέχεια χρησιμοποιήθηκε η θεωρία του αποτελεσματικού μέσου για να καταδειχθεί ο συσχετισμός της μαγνητικής επιδεκτικότητας του εγχυθέντος σιδηρο-ρευστού (ferrofluid) με τον υπολειπόμενο κορεσμό σε πετρέλαιο και το πορώδες του βράχου. Ένα πειραματικό σύστημα EMT εργαστηριακής κλίμακας εφαρμόστηκε επίσης ως πειραματική απόδειξη καθώς και για την επαλήθευση των αποτελεσμάτων προσομοίωσης για το σύστημα μεγάλης κλίμακας. Από την προοπτική ανάπτυξης υλικού, αναφέρεται μια ευέλικτη σύνθεση χαμηλού κόστους SPIONs. Τα SPIONs τροποποιήθηκαν χημικά με κιτρικό οξύ ως υδρόφιλος συνδέτης ώστε να ενισχυθεί η κολλοειδή σταθερότητα των σωματιδίων που συντέθηκαν σε υδατικά μέσα. Η ποιότητα των σωματιδίων εξετάστηκε μέσω ηλεκτρονικής μικροσκοπίας

διέλευσης, περίθλαση ακτίνων-Χ και μέσω μαγνητικών μετρήσεων. Τεχνικές χημικών και θερμικών αναλύσεων χρησιμοποιήθηκαν για να εξεταστούν τα χαρακτηριστικά σύνδεσης του συμπλοκοποιητή υπό συνθήκες υψηλής θερμοκρασίας παρόμοιες με αυτές των δεξαμενών. Τέλος, για τη στρατηγική έγχυσης σιδηρο-ρευστού (ferrofluid) εξετάστηκε ένα υποψήφιο υδατικό ρευστό που παρασκευάστηκε από διάφορες αραιώσεις θαλασσινού νερού. Οι βέλτιστες αραιώσεις θαλασσινού νερού που απαιτούνται για την παραγωγή μίας σταθερής έγχυσης σιδηρο-ρευστού (ferrofluid) προσδιορίστηκαν μετά από ενδελεχή μελέτη της κινητικής συσσωμάτωσης πλειάδων-πλειάδων (cluster-cluster) σε μέσα υψηλής αλατότητας.

Dedication

To my beloved parents **Fairouz** and **Saleem** for their endless love…

Acknowledgements

I would like to thank all those, whom without their support and contribution, the completion of this dissertation would not have been possible. First and foremost, I would like to express my deepest appreciation to my supervisor, Prof. Dimitrios Gournis, for his support, motivation, and guidance that contributed in the completion and success of this thesis. I am also grateful to him for giving me the opportunity to be part of his research group.

My sincere gratitude is reserved for my co-supervisor, Dr Georgios Papavassiliou, for his invaluable insight in developing the research presented in this dissertation, and guidance on the finite element simulations of crosswell electromagnetic tomography. It was indeed a great honor to work under his supervision, and with his team members.

I am also grateful to my co-supervisor, Dr Saeed Alhassan, for his support and patience as well as for his indispensable insights into colloidal stability.

My gratitude is also extended to Dr Michalis Fardis, for his valuable comments on editorship during the course of writing of this dissertation; and the other members of my committee, for their patience and support.

I would also like to express my immense appreciation to Dr George Mitrikas, Dr Eleni Efthimiadou, and Maria Theodosiou for assisting me with the dynamic light scattering and magnetic hyperthermia measurements.

Furthermore, I would like to acknowledge that most of the research presented in this dissertation was part of the project entitled “Magnetic Nanoparticles for Reservoir Characterization”, which was funded by Abu Dhabi National Oil Company (ADNOC).

I would like to express my gratitude to my friend, Dr Marios Katsiotis, for his indispensable care, support, and motivation throughout my Ph.D. journey. My gratitude is also extended to my friends and co-workers in Athens: Dr Lydia Gkoura, Athanasios Anastasiou, Savvas Orfanidis, Dr Nikolaos Panopoulos, Dr Marina Karagianni, Dr Vasileios Tzitzios, and Dr Despina Dermitzaki; my friends and former colleagues in Ioannina: Dr Panagiota Zygouri, Dr Antonios Kouloumpis, Dr Georgia Potsi, Dr Konstantinos Dimos, Dr Konstantinos Spyrou, Eleni Thomou, Nikolaos Chalmpes, Niki Karouta, Theodosis Giousis, Christina Gioti, Georgios Asimakopoulos, Dr Vasilios Kostas, Kyriaki-Marina Lyra, Dr Myrsini Antoniou, and Ms Souzana Pappa; and many other people I have not mentioned their names, who made my life so pleasant during these years.

Last, but certainly not least, I would like to thank my family and friends for their motivation and faith in me throughout these years. Their continued love and support have always revived my determination and persistence even in the darkest times of this journey. None of this would have been possible without them.

Table of Contents

List of Figures

List of Tables

Chapter 1

Introduction

1.1. Background and problem statement

In the last century, a variety of tracer materials have been used in groundwater hydrology and reservoir characterization for the identification of flow patterns of reservoir fluids (oil and water), flow barriers, layering, and saturation in geological formations [7-10]. These materials included insoluble powders, water-soluble dyes, as well as radioactive and non-radioactive isotopes. The vital characteristics of the "ideal tracer" include moving at the same velocity of the carrier fluid, minimum retention due to adsorption on the pores, chemical stability under harsh reservoir conditions, and detectability in minute concentrations [7].

Interwell tracer testing is an indirect in-situ reservoir characterization technique in which a fluid is tagged with a tracer material and injected to a zone of interest in the reservoir. The elution of the tracer material is then monitored at production wells as a function of time to generate tracer elution curves [7, 9]. However, matching these tracer elution curves to field data generally requires sophisticated analytical fluid flow models that account for variations in the petrophysical properties of the reservoir [7].

Electromagnetic tomography (EMT) is a novel fast functional imaging modality with viable medical and industrial applications [11, 12]. The viability of EMT for the large-scale imaging of formation conductivity has been well-researched over the last three decades with the increasing emphasis on reservoir characterization, and the desire to monitor dynamic reservoir processes in secondary and tertiary production [13].

Crosswell EMT is a direct in-situ reservoir characterization technique that is used to image the electrical conductivity distribution between boreholes. The conductivity provides information about the rock porosity and fluid saturation distributions via Archie's law. Variations in the conductivity distribution over time during fluid injection correspond to the variations in the fluid mobility within the rock matrix, which ultimately correspond to variations in permeability [14]. Nevertheless, the applicability of crosswell EMT is limited when the boreholes are steel-cased. Steel casing is typically eight orders-of-magnitude more conductive than the rock surrounding the borehole. Consequently, the high-frequency electromagnetic (EM) waves, which are needed to resolve the formation conductivity distribution in the interwell region undergo severe attenuation as they propagate through the steel casings of the transmitting and receiving boreholes [13, 14].

Alternatively, at low frequencies, the sensitivity of EMT surveys to magnetic heterogeneities significantly dominates that to conductive heterogeneities [5]. Therefore, in this work, we propose the deployment of low-frequency magnetic permeability-based EMT systems utilizing aqueous ferrofluids (i.e. stable colloidal dispersions of submicron magnetic particles), the latter which will be injected into the reservoir resulting in a magnetic permeability-based contrast as illustrated in Figure 1.1. As can be seen in Figure 1.1, the reservoir rock (i.e. background rock matrix) has a magnetic permeability of μ_1. As it propagates toward the observation well, the injected ferrofluid will increase the magnetic permeability of the zone of interest (shaded in black) from μ_1 to μ_2. The transmitted low-frequency primary field (red streamlines) will magnetize the zone of interest, and hence inducing a secondary field (blue streamlines). The electromagnetic attenuation of the primary field due to the secondary field will be detected by the receivers positioned in the observation well.

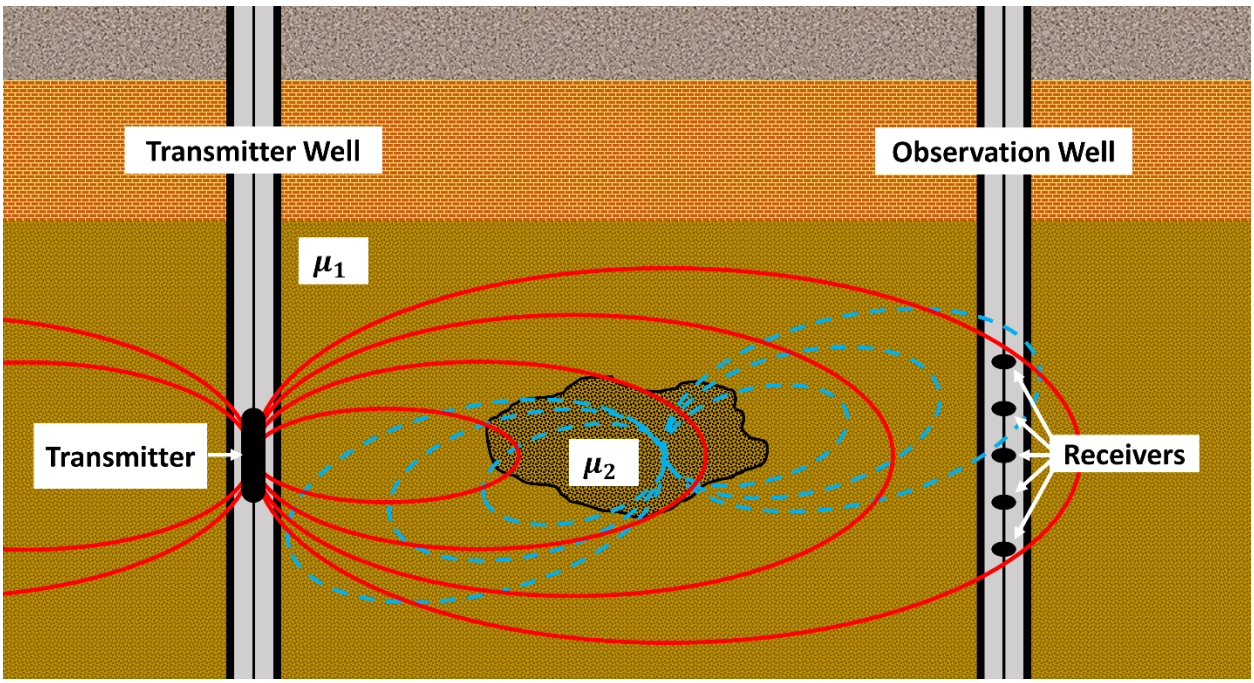

Figure 1.1 The proposed crosswell EMT method.

1.2. Research aims

The research presented in this dissertation is primarily aimed at developing hydrophilic magnetic nanoparticles (MNPs), which can be used as contrast agents for large-scale imaging of reservoirs. Moreover, this research is also aimed at determining the ferrofluid injection strategy as well as the optimum design parameters of the crosswell EMT system required to maximize the detectability of the MNPs during the course of ferrofluid propagation.

1.3. Research methodology and objectives

Due to the interdisciplinary nature of this research, an integrated top-down approach consisting of three hierarchical levels, as depicted in Figure 1.2, was developed and implemented. In the first level, a thorough theoretical overview of electromagnetic wave propagation in isotropic

lossy dielectric media is presented, which is aimed at introducing the concept of electromagnetic attenuation in addition to highlighting the role of skin depth as a design parameter. The second level includes a technical review of the rules of thumb reported in the literature for the design of conventional crosswell EMT systems. This is followed by finite element simulations of the proposed crosswell EMT utilizing the same design rules of thumb. A pilot EMT system was also implemented for verification of the simulation results. The third level covers the synthesis and characterization aspects of the candidate MNPs. Finally, this is followed by inspecting the aggregation kinetics of the developed MNPs in high-salinity media. This objective is aimed at determining the optimum number of seawater dilutions required to produce a stable injection fluid, and this is precisely where the novelty of this work lies.

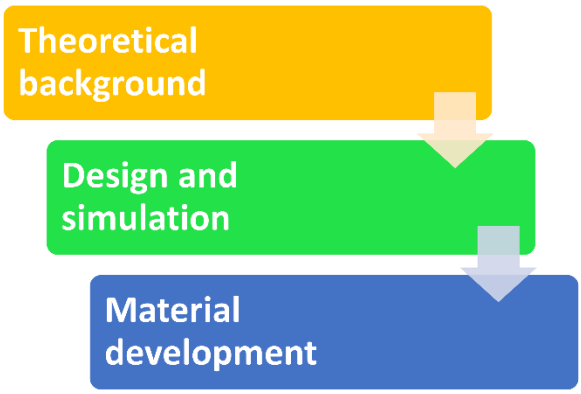

Figure 1.2 The proposed and implemented research methodology.

Chapter 2

Electromagnetic Wave Propagation

2.1. Introduction

The viability of the crosswell EMT technique is primarily judged by the propagation of the electromagnetic waves (EM waves) in rock formations. In order to understand how the propagation of EM waves influences the design of crosswell EMT systems, first we need to understand the theoretical background of the *classical theory of electromagnetic radiation*, which was formulated by the Scottish scientist James Clerk Maxwell based upon his famous *Maxwell's equations* [15]. Maxwell's theoretical work on electromagnetic radiation was later confirmed by the German physicist Heinrich Hertz through experiments with radio waves [16]. Table 2.1 shows the differential forms of Maxwell's equations where **D**, ρ_v, **B**, **E**, **H**, and **J** are the electric displacement field, volume charge density, magnetic flux density, electric field, magnetic field, and current density vector, respectively.

Table 2.1 Generalized differential forms of Maxwell's equations [17].

Equation (differential form)	**Equation #**	**Remarks**
$\nabla \cdot \mathbf{D} = \rho_v$	(Equation 2.1)	Gauss's law
$\nabla \cdot \mathbf{B} = 0$	(Equation 2.2)	Nonexistence of magnetic monopoles (Gauss's law for magnetic fields)
$\nabla \times \mathbf{E} = -\frac{\partial \mathbf{B}}{\partial t}$	(Equation 2.3)	Faraday's law
$\nabla \times \mathbf{H} = \mathbf{J} + \frac{\partial \mathbf{D}}{\partial t}$	(Equation 2.4)	Ampère's circuital law

The following constitutive relations

$$\mathbf{D} = \varepsilon \mathbf{E} \qquad \text{(Equation 2.5)}$$

$$\mathbf{B} = \mu \mathbf{H} \qquad \text{(Equation 2.6)}$$

$$\mathbf{J} = \sigma \mathbf{E} + \rho_v \mathbf{u} \qquad \text{(Equation 2.7)}$$

hold for static and time-harmonic fields, given that ε, μ, and σ, are the absolute permittivity, magnetic permeability, and electrical conductivity of the medium, respectively; and $\mathbf{u}$ is the wave propagation velocity.

2.2. Time-harmonic fields

Time-harmonic fields vary periodically or sinusoidally with time, and they can be easily expressed in a more practical form in terms of phasors [17]. A phasor is a complex number that contains the amplitude and phase of a sinusoidal oscillation. For example, in a rectangular (or Cartesian) form, a phasor $\mathbf{z}$ can be expressed as

$$\mathbf{z} = \mathbf{x} + j\mathbf{y} \qquad \text{(Equation 2.8)}$$

where $j = \sqrt{-1}$, and $\mathbf{x}$ and $\mathbf{y}$ are the real (Re) and imaginary (Im) parts of $\mathbf{z}$, respectively. Moreover, since the phase φ of $\mathbf{z}$ is given by

$$\varphi = \tan^{-1}\frac{\mathbf{y}}{\mathbf{x}} \qquad \text{(Equation 2.9)}$$

then $\mathbf{z}$ can be expressed in a polar form as follows

$$\mathbf{z} = re^{j\varphi} = r(\cos\varphi + j\sin\varphi) \qquad \text{(Equation 2.10)}$$

where r is the magnitude of $\mathbf{z}$, that is

$$r = |\mathbf{z}| = \sqrt{\mathbf{x}^2 + \mathbf{y}^2} \qquad \text{(Equation 2.11)}$$

Figure 1 illustrates the two phasor forms (Cartesian and polar) of a $\mathbf{z}$-field oscillating at an angular frequency of ω. It is worth noting that $\mathbf{x}$, $\mathbf{y}$, $\mathbf{z}$, r, and φ should not be confused with coordinate variables.

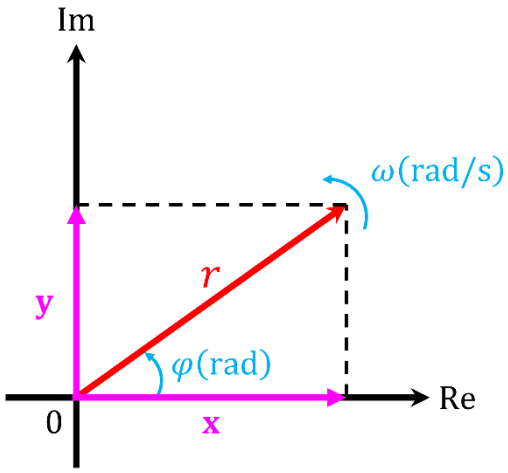

Figure 2.1 Cartesian and polar representation of a phasor.

The *time element* is defined as

$$\varphi = \omega t + \theta \qquad \text{(Equation 2.12)}$$

where θ is the *phase shift*, which can be a constant or a function of space coordinates and/or time. Substituting Equation 2.12 into Equation 2.10 yields

$$re^{j(\omega t+\theta)} = re^{j\theta}e^{j\omega t} \qquad \text{(Equation 2.13)}$$

and it follows that

$$\mathrm{Re}\left(re^{j\varphi}\right) = r\cos(\omega t + \theta) \qquad \text{(Equation 2.14)}$$

$$\mathrm{Im}\left(re^{j\varphi}\right) = r\sin(\omega t + \theta) \qquad \text{(Equation 2.15)}$$

Now, let's consider the following sinusoidal AC current with an amplitude of I_0:

$$I(t) = I_0\cos(\omega t + \theta)$$

A phasor form of the instantaneous current $I(t)$ analogous to Equation 2.13 can be expressed as follows

$$I(t) = I_0 e^{j\theta} e^{j\omega t} = I_s e^{j\omega t}$$

where I_s is the phasor current, and hence it can be deduced that

$$I(t) = \mathrm{Re}\left(I_s e^{j\omega t}\right)$$

In general, a phasor is a complex quantity and could be either a scalar or a vector. If a vector $\mathbf{A}(x, y, z, t)$ is a time-harmonic field, then the phasor form of $\mathbf{A}$ is $\mathbf{A}_s(x, y, z)$; the two quantities are related as follows

$$\mathbf{A}(x, y, z, t) = \mathrm{Re}\left[\mathbf{A}_s(x, y, z) e^{j\omega t}\right] \qquad \text{(Equation 2.16)}$$

and it can be shown that

$$\frac{\partial \mathbf{A}}{\partial t} = \frac{\partial}{\partial t}\mathrm{Re}\left(\mathbf{A}_s e^{j\omega t}\right) = \mathrm{Re}\left(j\omega \mathbf{A}_s e^{j\omega t}\right) = j\omega \mathbf{A}_s \qquad \text{(Equation 2.17)}$$

Using the same analogy in Equation 2.16, the differential forms of Maxwell's equations (Equations 2.1-2.4) scan now be expressed in their phasor forms as shown in Table 2.2.

Table 2.2 Generalized phasor forms of Maxwell's equations.

Equation (phasor form)	**Equation #**
$\nabla \cdot \mathbf{D}_s = \rho_{vs}$	(Equation 2.18)
$\nabla \cdot \mathbf{B}_s = 0$	(Equation 2.19)
$\nabla \times \mathbf{E}_s = -j\omega \mathbf{B}_s$	(Equation 2.20)
$\nabla \times \mathbf{H}_s = \mathbf{J}_s + j\omega \mathbf{D}_s$	(Equation 2.21)

2.3. Wave propagation in homogenous lossy dielectric media

EM waves lose power as they propagate through lossy dielectric media [17]. Wave propagation in lossy dielectric media is classically considered as a general case from which other special cases can be derived as we will see in the next section. In this context, let's consider a linear, isotropic, homogenous, lossy dielectric medium that is charge-free ($\rho_v = 0$). Using the phasor forms of Maxwell's equations and Equations 2.5-2.7, it can be shown that

$$\nabla \cdot \mathbf{E}_s = 0 \qquad \text{(Equation 2.22)}$$

$$\nabla \cdot \mathbf{H}_s = 0 \qquad \text{(Equation 2.23)}$$

$$\nabla \times \mathbf{E}_s = -j\omega\mu \mathbf{H}_s \qquad \text{(Equation 2.24)}$$

$$\nabla \times \mathbf{H}_s = (\sigma + j\omega\varepsilon)\mathbf{E}_s \qquad \text{(Equation 2.25)}$$

Taking the curl of both sides of Equation 2.24 yields

$$\nabla \times \nabla \times \mathbf{E}_s = -j\omega\mu(\nabla \times \mathbf{H}_s) \qquad \text{(Equation 2.26)}$$

Applying the vector identity

$$\nabla \times (\nabla \times \mathbf{A}) = \nabla(\nabla \cdot \mathbf{A}) - \nabla^2\mathbf{A}$$

to the left-hand side of Equation 2.26 yields

$$\nabla(\nabla \cdot \mathbf{E}_s) - \nabla^2\mathbf{E}_s = -j\omega\mu(\nabla \times \mathbf{H}_s) \qquad \text{(Equation 2.27)}$$

Substituting Equations 2.22 and 25 into Equation 2.27 yields

$$\nabla^2\mathbf{E}_s = j\omega\mu(\sigma + j\omega\varepsilon)\mathbf{E}_s \qquad \text{(Equation 2.28)}$$

Equation 2.28 can be rewritten as follows

$$\boxed{\nabla^2\mathbf{E}_s - \gamma^2\mathbf{E}_s = 0} \qquad \text{(Equation 2.29)}$$

where

$$\gamma^2 = -\omega^2\mu\varepsilon + j\omega\mu\sigma \qquad \text{(Equation 2.30)}$$

and γ, in reciprocal meters, is called the *propagation constant* of the medium. In a similar procedure, it can be shown that for the **H**-field,

$$\boxed{\nabla^2\mathbf{H}_s - \gamma^2\mathbf{H}_s = 0} \qquad \text{(Equation 2.31)}$$

Equations 2.29 and 2.31 are known as homogeneous vector *Helmholtz's equations*, or simply, vector *wave equations*.

Since γ in these equations is a complex quantity, we may let

$$\gamma = \alpha + j\beta \qquad \text{(Equation 2.32)}$$

We obtain α and β from Equations 2.30 and 2.32 by noting that

$$\gamma^2 = (\alpha + j\beta)^2 = (\alpha^2 - \beta^2) + j(2\alpha\beta) \qquad \text{(Equation 2.33)}$$

$$|\gamma^2| = \sqrt{(\alpha^2 - \beta^2)^2 + (2\alpha\beta)^2} = \alpha^2 + \beta^2 \qquad \text{(Equation 2.34)}$$

By comparing Equations 2.33 and 2.34 with Equation 2.30, it can be deduced that

$$-\mathrm{Re}(\gamma^2) = \beta^2 - \alpha^2 = \omega^2\mu\varepsilon \qquad \text{(Equation 2.35)}$$

$$|\gamma^2| = \beta^2 + \alpha^2 = \omega\mu\sqrt{(\omega\varepsilon)^2 + \sigma^2} \qquad \text{(Equation 2.36)}$$

and by simultaneously solving Equations 2.35 and 2.36 we obtain

$$\alpha = \omega\sqrt{\frac{\mu\varepsilon}{2}\left[\sqrt{1 + \left(\frac{\sigma}{\omega\varepsilon}\right)^2} - 1\right]} \qquad \text{(Equation 2.37)}$$

$$\beta = \omega\sqrt{\frac{\mu\varepsilon}{2}\left[\sqrt{1 + \left(\frac{\sigma}{\omega\varepsilon}\right)^2} + 1\right]} \qquad \text{(Equation 2.38)}$$

Conventionally, α is referred to as *attenuation* or *decay constant*, and β is known as *phase constant* or *wavenumber*.

Now, let's consider the case of an EM wave propagating in an unbounded medium. In Cartesian coordinates, we can assume that the wave is propagating in the *z*-direction (along the $\mathbf{a}_z$ unit vector), and its **E**-field has only an *x*-component that does not vary with x and y, and hence

$$\mathbf{E}_s = E_{s,x}(z)\,\mathbf{a}_x \qquad \text{(Equation 2.39)}$$

Substituting Equation 2.39 into Equation 2.29 yields

$$(\nabla^2 - \gamma^2)E_{s,x}(z) = 0$$

$$\frac{\partial^2 E_{s,x}(z)}{\partial x^2} + \frac{\partial^2 E_{s,x}(z)}{\partial y^2} + \frac{\partial^2 E_{s,x}(z)}{\partial z^2} - \gamma^2 E_{s,x}(z) = 0 \qquad \text{(Equation 2.40)}$$

and since $E_{s,x}(z)$ does not vary with x and y;

$$\frac{\partial^2 E_{s,x}(z)}{\partial x^2} = \frac{\partial^2 E_{s,x}(z)}{\partial y^2} = 0$$

Equation 2.40 becomes

$$\left[\frac{d^2}{dz^2} - \gamma^2\right] E_{s,x}(z) = 0 \qquad \text{(Equation 2.41)}$$

Equation 2.41 is a linear homogeneous differential equation with a solution that can be expressed as follows

$$E_{s,x}(z) = E_0 e^{-\gamma z} + E_0' e^{\gamma z} \qquad \text{(Equation 2.42)}$$

where E_0 and E_0' are constants. The only boundary condition that can be deduced from Equation 2.42 is

$$E_{s,x}(z) \to \infty \quad \text{as} \quad z \to \infty$$

and hence E_0' must be set to zero. Equation 2.42 now becomes

$$E_{s,x}(z) = E_0 e^{-\gamma z} \quad \text{(Equation 2.43)}$$

Substituting Equation 2.32 into Equation 2.43 yields

$$E_{s,x}(z) = E_0 e^{-\alpha z} e^{-j\beta z} \quad \text{(Equation 2.44)}$$

In order to apply the phasor identity (Equation 2.16), we need to multiply both sides of Equation 2.44 by the time factor $e^{j\omega t}$ and the unit vector $\mathbf{a}_x$. This yields

$$\mathbf{E}_x(z,t) = \text{Re}\left[E_{s,x}(z)\, e^{j\omega t}\mathbf{a}_x\right] = \text{Re}\left[E_0 e^{-\alpha z} e^{j(\omega t - \beta z)}\mathbf{a}_x\right] \quad \text{(Equation 2.45)}$$

Applying the phasor identity (Equation 2.14) to Equation 2.45 yields

$$\mathbf{E}_x(z,t) = E_0 e^{-\alpha z} \cos(\omega t - \beta z)\, \mathbf{a}_x \quad \text{(Equation 2.46)}$$

Conventionally, $t = 0$ is arbitrarily selected as a reference for a wave, and hence Equation 2.46 finally becomes

$$\boxed{\mathbf{E}(z) = E_0 e^{-\alpha z} \cos(-\beta z)\, \mathbf{a}_x} \quad \text{(Equation 2.47)}$$

Equation 2.47 can be interpreted verbally as a single-component (x-component) **E**-field propagating periodically in the z-direction with a period of $2\pi/\beta$ and an amplitude E_0 decaying exponentially by a factor of α.

It can be deduced from Maxwell-Faraday equation (Equation 2.3) that both **E** and **H** time-harmonic fields (or EM waves) are always normal to the direction of wave propagation. This means that the fields lie in a plane that is orthogonal (or transverse) to the direction of wave propagation. They form an EM wave that has no **E** and **H** field components along the direction of propagation, such a wave is called a *transverse electromagnetic wave*. Therefore, the **H**-field

corresponding to the **E**-field in Equation 2.47 can be obtained by solving Equation 2.31 following steps similar to those in Equations 2.39-2.45, but in the transverse direction (along $\mathbf{a}_y$), which will eventually lead us to

$$\mathbf{H}_y(z,t) = \mathrm{Re}\left[H_0 e^{-\alpha z} e^{j(\omega t - \beta z)} \mathbf{a}_y\right] \qquad \text{(Equation 2.48)}$$

H_0 can be expressed in terms of E_0 as follows

$$H_0 = \frac{E_0}{\eta} \qquad \text{(Equation 2.49)}$$

where η is a complex quantity known as the *intrinsic impedance* (in ohms) of the medium, which is defined as

$$\eta = |\eta| e^{j\theta_\eta} \qquad \text{(Equation 2.50)}$$

with

$$|\eta| = \frac{\sqrt{\mu/\varepsilon}}{\left[1 + \left(\frac{\sigma}{\omega\varepsilon}\right)^2\right]^{1/4}} \qquad \text{(Equation 2.51)}$$

and

$$\tan 2\theta_\eta = \frac{\sigma}{\omega\varepsilon} \qquad \text{(Equation 2.52)}$$

where $0 \le \theta_\eta \le 45°$. Substituting Equations 2.49-2.51 into Equation 2.48 yields

$$\mathbf{H}_y(z,t) = \mathrm{Re}\left[\frac{E_0}{|\eta|} e^{-\alpha z} e^{j(\omega t - \beta z - \theta_\eta)} \mathbf{a}_y\right] = \frac{E_0}{|\eta|} e^{-\alpha z} \cos\left(\omega t - \beta z - \theta_\eta\right) \mathbf{a}_y \qquad \text{(Equation 2.53)}$$

Finally, by taking $t = 0$ as a reference, Equation 2.53 becomes

$$\boxed{\mathbf{H}(z) = \frac{E_0}{|\eta|} e^{-\alpha z} \cos\left(-\beta z - \theta_\eta\right) \mathbf{a}_y} \qquad \text{(Equation 2.54)}$$

It can be implied from Equations 2.47 and 2.54 that the electric and magnetic fields of an EM wave propagating in a lossy dielectric medium are always out-of-phase by θ_η due to the intrinsic impedance of the medium. In the next section, we will see how the intrinsic impedance and dielectric loss in a material are interrelated.

2.4. Approximations

It is worth mentioning that in lossy dielectric media, ε varies in a complex way with frequency, and this can be best explained with the aid of Equation 2.25;

$$\nabla \times \mathbf{H}_s = j\omega\varepsilon \left(1 - j\frac{\sigma}{\omega\varepsilon}\right) \mathbf{E}_s = j\omega\varepsilon_c \mathbf{E}_s$$

Here, ε_c is the complex permittivity, which can be expressed as follows

$$\varepsilon_c(\omega) = \varepsilon \left(1 - j\frac{\sigma}{\omega\varepsilon}\right) = \varepsilon'(\omega) - j\varepsilon''(\omega) \qquad \text{(Equation 2.55)}$$

where $\varepsilon = \varepsilon'(\omega)$ is the frequency-dependent *real permittivity*, and $\varepsilon''(\omega) = \sigma/\omega$ is the frequency-dependent *imaginary permittivity* representing dielectric loss. The real permittivity of a medium is defined as

$$\varepsilon'(\omega) = \varepsilon_r(\omega)\, \varepsilon_0 \qquad \text{(Equation 2.56)}$$

where $\varepsilon_r(\omega)$ and ε_0 are the frequency-dependent *complex relative permittivity*, and *vacuum permittivity* ($\varepsilon_0 = 8.85\times10^{-12}$ F/m), respectively.

The dielectric loss, which is often parameterized as the *loss tangent* $\tan\theta_e$ or the corresponding *loss angle* θ_e, quantifies the inherent dissipation of electromagnetic radiation in a dielectric material in the form of heat, and it can be expressed in terms of the phase shift due to intrinsic impedance (θ_η) as follows

$$\tan\theta_e = \frac{\varepsilon''(\omega)}{\varepsilon'(\omega)} = \frac{\sigma}{\omega\varepsilon} = \tan 2\theta_\eta \qquad \text{(Equation 2.57)}$$

In the following sections, we will present two cases for the loss tangent, which are often considered in the design of crosswell EMT systems.

2.4.1. Wave-regime approximation

The *wave-regime approximation* is a condition used to describe the propagation of an extremely high-frequency EM wave in a medium. However, a more generic definition can be interpreted in terms of the loss tangent as $\sigma \ll \omega\varepsilon$, which also corresponds to free space or perfect dielectric medium ($\sigma \to 0$). Applying this condition to Equations 2.37, 2.38, and 2.52 yields

$$\boxed{\alpha = 0} \qquad \text{(Equation 2.58)}$$

$$\boxed{\beta = \omega\sqrt{\mu\varepsilon}} \qquad \text{(Equation 2.59)}$$

and

$$\tan 2\theta_\eta = 0 \Rightarrow \boxed{\theta_\eta = 0} \qquad \text{(Equation 2.60)}$$

The electric and magnetic fields corresponding to the conditions specified in Equations 2.58-2.60 are illustrated in Figure 2.2. Note that both fields become in-phase in the wave-regime approximation as $\theta_\eta = 0$.

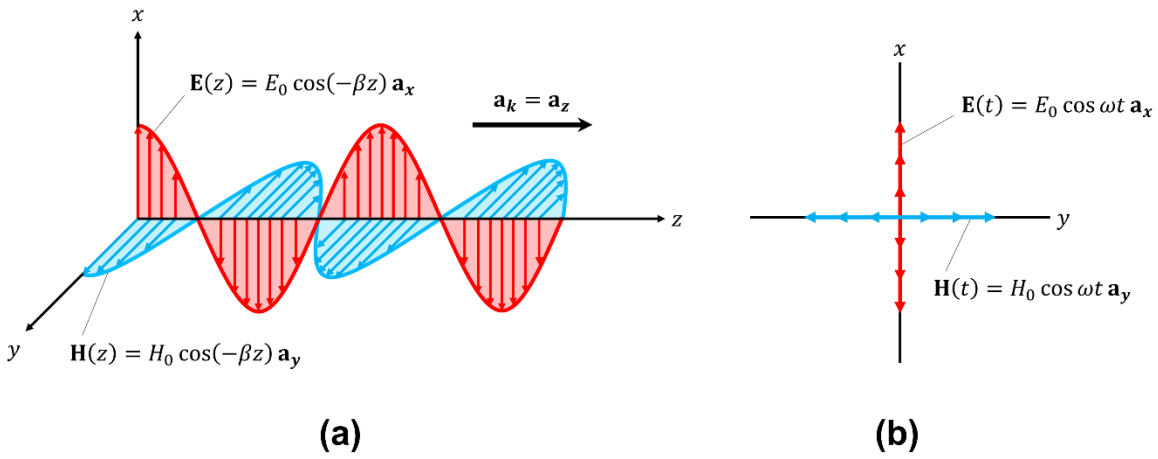

Figure 2.2 Plots of $\boldsymbol{E}$ and $\boldsymbol{H}$ for a transverse EM wave propagating in the z-direction: (a) as functions of z at t=0 ($\boldsymbol{a}_k$ is the unit vector of the direction of propagation), and (b) at z=0.

Taking $\omega = 2\pi f$ where f is the wave frequency in Hertz (Hz), Equation 2.59 becomes

$$\boxed{\beta = 2\pi f\sqrt{\mu\varepsilon}} \qquad \text{(Equation 2.61)}$$

The magnitude of the wave propagation velocity (*phase velocity*) u is defined as

$$u = \frac{\omega}{\beta} \qquad \text{(Equation 2.62)}$$

Substituting Equation 2.59 into Equation 2.62 yields

$$u = \frac{1}{\sqrt{\mu\varepsilon}} \qquad \text{(Equation 2.63)}$$

and given that $\mu = \mu_r \mu_0$ and $\varepsilon = \varepsilon_r(\omega)\, \varepsilon_0$ where μ_r is the relative magnetic permeability of the medium ($\mu_r = \varepsilon_r = 1$ for vacuum/free space by definition); and μ_0 is the vacuum magnetic permeability ($\mu_0 = 4\pi \times 10^{-7}$ H/m), Equation 2.63 becomes

$$\boxed{u = \frac{c}{\sqrt{\mu_r \varepsilon_r(\omega)}} \quad , \quad c = \frac{1}{\sqrt{\mu_0 \varepsilon_0}}} \qquad \text{(Equation 2.64)}$$

where c is the speed of light in free space ($c \cong 3 \times 10^8$ m/s).

2.4.2. Quasi-static approximation

As the name suggests, the *quasi-static approximation* is a condition used to describe the propagation of an extremely low-frequency EM wave in a medium, and hence it can be interpreted in terms of the loss tangent as $\sigma \gg \omega\varepsilon$, which also corresponds to a perfect or good conducting medium ($\sigma \to \infty$). Applying this condition to Equations 2.37, 2.38, and 2.52 yields

$$\boxed{\alpha = \beta = \sqrt{\frac{\omega\mu\sigma}{2}} = \sqrt{\pi f \mu \sigma}} \qquad \text{(Equation 2.65)}$$

and

$$\tan 2\theta_\eta \to \infty \Rightarrow \boxed{\theta_\eta = 45°} \qquad \text{(Equation 2.66)}$$

It can be implied from Equations 2.47, 2.54, and 2.66 that in the quasi-static approximation, the **H**-field of a transverse EM wave, at any time, lags the **E**-field by 45°.

The phase speed of a transverse EM wave in the quasi-static approximation can be obtained by substituting Equation 2.65 into Equation 2.62;

$$\boxed{u = \sqrt{\frac{2\omega}{\mu\sigma}} = \sqrt{\frac{4\pi f}{\mu\sigma}}} \qquad \text{(Equation 2.67)}$$

It is worth noting that both Equations 2.64 and 2.67 imply that different frequency components in a transverse EM wave travel with different velocities causing what is known as *dispersion*.

2.5. Frequency of operation and skin depth

When designing an EMT system, the *frequency of operation* (i.e. frequency of the transmitted EM waves) is determined by the desired depth of EM wave propagation, magnetic field intensity at the transmitter location, and sensitivity of the receiver [18]. The desired depth of EM wave propagation is often parameterized as the *skin depth* δ, that is the distance at which the amplitude of a propagating transverse EM wave has decayed by a factor of e^{-1} (~37% of its original value). Therefore, applying the definition of skin depth to either Equation 2.47 or Equation 2.54 yields

$$e^{-\alpha\delta} = e^{-1}$$

and hence we obtain

$$\delta = \frac{1}{\alpha} \qquad \text{(Equation 2.68)}$$

Substituting Equation 2.65 into Equation 2.68 yields

$$\boxed{\delta = \frac{1}{\sqrt{\pi f \mu\sigma}} \cong \frac{503}{\sqrt{f\mu_r\sigma}}} \qquad \text{(Equation 2.69)}$$

Figure 2.3 shows how the *background conductivity* (i.e. conductivity of the rock formation) and frequency of operation are related to skin depth as per Equation 2.69. The *wave propagation* region is where the wave-regime approximation is applicable ($\sigma \ll \omega\varepsilon$) and displacement currents are dominant, whereas the *diffusion process* region is where the quasi-static approximation is applicable ($\sigma \gg \omega\varepsilon$) and conduction currents are dominant. The dashed line shows the boundary between the two regions, that is when $\sigma \to \omega\varepsilon$ (for carbonate rocks: $\varepsilon_r \cong 6$).

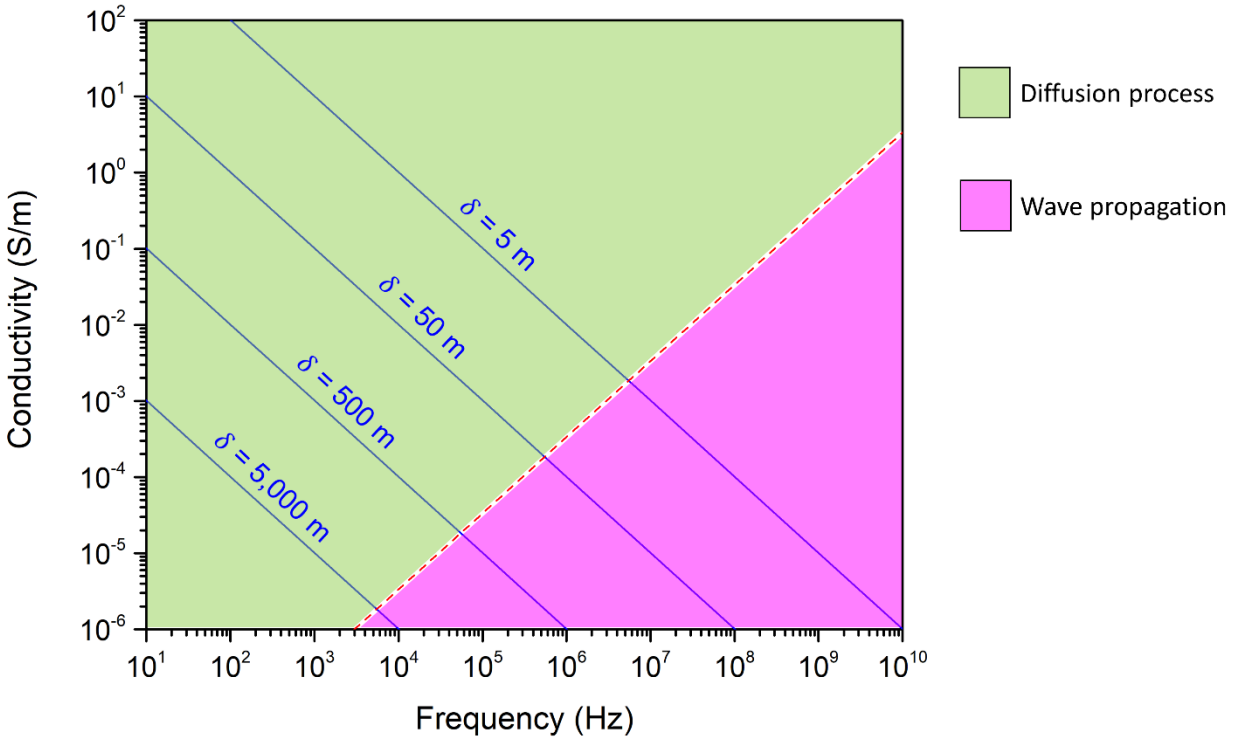

Figure 2.3 Skin depth as a function of background conductivity and operating frequency.

Because the typical conductivities of carbonate sedimentary rocks (e.g. dolomite and limestone) vary between 10^{-5} and 10^{-3} S/m (see Figure 2.4), and the desired depth of EM wave propagation is 500 m; therefore, our interest will be solely in the diffusion process region with operating frequencies of 10 kHz and below.

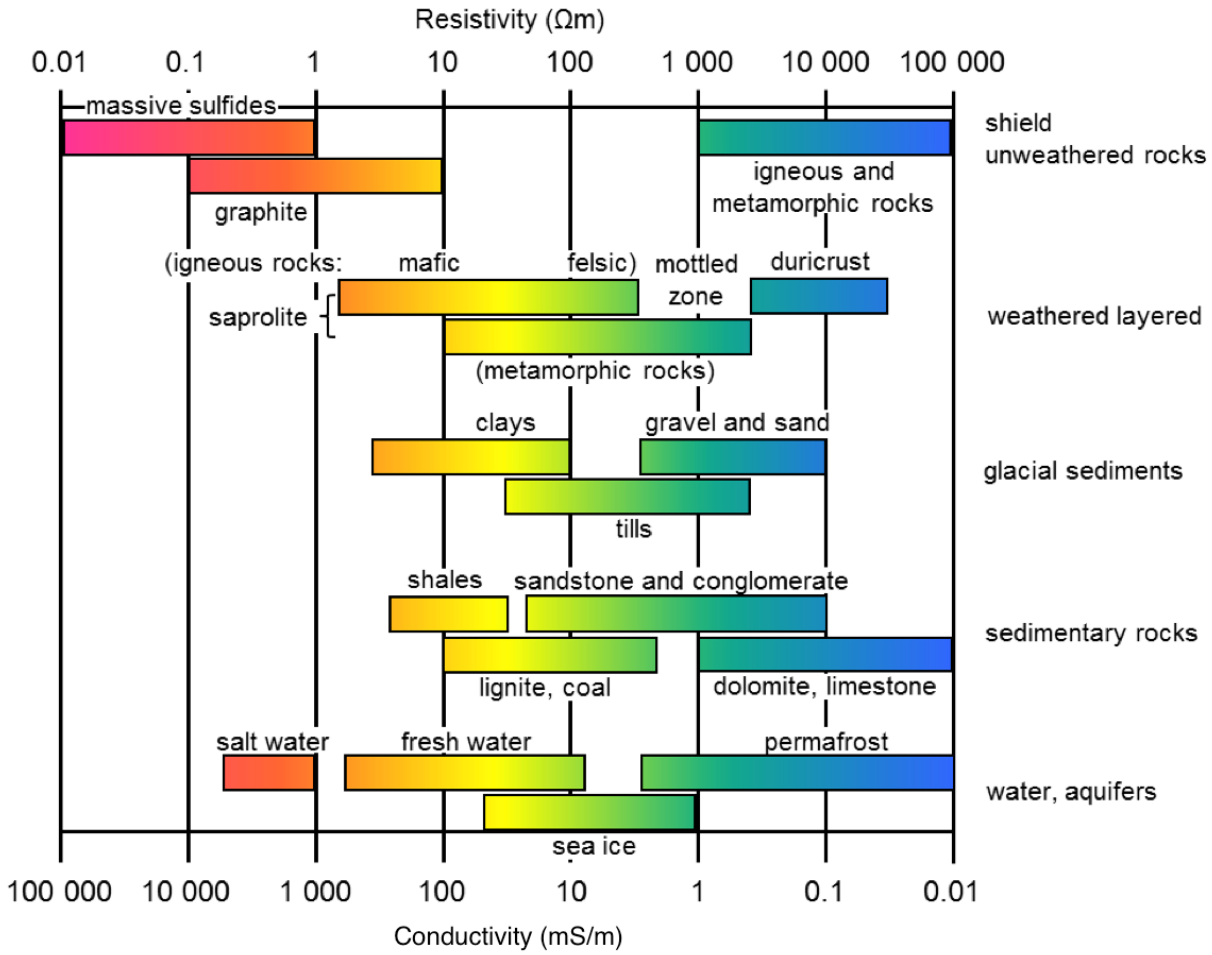

Figure 2.4 Electrical conductivity and resistivity of common rocks [19].

Chapter 3

Design and Simulation of a Crosswell Electromagnetic Tomography System for the Tracking of Propagating Magnetic Slugs in Reservoirs

3.1. Introduction

Crosswell electrical and EM methods can be classified into three categories: DC electrical resistivity measurements, high-frequency EM propagation techniques, and low-frequency inductive methods. The crosswell resistivity method is only applicable in open-hole or perforated plastic-cased wells. High-frequency EM techniques in the radio-frequency range (typically the MHz range) are particularly attractive because standard tomographic reconstruction techniques can be applied in interpretation, and resolution in the sub-meter range can often be obtained. However, the high attenuation encountered at high frequencies due to conductive heterogeneities in geological formations precludes the application of such techniques to most petroleum exploration and development problems. Therefore, in order to increase the depth of investigation in conductive environments, lower frequencies must be employed, which can be achieved by low-frequency inductive methods [13].

In the previous chapter, we showed that a skin depth of 500 m in carbonate sedimentary rock formations is attainable only if we operate in the diffusion process region at audio frequencies of 10 kHz and below. However, skin depth is not a practical parameter to rely on when designing crosswell systems as it does not take into account the optimum transmitter dipole moment and

receiver sensitivity. Therefore, in this chapter, we will first present the criteria for designing a conventional EMT crosswell system using simple methods developed by Brian Spies and Michael Wilt earlier in the 1990s [13, 19]. This will be followed by finite element simulations of a crosswell system for the imaging of a propagating magnetic slug in a carbonate rock formation using the COMSOL Multiphysics® software. A pilot EMT system was implemented in order to verify the results obtained from the finite element simulations of the large-scale system.

3.2. Background and design considerations

A typical crosswell EMT system consists of a *transmitting well* and another *observation well*, which are separated by a crosswell distance L as illustrated in Figure 3.1. The transmitter section in the transmitting well consists of a multi-turn coil antenna with a high-permeability core, an AC current source to power the coil, and a winch-cable system for borehole deployment. The receiver section in the observation well consists of a commercial sensor attached to a winch-cable system, and a commercial synchronous detector, which uses the optically coupled transmitter current signal as a reference for measurements [19]. In this chapter, we will be referring to the transmitting solenoid as the *transmitter*, and the sensor-synchronous detector setup as the *receiver*.

There are two types of EM fields that are encountered in any crosswell EMT system, namely *primary* and *secondary fields*. Primary fields are those broadcasted by the transmitter, and measured in the presence of a conductive background rock formation, which we will be referring to as the *background*. It is worth noting that background conductivity (σ_b) is an anisotropic property, meaning that it varies with spatial coordinates [20]. Nevertheless, since our interest is

merely in the crosswell imaging of carbonate sedimentary rocks; hence, in this study we will be assuming a homogeneous limestone background with an isotropic conductivity of 1.00×10^{-4} S/m. Secondary fields often arise from conductive heterogeneities that are embedded the background in the form of brine-saturated regions. This is because at significantly high frequencies primary fields induce eddy currents within conductive heterogeneities, and these currents, in turn, induce secondary fields. However, in our case, secondary fields arise particularly due the induced magnetization in the ferrofluid-saturated region of interest, which we will be introducing in the background as illustrated in Figure 3.1.

Interference of primary and secondary magnetic fields yields a *total magnetic field* whose vertical component (H_z) is measured by the receiver inside the observation well borehole [19, 21]. Total fields become comparable to primary fields when secondary fields are extremely weak. In the next sections, we will describe the criteria for designing a crosswell EMT system using a mathematical model for H_z adapted from John D. Jackson [22].

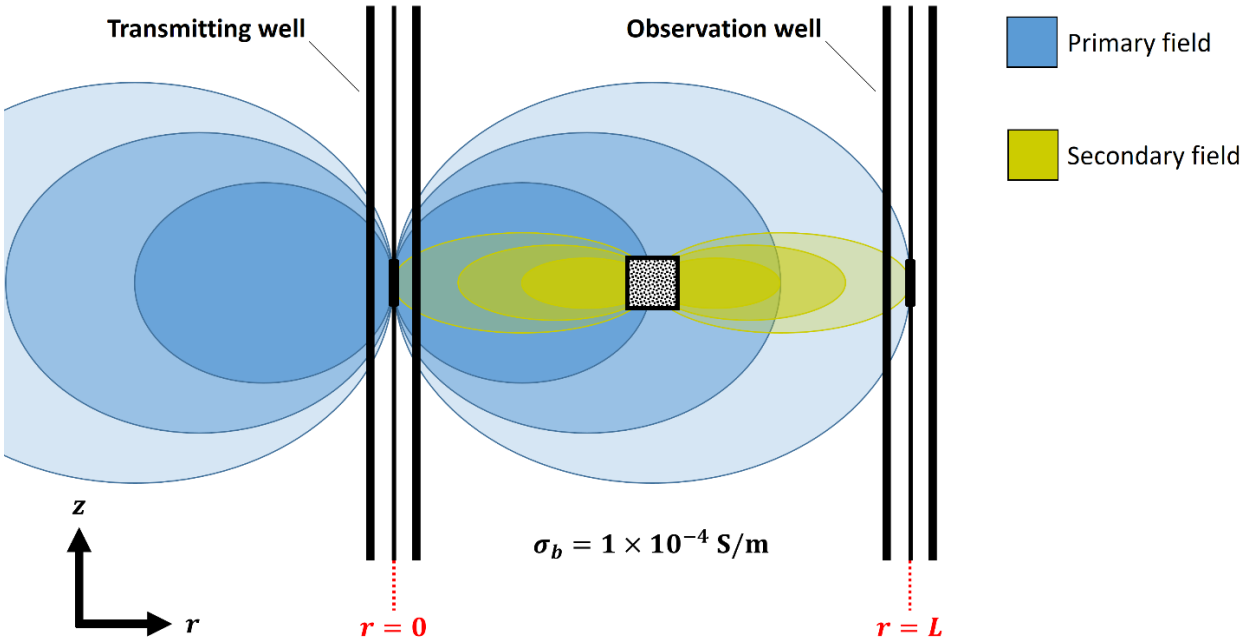

Figure 3.1 Schematic diagram of a basic crosswell EMT system with a limestone background. An observation well is located at a radial distance L from the transmitting well.

3.2.1. Minimum frequency of operation

For coplanar transmitting vertical magnetic dipole (VMD) and receiver located at the same depth, H_z is given by

$$H_z(r) = \frac{-M}{4\pi r^3} e^{-jk_b r}(1 + jk_b r - k_b^2 r^2) \qquad \text{(Equation 3.1)}$$

Here, r is the radial distance from the transmitter, M is the transmitter dipole moment, and k_b is the propagation constant of the background medium, which is given by

$$k_b = \sqrt{\omega^2 \mu_b \varepsilon_b - j\omega\mu_b\sigma_b} \qquad \text{(Equation 3.2)}$$

where μ_b and ε_b are the background magnetic permeability and permittivity ($\mu_b = \mu_0 = 4\pi\times10^{-7}$ H/m for a nonmagnetic background), respectively. For earth materials at subradio frequencies, the first term of Equation 3.2 is always dominated by the second term [19]. Thus, one could express k_b in terms of frequency of operation (f) as follows

$$k_b = \sqrt{-2\pi j\mu_b\sigma_b f} \qquad \text{(Equation 3.3)}$$

The $k_b^2 r^2$ term in Equation 3.1 could be expressed in terms of the dimensionless parameter Γ_b as follows

$$k_b^2 r^2 = -2\pi j\Gamma_b \qquad \text{(Equation 3.4)}$$

where Γ_b is conventionally referred to as the *background induction number*, and is given by

$$\Gamma_b = \mu_b\sigma_b f r^2 \qquad \text{(Equation 3.5)}$$

A dimensionless form of H_z could be expressed as follows

$$\overline{H_z} = \frac{-4\pi r^3 H_z}{M} \qquad \text{(Equation 3.6)}$$

Substituting Equations 3.4 and 3.6 into Equation 3.1 yields

$$\overline{H_z} = e^{-j\sqrt{-2\pi j\Gamma_b}}\left(1 + j\sqrt{-2\pi j\Gamma_b} + 2\pi j\Gamma_b\right) \qquad \text{(Equation 3.7)}$$

Figure 3.2 shows the log-log absolute-value plots of the real and imaginary parts of $\overline{H_z}$ versus Γ_b. For values of Γ_b less than 0.01, the total field is effectively equivalent to its free-space value. Measurements in this range contain no information on the background conductivity, yet they can be useful in calibrating the system, and correcting for errors in the transmitter-receiver geometry

[13] . In this regard, the value Γ_b = 0.01 puts an effective lower limit on the frequency of operation. In our case, the minimum frequency of operation for a crosswell distance of 500 m can be calculated using Equation 3.5 as follows

$$f_{\min} = \frac{0.01}{\mu_b \sigma_b L^2} = \frac{0.01}{(4\pi \times 10^{-7}\ \mathrm{H\ m^{-1}})(1 \times 10^{-4}\ \mathrm{S\ m^{-1}})(500\ \mathrm{m})^2} \cong 318\ \mathrm{Hz}$$

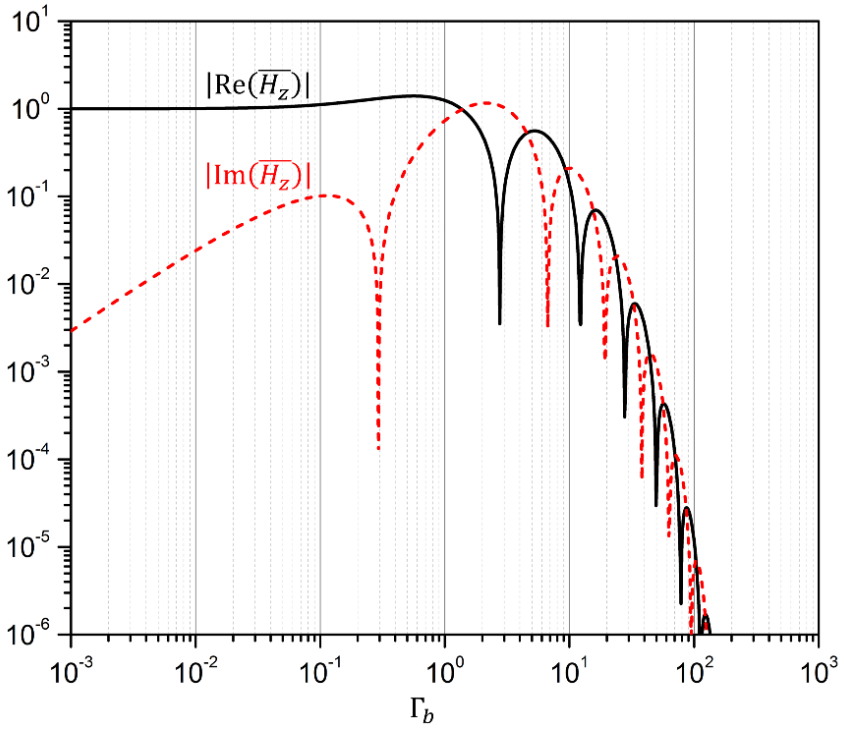

Figure 3.2 Log-log absolute-value plots of the real and imaginary parts of $\overline{H_z}$ displayed as a function of Γ_b.

3.2.2. Maximum frequency of operation

The total magnetic flux density (B_z) corresponding to the total magnetic field H_z is given by

$$B_z = \mu_b H_z \qquad \text{(Equation 3.8)}$$

Figure 3.3 shows the log-log plots of the magnitude of B_z versus L for four orders of magnitude of $f_{\min}$, and a transmitter dipole moment of 1 kA·m^2. We are assuming here a maximum receiver sensitivity that is equal to an instrumental noise floor of 10^{-10} nT, a value which was chosen for consistency with the literature [19]. As can be seen in Figure 3.3, crosswell imaging can be effectively performed at crosswell distance of 500 m with a maximum frequency of operation of 3.18 MHz.

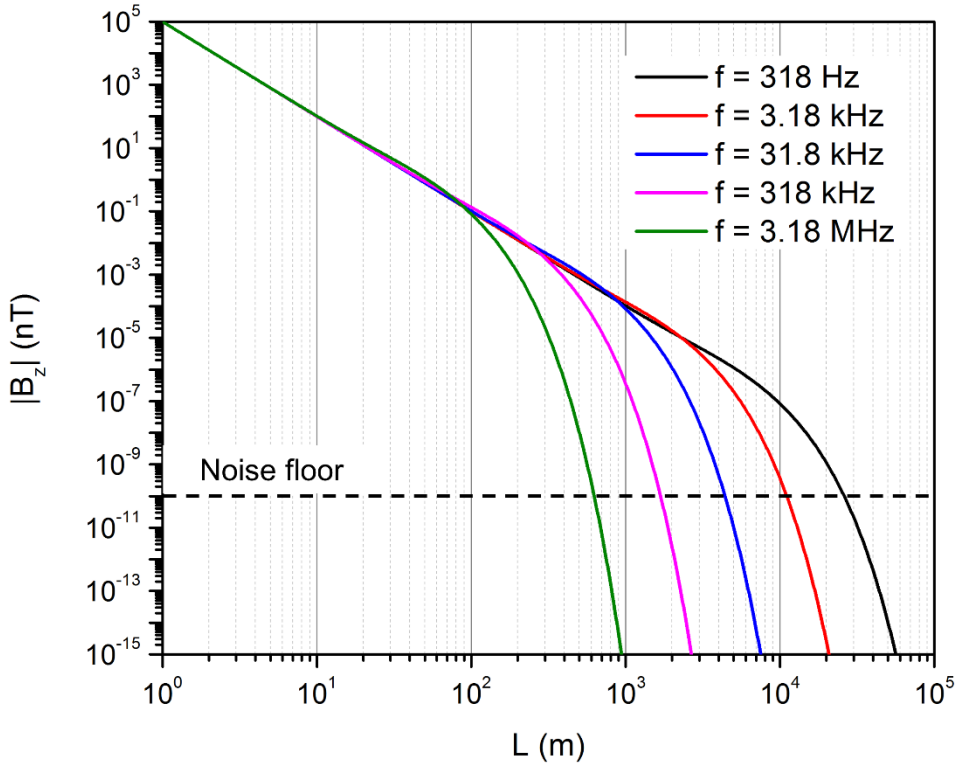

Figure 3.3 Log-log plots of the magnitude of B_z versus L for a limestone background with a conductivity of 1.00×10^{-4} S/m. The transmitter dipole moment used here is 1 kA·m^2 with a corresponding instrumental noise floor of 10^{-4} nT. The plots display the initial characteristic r^{-3} fall-off of B_z in free space, which is followed by the frequency-dependent exponential decay.

3.3. Finite element simulations

Our crosswell EMT model consists of a 2D axisymmetric computational domain that extends vertically from -325 m to 325 m, and radially to a distance of 650 m. The computation domain contains an *infinite element domain* with a thickness of 100 m to emulate the unbounded domain condition. A transmitting VMD point with a moment of 1 $kA \cdot m^2$ is positioned along the axis of symmetry. Point receivers are positioned vertically at a radial distance of 500 m. The vertical position (*z*-position) of the transmitter is parametrically swept from -125 m to 125 m with a step size of 2.5 m in order to locate 101 transmitting points. Analogically, the corresponding coplanar 101 receiving points are located in the same vertical transmitting range with the same step size.

3.3.1. Petrophysical properties and considerations

In this study, we are assuming a homogeneous limestone background isotropic conductivity of 1.00×10^{-4} S/m. The gas saturation within the rock formation is assumed to be zero. A conductive anomaly is embedded in the background in the form of a brine-saturated reservoir layer extending radially from 50 m to 450 m, and vertically from -100 m to -50 m. This layer is assumed to increase the rock conductivity by a factor of ten.

A dense ferrofluid (i.e. magnetic slug) is injected into another reservoir layer extending radially from 50 m to 450 m, and vertically from -25 m to 25 m. The slug-saturated region, which we will be referring to as the *magnetic anomaly*, is 50 m in height and width, and these dimensions are assumed to remain conserved as the slug radially propagates towards the observation well in an incompressible flow and a piston-like transport. The slug is assumed to increase the magnetic permeability of the rock initially by a factor of two. The magnetic permeability of the magnetic anomaly was decreased with the course of propagation to emulate the retention of magnetic

nanoparticles in the pores due to adsorption. Figure 3.4 shows a schematic of our computational model.

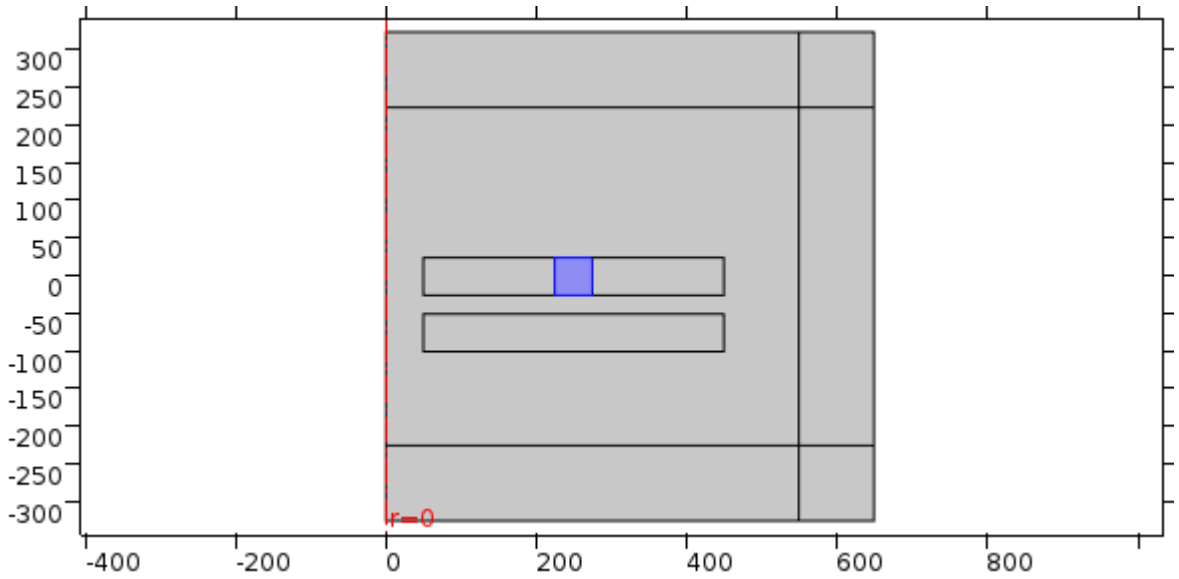

Figure 3.4 Schematic of the simulated crosswell EMT model. For the sake of illustration, the magnetic anomaly (highlighted in blue) is positioned in the middle of the crosswell distance (at r = 250 m).

3.3.2. Physical background and methodology

The magnetic vector potential ($\mathbf{A}$) at a spherical radial distance r from a point VMD is given by

$$\mathbf{A} = \frac{\mu_0}{4\pi}\frac{\mathbf{m_z} \times \hat{\mathbf{r}}}{r^3} \qquad \text{(Equation 3.9)}$$

where $\mathbf{m_z}$ is the VMD moment along the z axis ($\mathbf{m_z}$ = 1 kA·m^2), and $\hat{\mathbf{r}}$ is the spherical radial unit vector [23]. However, since our model is 2D axisymmetric, COMSOL automatically evaluates Equation 3.9 in cylindrical geometry. All simulations were performed by solving Ampère's law in the frequency domain (Equation 2.21) for $\mathbf{A}$ given that the electric field ($\mathbf{E}$), magnetic field ($\mathbf{H}$), and magnetic flux density ($\mathbf{B}$) are defined as follows

$$\mathbf{E} = -j\omega\mathbf{A} \qquad \text{(Equation 3.10)}$$

and

$$\mathbf{B} = \mu\mathbf{H} = \nabla \times \mathbf{A} \qquad \text{(Equation 3.11)}$$

All the simulations were performed at three frequencies: 318 Hz, 3.18 kHz, and 3.18 MHz.

The amplitude (or magnitude) of B_z was calculated in COMSOL as follows

$$B_{z0} = \sqrt{[\mathrm{Re}(B_z)]^2 + [\mathrm{Im}(B_z)]^2} \qquad \text{(Equation 3.12)}$$

where $\mathrm{Re}(B_z)$ and $\mathrm{Im}(B_z)$ are the real and imaginary parts of B_z, respectively. The crosswell EMT surveys were conducted by calculating B_{z0} for multiple combinations of the z-positions of the transmitting and receiving points, and hence yielding an array of B_{z0}, which could be expressed as follows

$$B_{z0} = [b_{ij}] \equiv \begin{bmatrix} b_{11} & \cdots & b_{1j} \\ \vdots & \ddots & \vdots \\ b_{i1} & \cdots & b_{ij} \end{bmatrix} \qquad \text{(Equation 3.13)}$$

where i and j (not to confuse with the imaginary unit j) are the indices corresponding to the transmitting and receiving points, respectively. Arrays of B_{z0} were plotted in MATLAB yielding contour plots of B_{z0} with respect to the z-positions of the transmitting and receiving points. These plots help us visualize the influence of electromagnetic anomalies on the propagation of the transmitted transverse EM waves across the crosswell plane.

The combinations of the z-positions of the transmitting and receiving points are often schematically displayed in the literature as *ray paths* connecting the transmitting and receiving

points as illustrated in Figure 3.5 [24]. Physically, each ray path represents the distance travelled by a transmitted transverse EM wave across the crosswell plane.

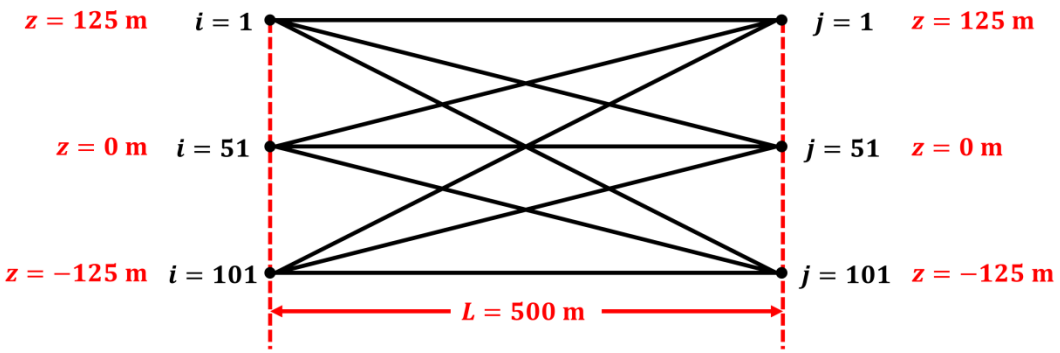

Figure 3.5 Schematic of a symmetric crosswell EMT survey.

3.4. Results and discussion

3.4.1. Influence of the conductive layer

The first step in the crosswell imaging of the propagating magnetic slug is to quantitatively identify the influence of the conductive brine-saturated layer embedded in the background. Figure 3.6 shows the contour plots of B_{z0} for the background (i.e. without the slug) for the aforementioned frequencies. At 318 Hz, B_{z0} is highest along the points on the diagonal, which correspond to the shortest ray path (i.e. when both the transmitter and receiver are located at the same depth). The absence of an anomalous response along the diagonal region implies a negligible attenuation of the transmitted EM waves as they propagate through the conductive layer at 318 Hz. The anomalous response becomes evident at 3.18 kHz and severe at 3.18 MHz, which is expected as more eddy currents are induced within the conductive layer with increasing frequency as can be seen in Figure 3.8. The attenuation due to the secondary field arising from the induced eddy currents can be clearly seen in Figure 3.9. The resistive losses generated by eddy currents are shown in Figure 3.10.

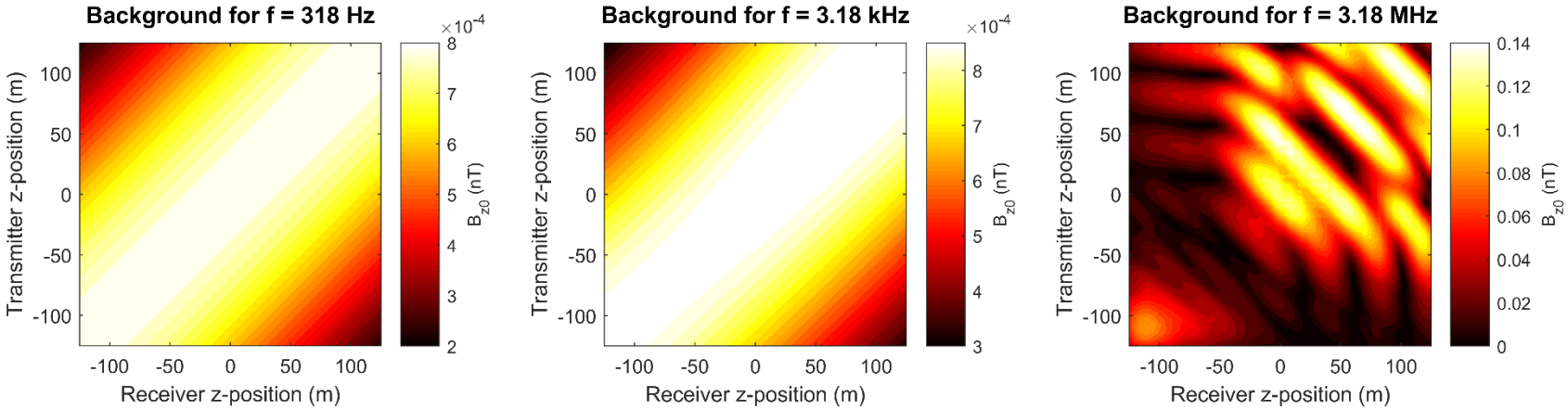

Figure 3.6 B_{z0} contour plots for the background at different frequencies. The blue square depicts the vertical boundaries of the conductive layer.

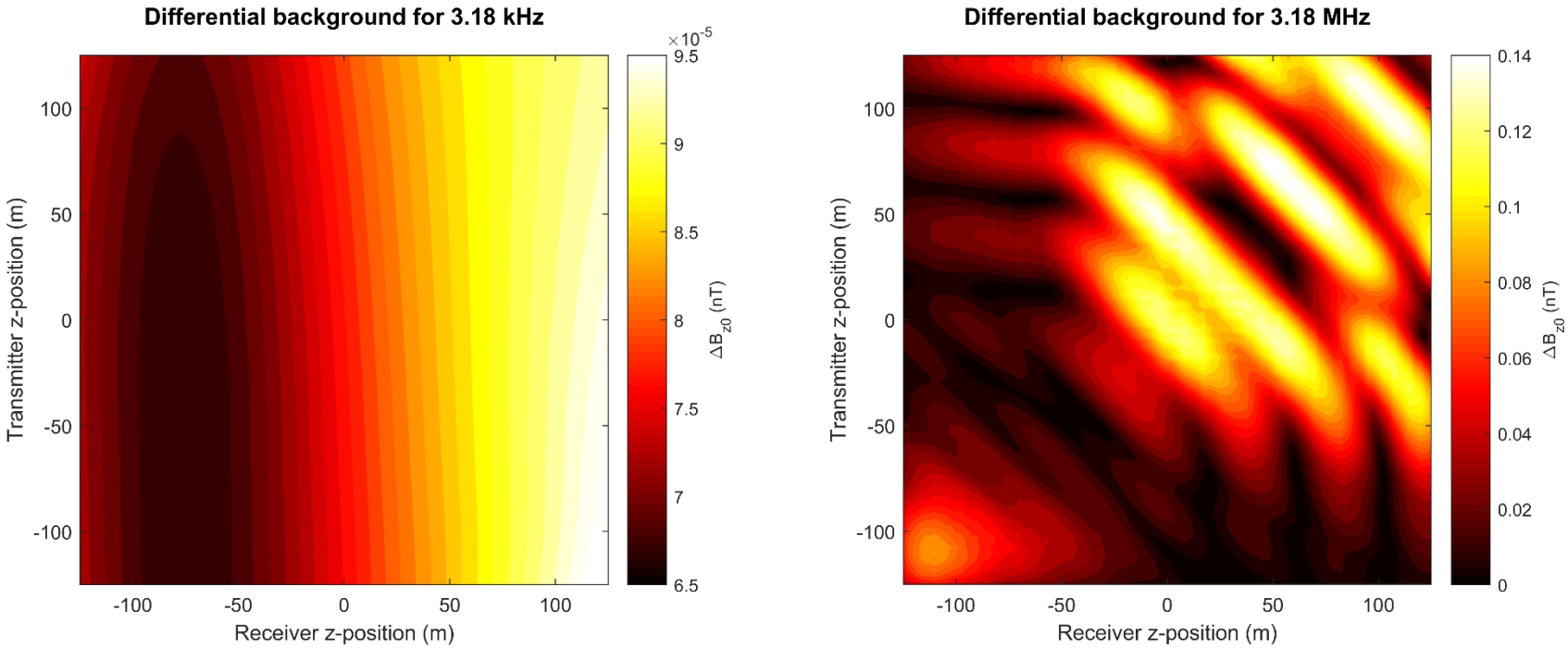

Figure 3.7 Differential B_{z0} contour plots for the background (*differential backgrounds*) at 3.18 kHz and 3.18 MHz taking the background at 318 Hz as the *reference background* for subtraction.

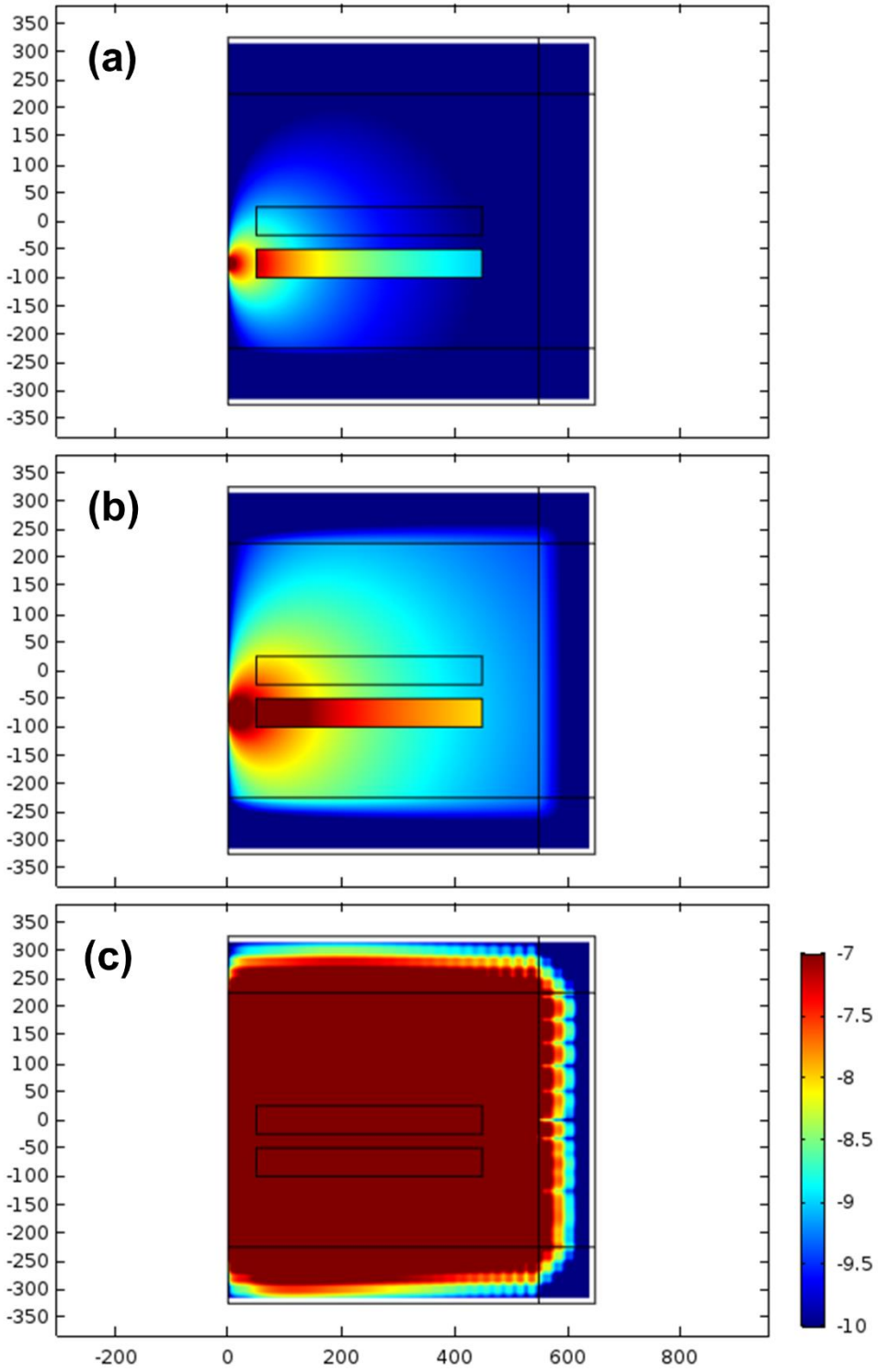

Figure 3.8 Eddy currents induced within the conductive layer at 318 Hz (a), 3.18 kHz (b), and 3.18 MHz (c). The color bar displays the logarithmic scale of induced current density in A/m^2.

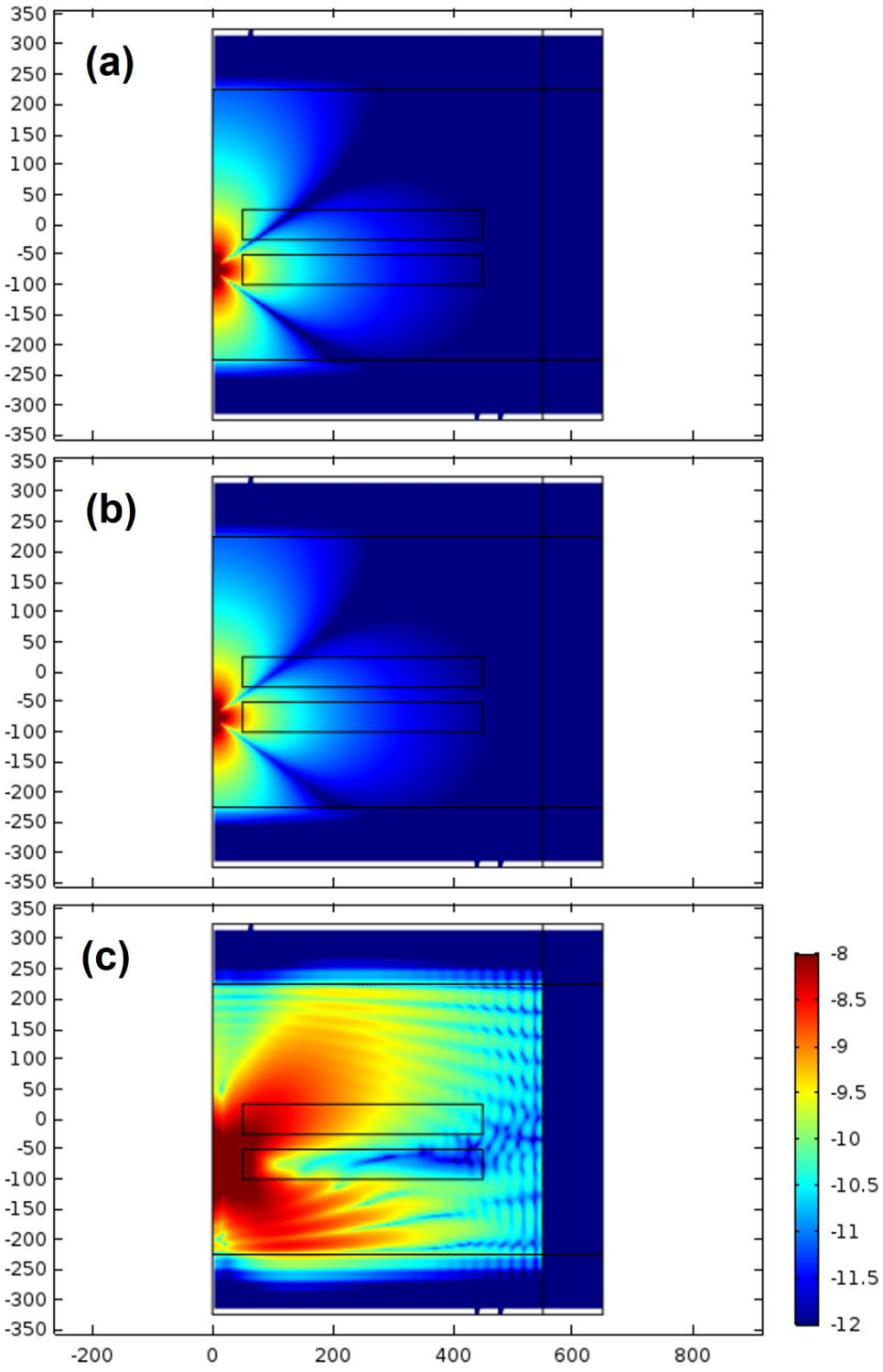

Figure 3.9 2D map of B_{z0} at 318 Hz (a), 3.18 kHz (b), and 3.18 MHz (c). The color bar displays the logarithmic scale in Tesla (T). The fields in (a) and (b) are almost equivalent to the primary field (i.e. negligible secondary field).

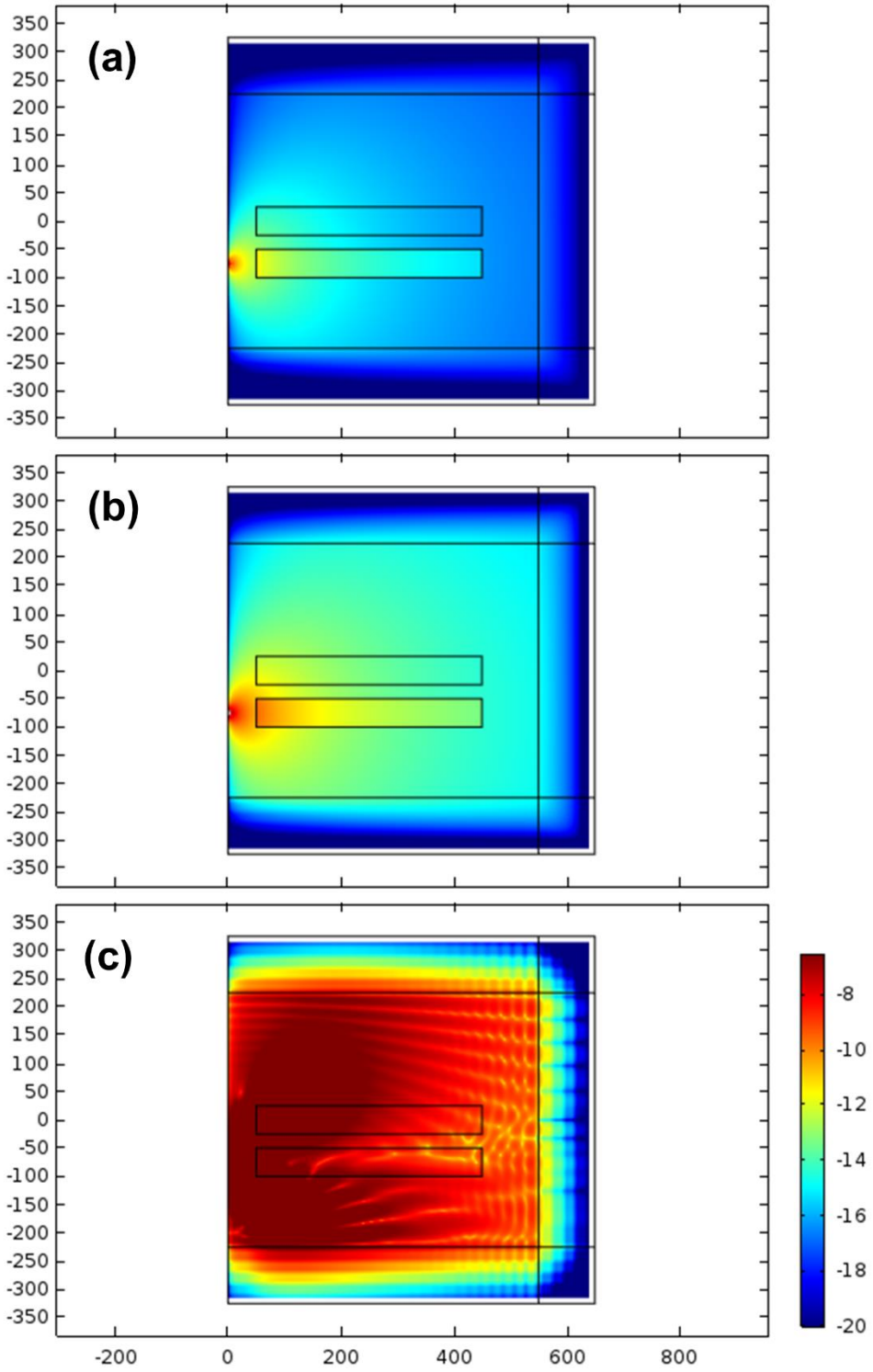

Figure 3.10 Resistive losses generated by the induced eddy currents at 318 Hz (a), 3.18 kHz (b), and 3.18 MHz (c). The color bar displays the logarithmic scale in W/m^3.

3.4.2. Influence of the magnetic slug

After ascertaining the electromagnetic contribution of the conductive layer, we can now proceed to investigating the influence of the magnetic slug as it propagates through the reservoir towards the observation well. Figures 3.11-3.13 show the contour plots of B_{z0} for different radial positions of the magnetic anomaly and at the same aforementioned frequencies. As can be seen in Figure 3.11, the anomalous response of the slug at 318 Hz can be observed between the transmitter and receiver z-positions of -25 to 25 m, which in fact correspond to the dimensions of the magnetic anomaly. The response is strongest when the slug is in close proximity to the transmitter, decreases in the middle of the crosswell distance, and then slightly increases as the slug is in close proximity to the receiver. However, the response seems to slightly shift to lower z-positions at 3.18 kHz as can be seen in Figure 3.12. This can be attributed to the interference with the secondary field arising from the eddy currents generated within the conductive layer at 3.18 kHz, which becomes highly dominant at 3.18 MHz as can be seen in Figure 3.13. Moreover, it can be inferred from the differential contour plots (after background subtraction) of B_{z0} in Figures 3.14-3.16 that the secondary field due to the magnetization of the propagating slug dominates the one generated by the induced eddy currents within the conductive layer at audio frequencies of 10 kHz and below.

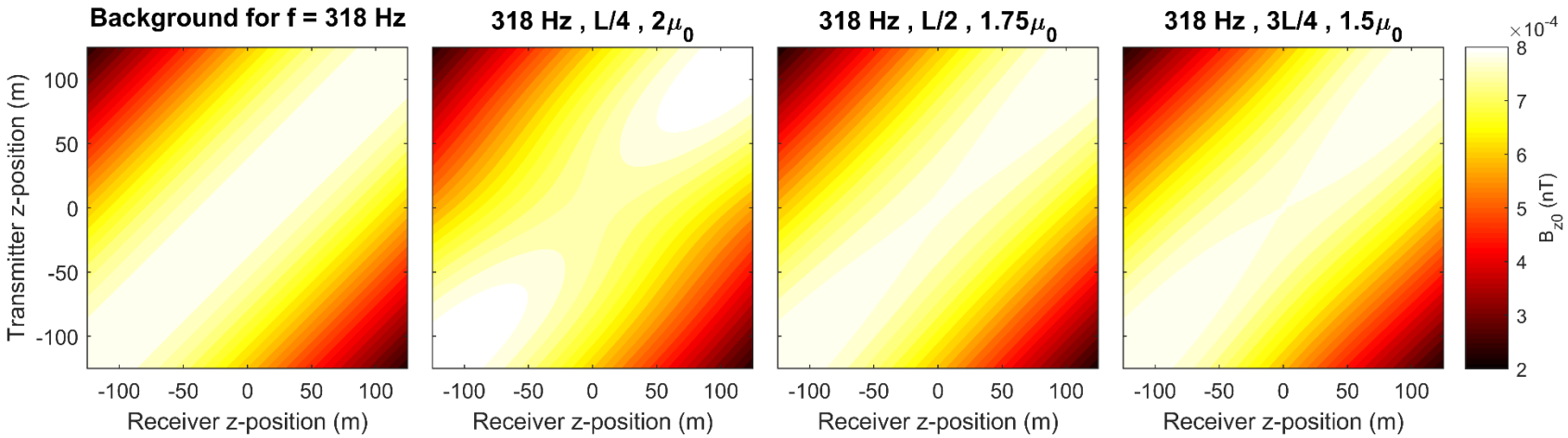

Figure 3.11 B_{z0} contour plots for the background without and with the magnetic slug at 318 Hz. The radial position of the magnetic anomaly is displayed in terms of the crosswell distance (L). The magnetic permeability of the magnetic anomaly is displayed as multiples of magnetic permeability of vacuum (μ_0).

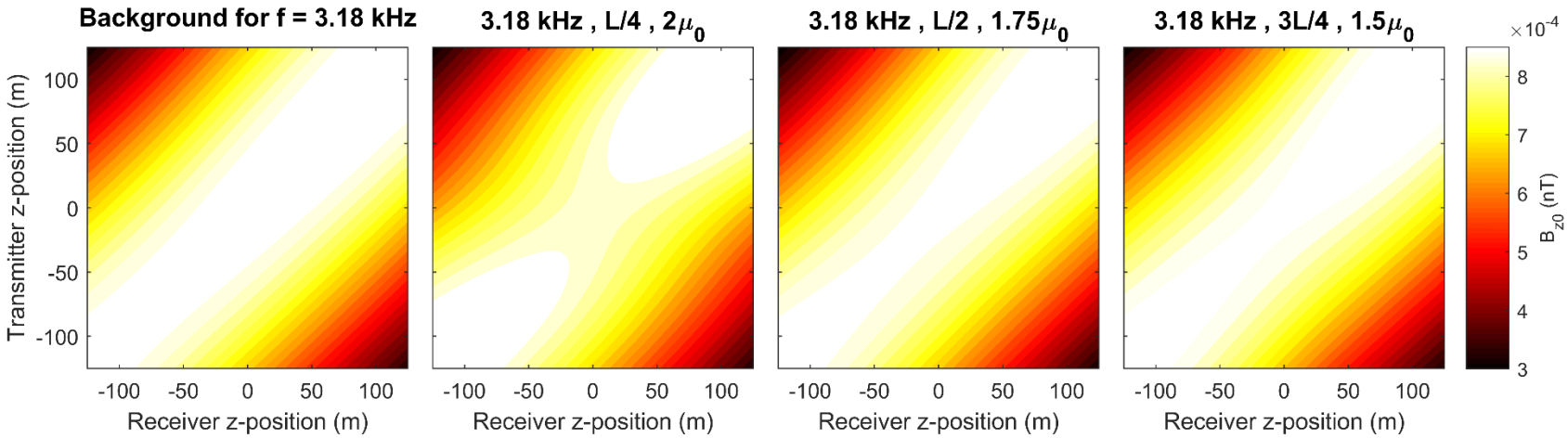

Figure 3.12 B_{z0} contour plots for the background without and with the magnetic slug at 3.18 kHz. The radial position of the magnetic anomaly is displayed in terms of the crosswell distance (L). The magnetic permeability of the magnetic anomaly is displayed as multiples of magnetic permeability of vacuum (μ_0). The blue and black squares depict the vertical boundaries of the conductive layer and magnetic anomaly, respectively.

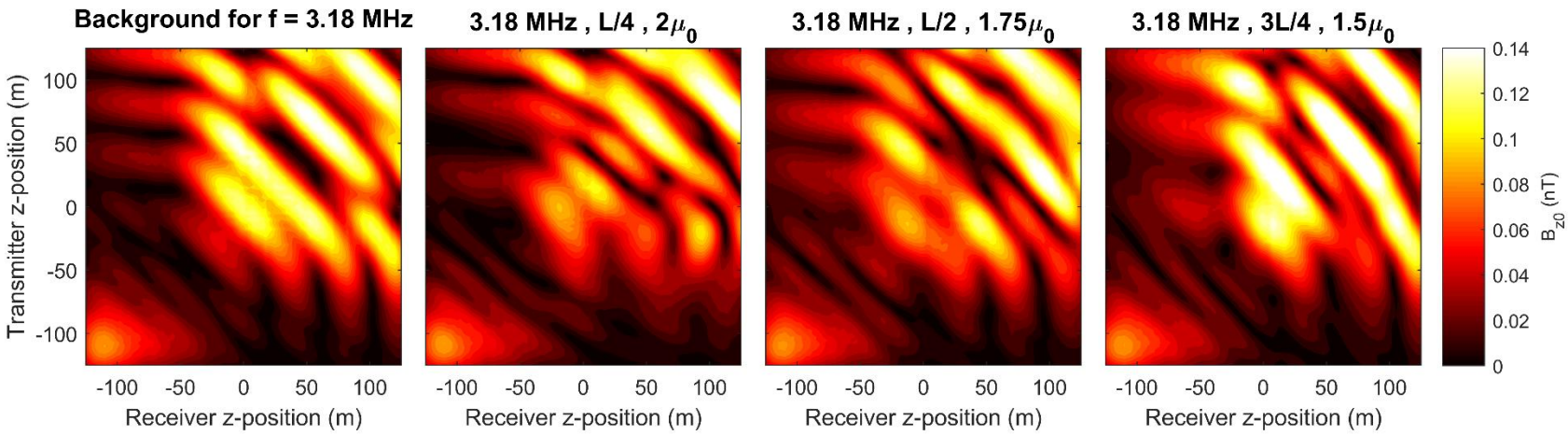

Figure 3.13 B_{z0} contour plots for the background without and with the magnetic slug at 3.18 MHz. The radial position of the magnetic anomaly is displayed in terms of the crosswell distance (L). The magnetic permeability of the magnetic anomaly is displayed as multiples of magnetic permeability of vacuum (μ_0).

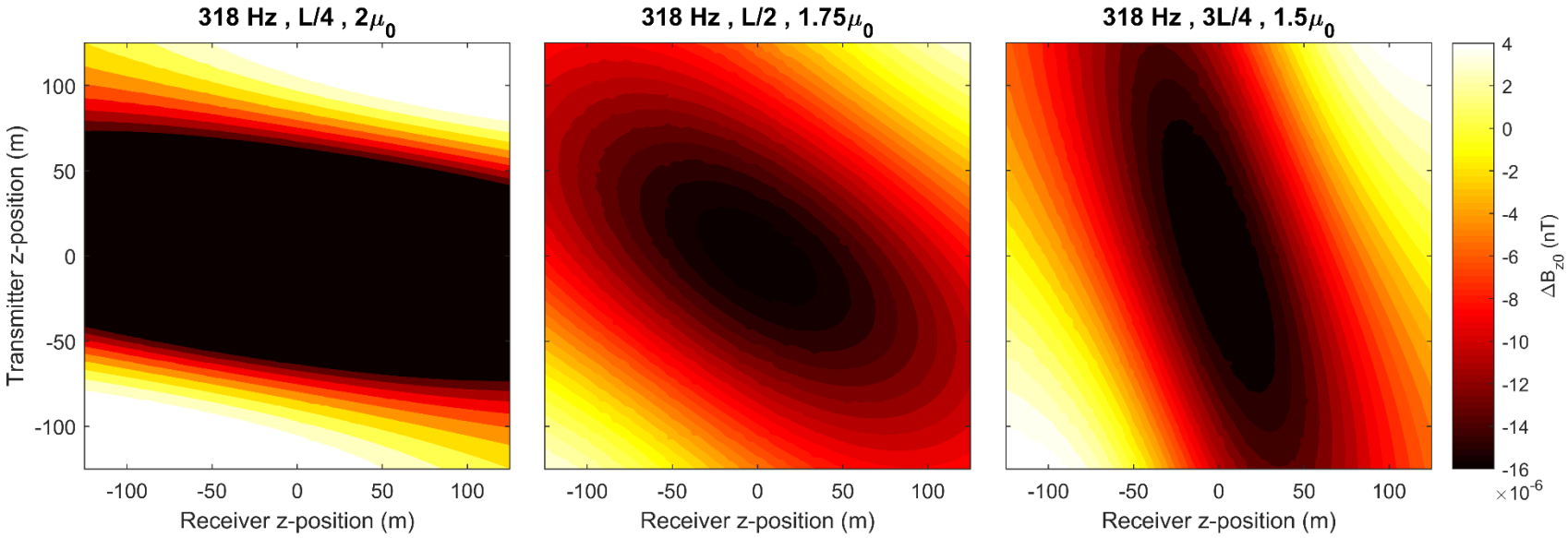

Figure 3.14 Differential contour plots of B_{z0} for the background with the magnetic slug at 318 Hz. The radial position of the magnetic anomaly is displayed in terms of the crosswell distance (L). The magnetic permeability of the magnetic anomaly is displayed as multiples of magnetic permeability of vacuum (μ_0).

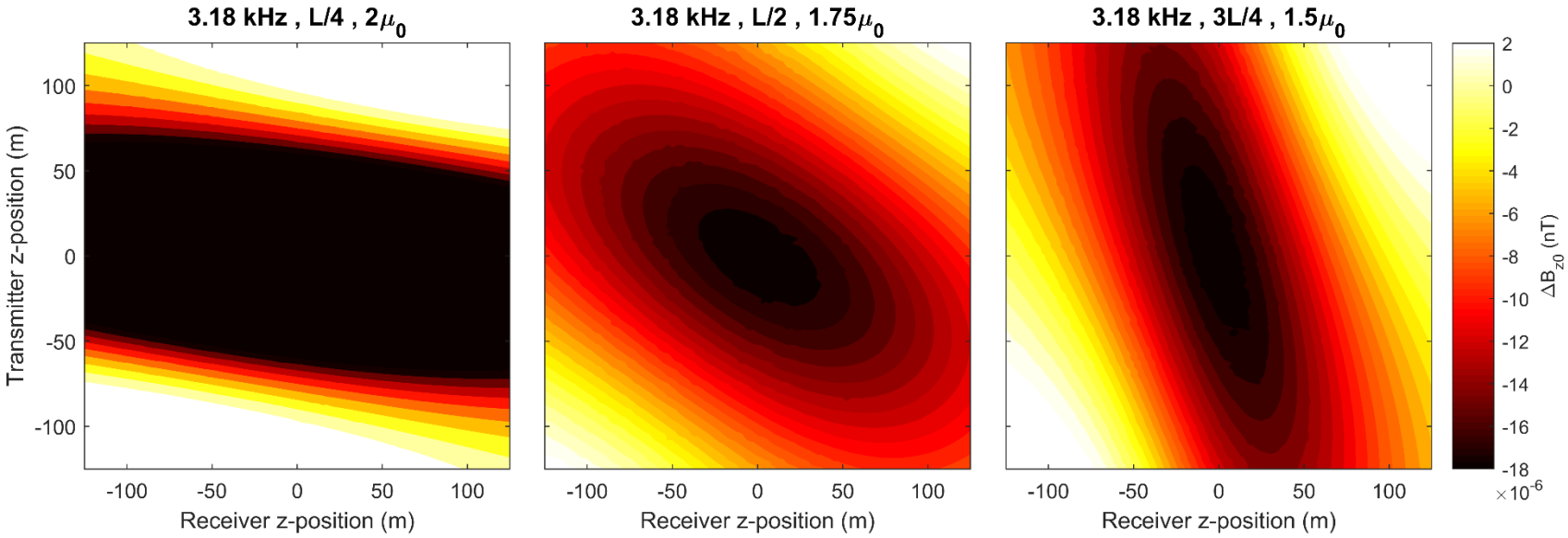

Figure 3.15 Differential contour plots of B_{z0} for the background with the magnetic slug at 3.18 kHz. The radial position of the magnetic anomaly is displayed in terms of the crosswell distance (L). The magnetic permeability of the magnetic anomaly is displayed as multiples of magnetic permeability of vacuum (μ_0).

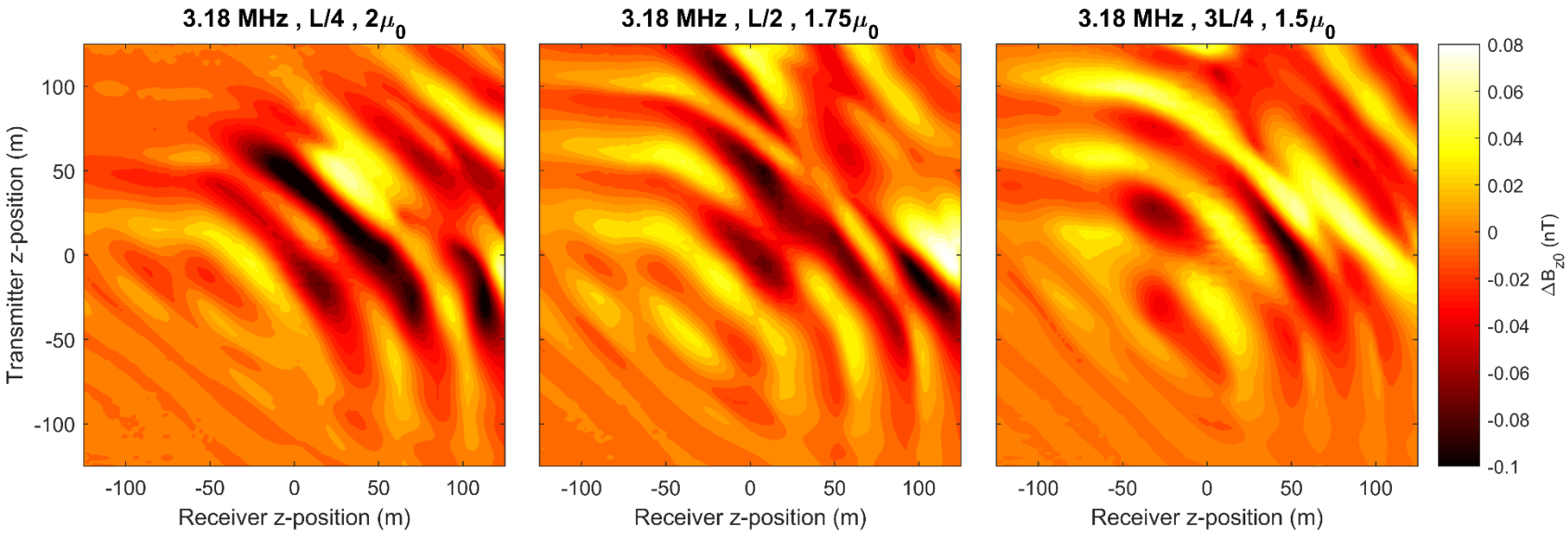

Figure 3.16 Differential contour plots of B_{z0} for the background with the magnetic slug at 3.18 kHz. The radial position of the magnetic anomaly is displayed in terms of the crosswell distance (L). The magnetic permeability of the magnetic anomaly is displayed as multiples of magnetic permeability of vacuum (μ_0).

3.4.3. Magnetic susceptibility of the slug

In order to calculate the minimum magnetic susceptibility of the ferrofluid required to generate the previous results, the *effective medium theory* was employed. This theory accounts for the contributions of the rock matrix, the ferrofluid, and the residual oil occupying the rock porosity [5]. Here, we will be applying the Bruggeman's model of the effective medium theory [25];

$$[1-(1-S_{or})\varphi_{rock}]\frac{\mu_{rock}-\mu_e}{\mu_{rock}+2\mu_e}+(1-S_{or})\varphi_{rock}\frac{\mu_{ferr}-\mu_e}{\mu_{ferr}+2\mu_e}=0 \qquad \text{(Equation 3.14)}$$

where S_{or} is the residual oil saturation within the rock, φ_{rock} is the rock porosity, μ_{rock} is the relative magnetic permeability of the rock matrix (assumed to be unity), μ_e is the effective relative magnetic permeability of the anomaly, and μ_{ferr} is the relative magnetic permeability of the injected ferrofluid. The magnetic susceptibility of the ferrofluid (χ) is ultimately calculated using the basic definition of relative magnetic permeability;

$$\mu_{ferr}=1+\chi \qquad \text{(Equation 3.15)}$$

As can be seen in Figure 3.17, the required magnetic susceptibility of the injected ferrofluid increases with the residual oil saturation, but decreases with rock porosity. In the first case, a higher residual oil saturation corresponds to a higher non-magnetic occupancy of the pore volume, and hence demanding a higher magnetization (i.e. magnetic moment per unit volume). In the second case, a higher porosity corresponds to a higher pore volume; therefore, requiring a lower magnetization.

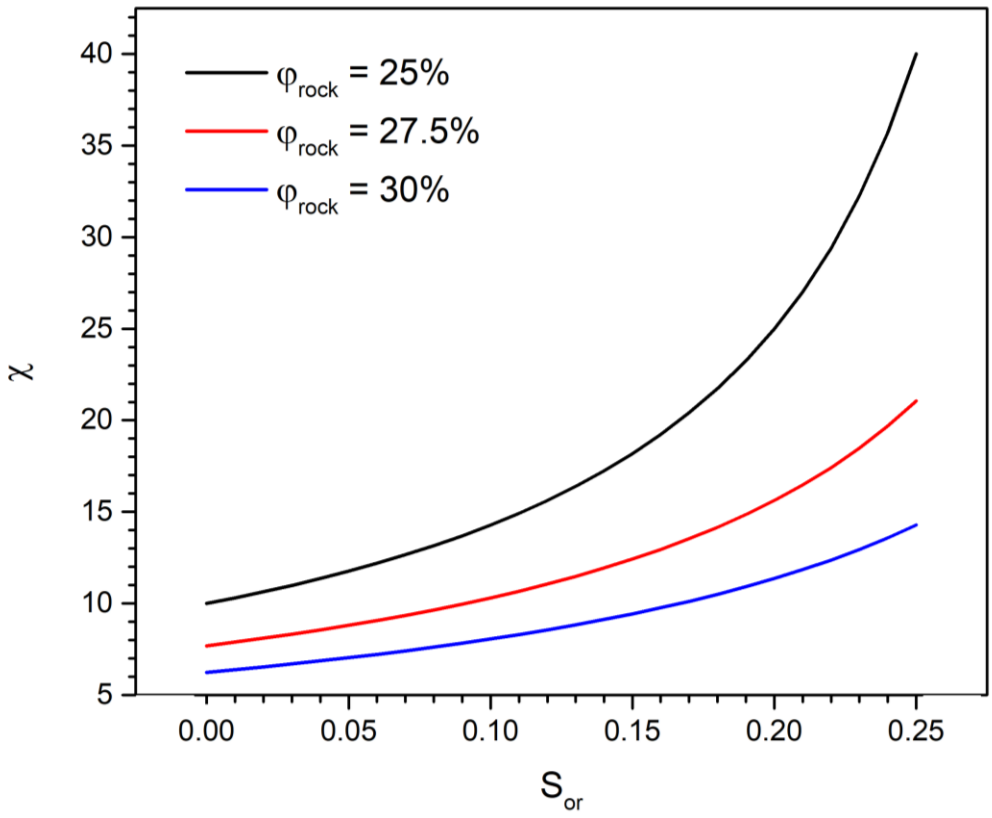

Figure 3.17 Required magnetic susceptibility of the injected magnetic slug as a function of residual oil saturation and rock porosity.

3.5. Pilot magnetic permeability-based EMT system

3.5.1. Experimental setup and methodology

A prototype laboratory-scale EMT system was constructed comprising two standalone units, namely the transmitter and receiver sections. Each section was equipped with a multi-turn coil antenna that is mounted on a vertical sliding frame as illustrated in Figure 3.18a. For the sake of convenience, we will be referring to the transmitting and receiving antennas as the transmitter and receiver, respectively. The transmitter was connected to a lock-in amplifier for the broadcasting of the time-harmonic primary magnetic field. The electromotive force (EMF) signal induced in the receiver due to the total field was measured using a lock-in amplifier and a digital voltmeter. Both antennas were equipped with motion control servomotors to allow the recording

of EMF signals for multiple combinations of their vertical positions (z-positions). These combinations are depicted as ray paths connecting the transmitting (i) and receiving (j) points as illustrated in Figure 3.18b.

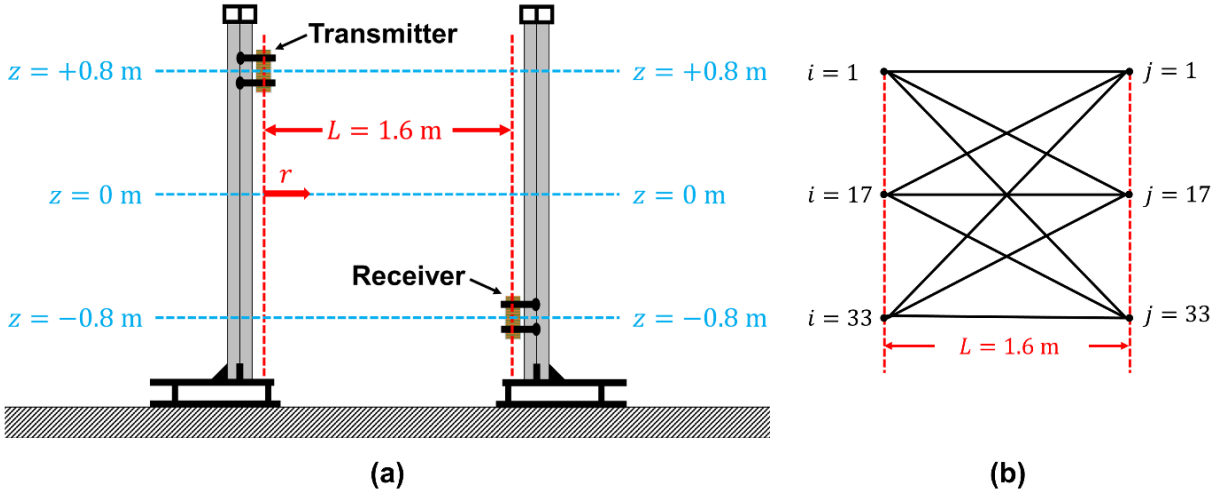

Figure 3.18 Design schematic of the developed pilot EMT system (a), and its corresponding ray path layout (b).

Implementations of the EMT system were conducted initially for an air background (i.e. without a magnetic anomaly) with a transmitter-to-receiver separation distance (L) of 1.6 m, and a vertical scanning distance of 1.6 m as shown in Figure 3.18a. Subsequently, a magnetic anomaly, consisting of a six-liter cubic plastic container filled with of a commercial ferrofluid (Ferrotec), was placed at different radial positions across the scanning plane, and vertically at the mid-position (z = 0). In both cases, the amplitude and frequency of the excitation current were set at 750 mA and 265 Hz, respectively. The acquired EMF survey arrays for the background; without and with the magnetic anomaly, were plotted in MATLAB yielding EMF contour plots. These plots were verified with the B_{z0} contour plots obtained from the COMSOL simulations of the EMT surveys. The differential contour plots were acquired upon background subtraction.

3.5.2. Experimental and simulation results

The low-frequency background EMT survey was conducted in the absence of the magnetic anomaly as depicted in Figure 3.19. As can be seen in Figure 3.19, both the EMF and B_{z0} contour plots of the background exhibit no anomalous response along the diagonal region. This is expected due the absence of an interfering secondary field arising from the magnetization of a magnetic anomaly by the primary field. In order to examine the influence of the spatial propagation of a magnetic anomaly, three different radial positions were considered: close to the transmitter ($r = L/4$), in the middle ($r = L/2$), and close to the receiver ($r = 3L/4$). As can be seen in Figure 3.20, the simulation results plausibly corroborate the experimental ones with an attenuation pattern similar to that observed in Figure 3.11. In this regard, the anomalous response is greatest when the anomaly is in close proximity to the transmitter and receiver, and smallest in the middle of the separation distance. Furthermore, the EMF and B_{z0} differential contour plots in Figure 3.21 are in agreement with each other as well as with Figures 3.14 and 3.15. These results ultimately confirm the applicability of magnetic permeability-based EMT systems for the tracking of propagating magnetic slugs in reservoirs.

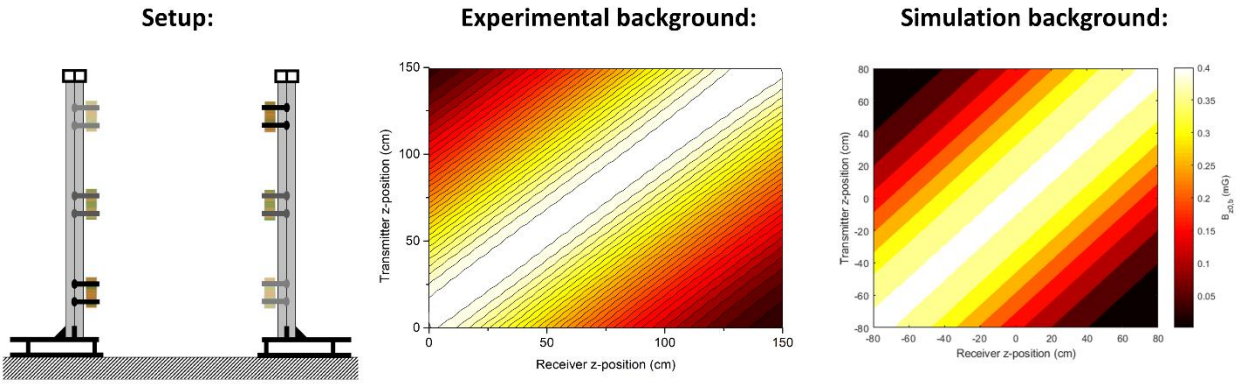

Figure 3.19 EMF and B_{z0} contour plots for the background.

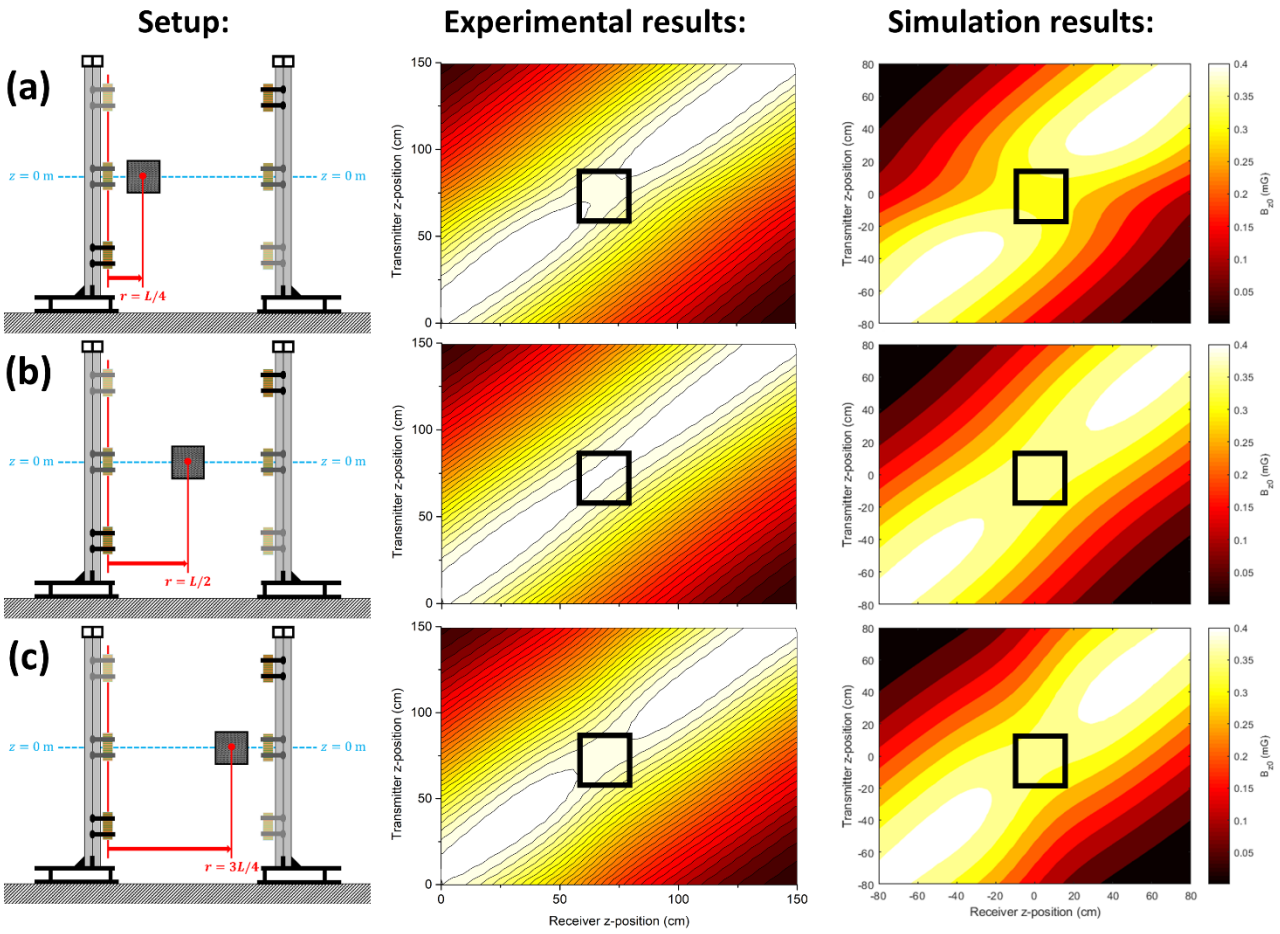

Figure 3.20 EMF and B_{z0} contour plots for different radial positions of the magnetic anomaly; $r = L/4$ (a), $r = L/2$ (b), and $r = 3L/4$ (c). The black square depicts the vertical boundaries of the magnetic anomaly.

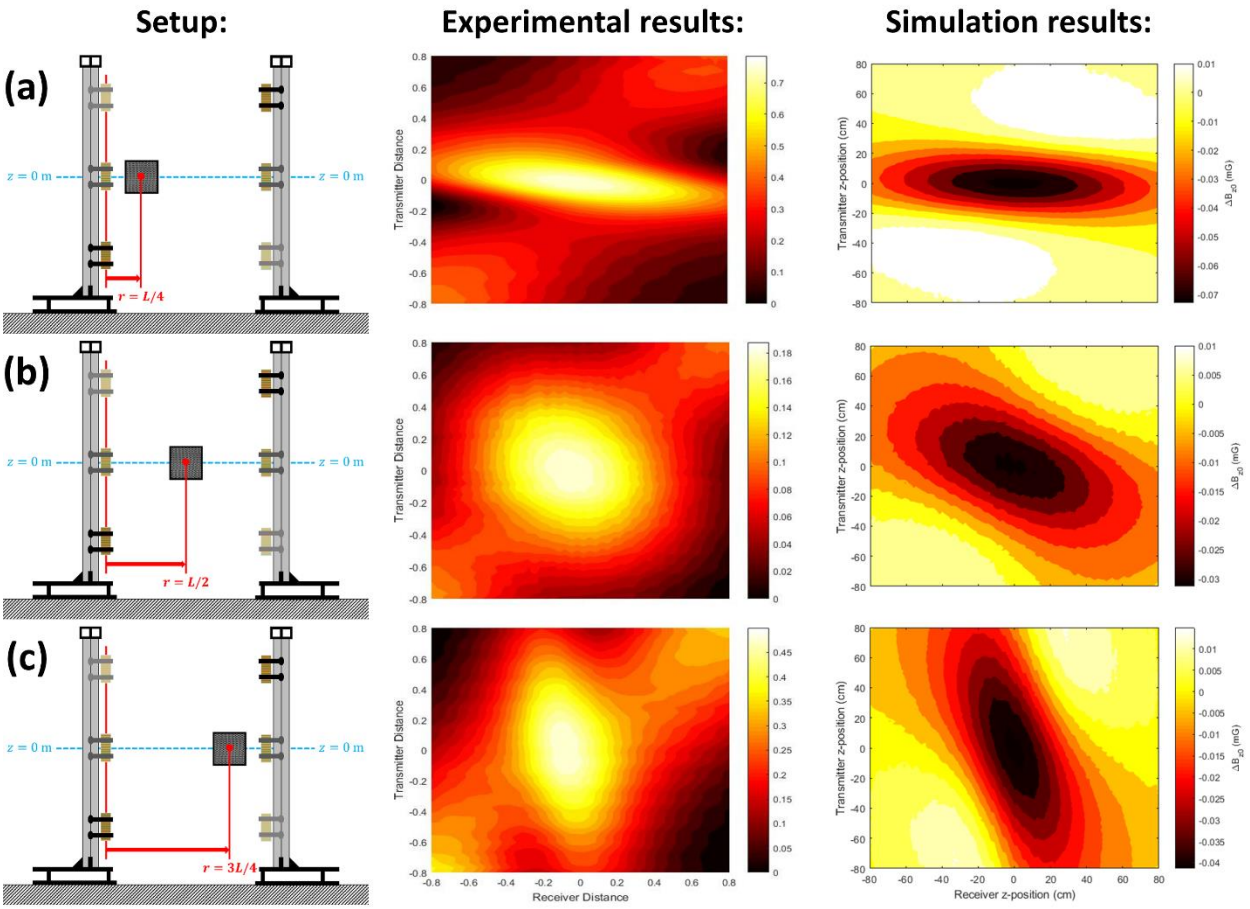

Figure 3.21 EMF and B_{z0} differential contour plots for different radial positions of the magnetic anomaly: $r = L/4$ (a), $r = L/2$ (b), and $r = 3L/4$ (c).

3.6. Conclusions

In this work, we have presented a detailed yet simple and practical methodology for the tracking of magnetic slugs propagating through geological formations. The most significant observation that is worth noting here is that the anomalous response of propagating magnetic slugs dominates that of conductive anomalies when the crosswell distance is one skin depth at least ($L \geq \delta$). Moreover, the required magnetic susceptibility of the injected ferrofluid is primarily judged by the rock porosity and the residual oil occupying it. The experimental and simulation results of the pilot EMT system were in agreement with those of the simulated large-scale system, and confirmed the applicability of magnetic permeability-based EMT for the tracking of propagating magnetic slugs in reservoirs.

Chapter 4

Synthesis and Characterization of Citric Acid-functionalized Iron Oxide Nanoparticles

4.1. Introduction

In addition to the aforementioned criteria for ideal tracers, the production of MNPs must be inexpensive and facile in order to be utilized in subsurface applications [26]. In this regard, iron oxide nanoparticles (IONPs) were found the most preeminent candidate material as they have been the most widely researched MNPs owing to their low-cost, ease of synthesis, and high magnetic susceptibility [27, 28]. The most ubiquitous method used to date for the synthesis of IONPs is the co-precipitation method, which involves the co-precipitation of ferrous (Fe^{2+}) and ferric (Fe^{3+}) ions from their acidic aqueous precursor solution by the addition of a base to at moderate temperatures (typically below 100 °C) [29]. Citric acid was chosen as a hydrophilic ligand for the surface functionalization of the IONPs in order to enhance their dispersibility and colloidal stability in the aqueous carrier fluid.

4.2. Experimental section

4.2.1. Chemicals

Iron(III) chloride ($FeCl_3$, anhydrous) was obtained from Riedel-de Haën®, ammonia (25 wt%, aqueous solution) was obtained from Chem-lab, and iron(II) chloride tetrahydrate ($FeCl_2 \cdot 4H_2O$, 98%) and citric acid (CA, 99%) were obtained from Alfa Aesar.

4.2.2. Synthesis of bare and citric acid-functionalized IONPs

In a typical synthesis, 14.6 g $FeCl_3$ (90 mmol Fe^{3+}) and 11.9 g $FeCl_2 \cdot 4H_2O$ (60 mmol Fe^{2+}) were dissolved in 200 mL deionized water and heated to 90 °C. Then, 60 mL of ammonia solution and 6.5 g of CA were sequentially added under vigorous mechanical stirring. The reaction mixture was continued to be stirred at 90 °C for 1 hr. After cooling, 150 mL acetone was added to force the precipitation of the nanoparticles. The precipitate was washed several times with water and excess acetone, and dried overnight at room temperature. Figure 4.1 shows the magnetic response of aqueous ferrofluids of CA-IONPs at two particle concentrations. Note that the Rosensweig peak density is proportional to the particle concentration. Bare IONPs were synthesized as a reference sample for the crystallographic, chemical, and thermal analyses following the same procedure, but without the addition of CA.

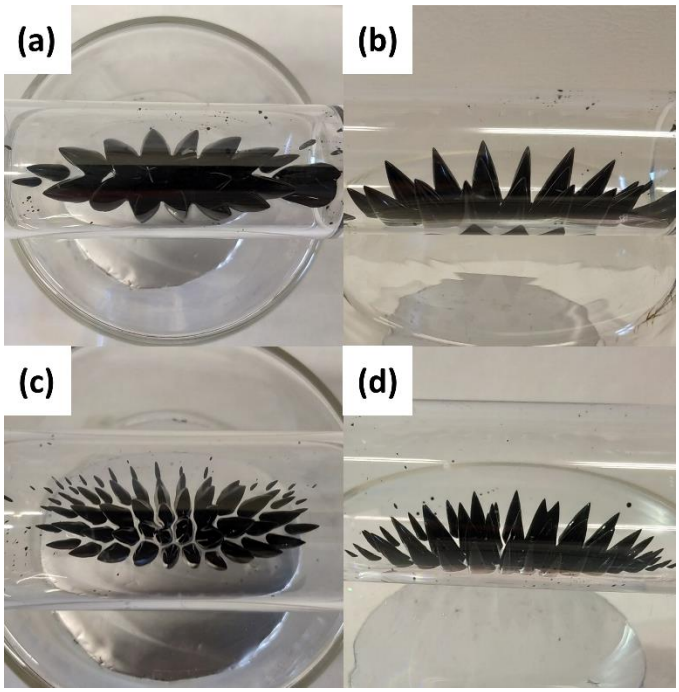

Figure 4.1 Normal-field (Rosensweig) instability of dense aqueous ferrofluids of CA-IONPs at two particle concentrations. Top-views (a,c) and side-views (b,d) of the 1 kg/L (50 wt%) and 2 kg/L (67 wt%) ferrofluid samples, respectively.

4.2.3. Characterization

The chemical composition of the samples was characterized using the PerkinElmer® Spectrum 100 Fourier transform infrared (FTIR) spectrometer and the attenuated total reflection (ATR) method. The transmittance measurements were recorded over the wavenumber range of 400-4000 cm^{-1}. Thermal analysis was performed using the PerkinElmer® Pyris 7 thermogravimetric analyser. The temperature was initially maintained at 100 °C for 10 min to allow the samples to dry out. The measurements were then recorded over the temperature range of 100-800 °C with a heating rate of 10 °C/min. The samples were continuously purged with nitrogen during the course of the measurements. Crystallographic analysis was performed using the Siemens D500 X-ray diffractometer with a Cu-Kα radiation source, wavelength of 1.5418 Å, and scan rate of 2.0000 deg/min. The structural properties were examined using the FEI-Philips CM20 microscope operating at 200 kV accelerating voltage, and the size distribution was obtained using the ImageJ software [30]. The DC magnetization measurements were performed using the Quantum Design MPMS® 5.5 T superconducting quantum interference device (SQUID) magnetometer. To obtain the hysteresis loop, the magnetization measurements were recorded in a magnetic field range of ±50 kOe. For the zero-field cooling (ZFC) and field-cooling (FC) magnetization measurements, all samples were cooled to 20 K without any applied field before heating to 300 K, followed by subsequent cooling to 10 K under a DC field of 100 Oe. The Mössbauer spectrum was obtained using a conventional transmission spectrometer equipped with a ^{57}Co(Rh) source moving with constant acceleration. A Janis cryostat was utilized to obtain the low-temperature spectrum at 4.2 K. Isomer shifts are given with respect to metallic iron at 4.2 K. The spectrum was least-squares fitted using the IMSG program [31].

4.3. Results and discussion

4.3.1. Reaction mechanism

Citric acid-functionalized IONPs (CA-IONPs) were synthesized via the co-precipitation of Fe^{2+} and Fe^{3+} ions in the presence of CA. The nucleation and growth mechanisms of IONPs can be described are within the framework of classical nucleation theory as illustrated in Figure 4.2 [32]. The reaction is initiated by the addition of ammonium hydroxide (base) to the acidic aqueous solution of the iron precursors, which triggers the formation of primary particles. The accretion of these particles results in the formation of the iron oxide nuclei (i.e. nucleation of iron oxide nanocrystals), which grow into larger crystalline nanoparticles by the attachment of excess primary particles. The growth of nanoparticles is ultimately terminated by the formation of the CA shells, which inhibit the further attachment of excess primary particles.

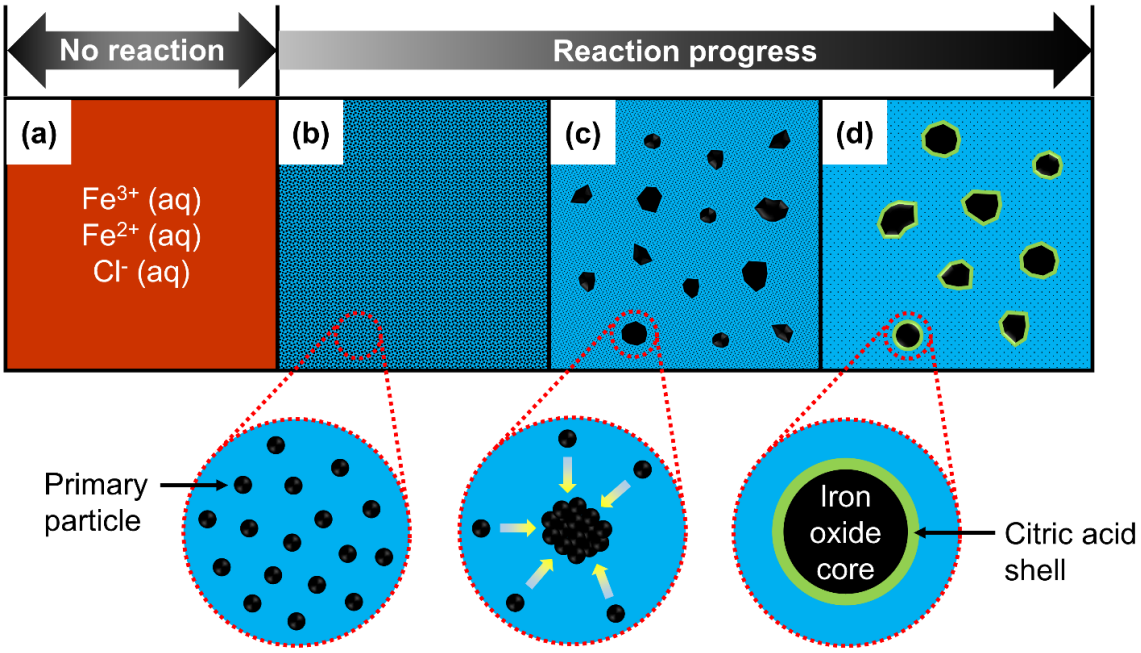

Figure 4.2 Synthesis of CA-IONPs: (a) Starting aqueous solution of the iron precursors. (b) Formation of primary particles. (c) Nucleation and growth of iron oxide nanocrystals. (d) Growth termination due to the formation of CA shells.

4.3.2. Structural and crystallographic analyses

The size and shape of CA-IONPs were investigated using transmission electron microscopy (TEM). Figure 4.3a shows polydisperse nanoparticles in the range of 3–10 nm; as per the corresponding size distribution in Figure 4.3b, and most of them exhibit a spheroidal shape. X-ray diffraction (XRD) was implemented to examine the crystal structures of the bare and CA-functionalized IONPs. All the characteristic peaks in Figure 4.3c match those of magnetite (JCPDS card No 65-3107) as well as maghemite (JCPDS card No 39-1364).

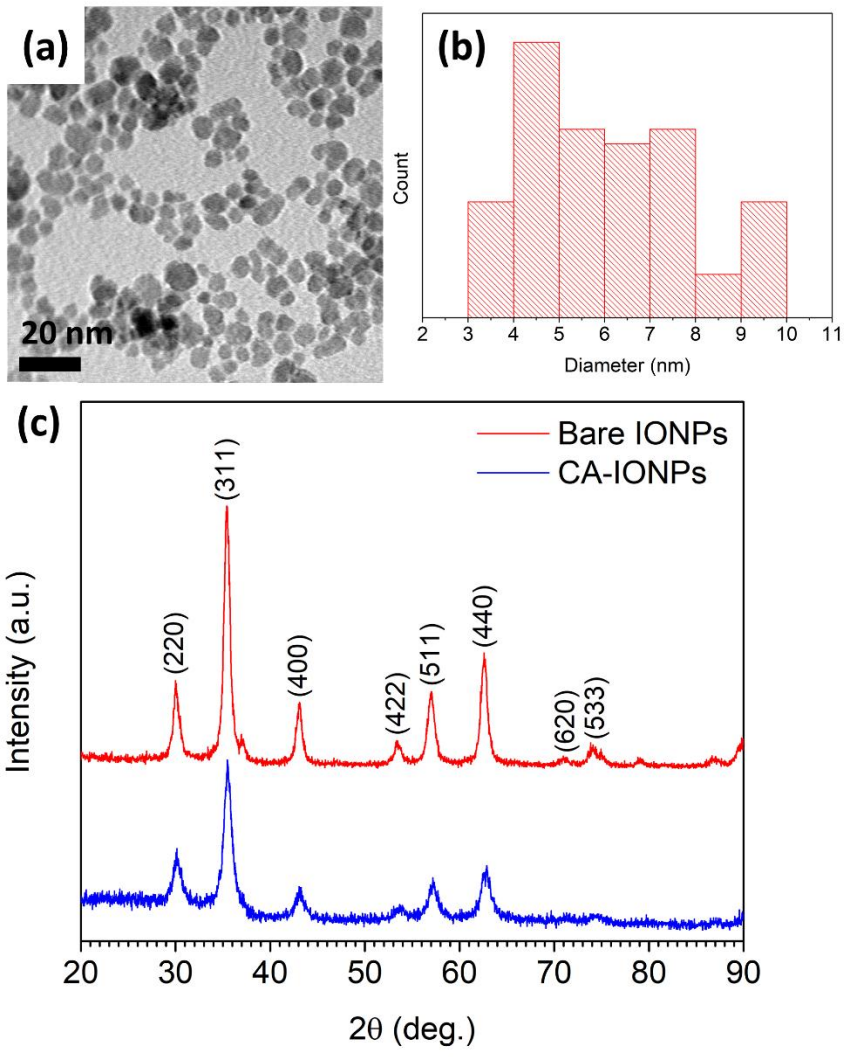

Figure 4.3 TEM analysis of CA-IONPs (a), and the corresponding size distribution (b). XRD patterns of bare and CA-functionalized IONPs (c).

4.3.3. Chemical and thermal analyses

The binding characteristics of CA to the surface of IONPs were examined by ATR-FTIR spectroscopy. As can be seen in Figure 4.4, the strong absorption band at 554 cm^{-1} is attributed to the Fe-O vibrations in the lattice structures of the bare and CA-functionalized IONPs [33]. The bands at 1416 and 1619 cm^{-1} in the spectrum of the bare IONPs can be ascribed to the bicarbonate C-O stretching vibrations due to adsorbed atmospheric CO_2 [34]. The bands at 1695 and 1743 cm^{-1} in the spectrum of neat CA can be assigned to the C=O stretching vibrations in the carboxylic functional groups of CA [35]. The bands at 1394 and 1604 cm^{-1} in the spectrum of CA-IONPs are characteristic of carboxylate symmetric and asymmetric vibrations, respectively, and hence indicating the formation of Fe-carboxylate bidentate coordination bonds at the surface of the IONPs [35]. This is particularly due to the fact that the carboxyl groups of CA were fully deprotonated in the basic reaction mixture.

The chemisorption of CA on the surface of CA-IONPs was further examined by thermogravimetric analysis (TGA). As can be seen in Figure 4.5a, the thermogram of bare IONPs exhibits a mass loss of approximately 8%, which is probably attributed to the adsorbed water [36, 37]. The thermograms of neat CA and CA-IONPs exhibit a single-step mass loss at onset temperatures of 172 and 181 °C, respectively (Figure 4.5b). This loss is associated with the decomposition of CA due to decarboxylation [38]. The increase in the onset decomposition temperature in the CA-IONPs thermogram confirms the chemisorption of CA molecules on the iron oxide surface, which is in agreement with the FTIR results. Figure 4.6 shows the possible configurations in which CA could bind to the surface of IONPs.

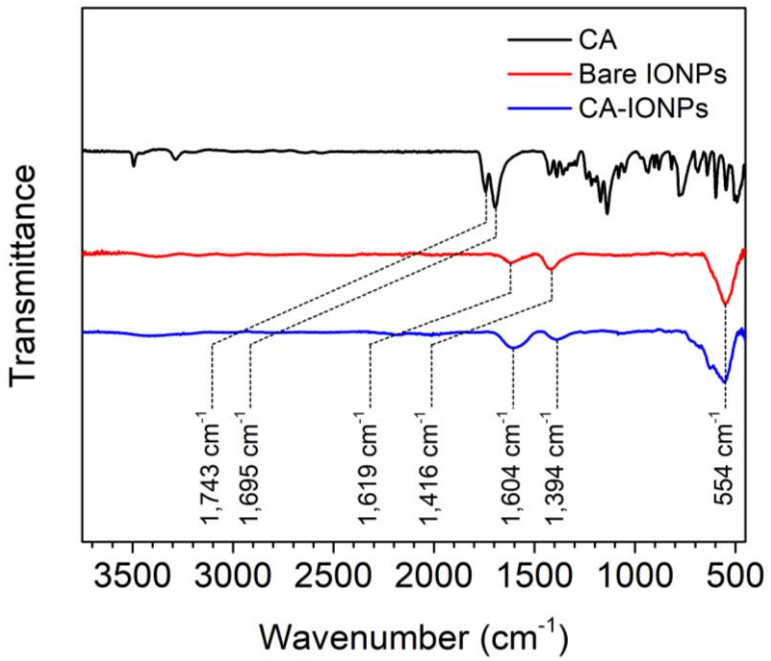

Figure 4.4 FTIR spectra of neat CA, bare IONPs, and CA-IONPs.

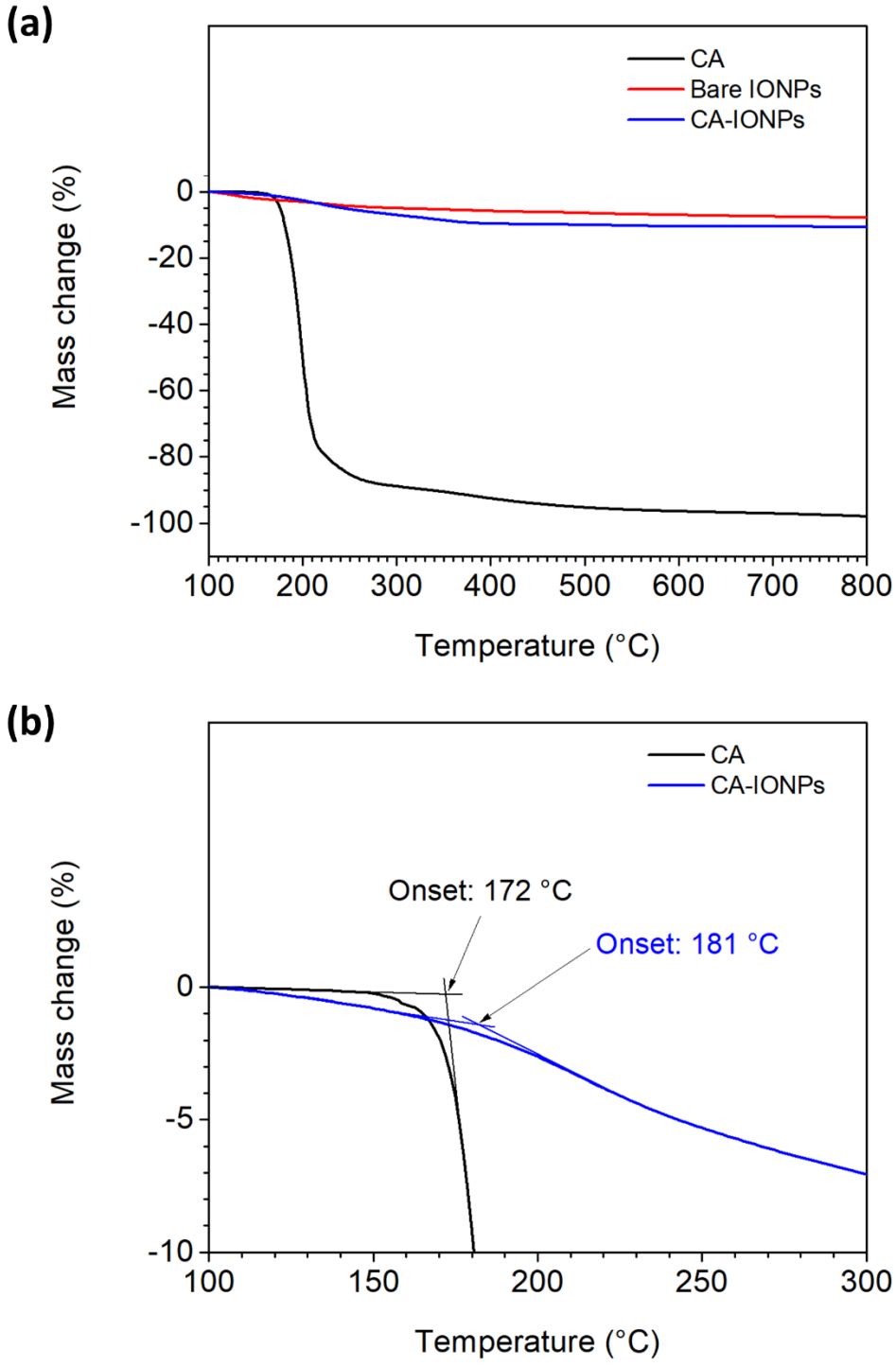

Figure 4.5 (a) TGA thermograms of neat CA, bare IONPs, and CA-IONPs. (b) Onset decomposition temperature analysis for neat CA and CA-IONPs.

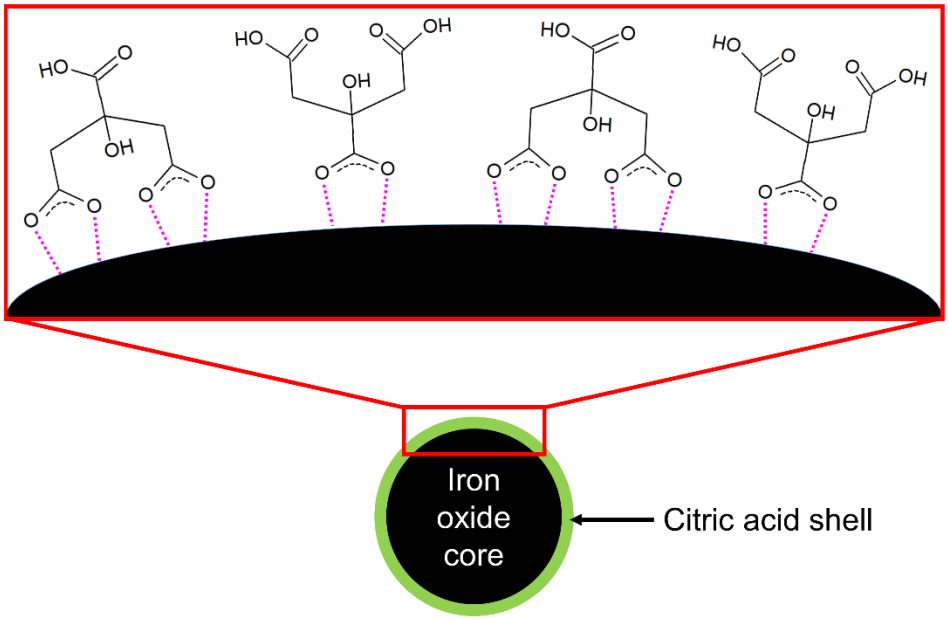

Figure 4.6 Binding of CA to the surface of an IONP via bidentate Fe-carboxylate coordination bonds. The exposed (non-coordinating) carboxylic functional groups were probably reprotonated during the course of washing.

4.3.4. Magnetic phase composition

Magnetite and maghemite, the two possible phases identified in the XRD analysis of CA-IONPs, are iron oxide phases of similar cubic spinel structure, but different electric and magnetic properties. This is due to the difference in the Fe^{2+} and Fe^{3+} occupancy in their spinel lattice structures. The empirical formula of magnetite is given as $\left(Fe^{3+}\right)_A\left[Fe^{3+}\,Fe^{2+}\right]_B O_4$ where the subscripts *A* and *B* refer to the tetrahedral and octahedral sites, respectively. Maghemite; however, is known to be a ferrous-deficient magnetite, and hence its empirical formula is often expressed as a nonstoichiometric magnetite containing vacancies (represented by a blank square) in the B-sites, that is $\left(Fe^{3+}\right)_A\left[Fe^{3+}{}_{0.6625}\,\square_{0.3375}\,Fe^{3+}\right]_B O_4$. Therefore, Mössbauer spectroscopy was employed for the identification of magnetic phases present in CA-IONPs.

The sextet hyperfine splitting observed in the ^{57}Fe Mössbauer spectrum of the CA-IONPs at 4.2 K (Figure 4.7) indicates that all Fe ions are in a magnetically ordered state. The spectrum was fit to two magnetic components, whose hyperfine parameters are listed in Table 4.1. The values of isomer shifts (δ) and quadrupole splitting (Δ) are typical of Fe^{3+} ions [39, 40]. The lower hyperfine magnetic field (H_{hf}) values correspond to the A-site Fe^{3+} ions, whereas the higher ones correspond to the B-site Fe^{3+} ions [40]. The absence of Fe^{2+} ions clearly indicates that the magnetite phase is not present. Therefore, it can be deduced that the iron oxide phase of CA-IONPs is solely made up of maghemite.

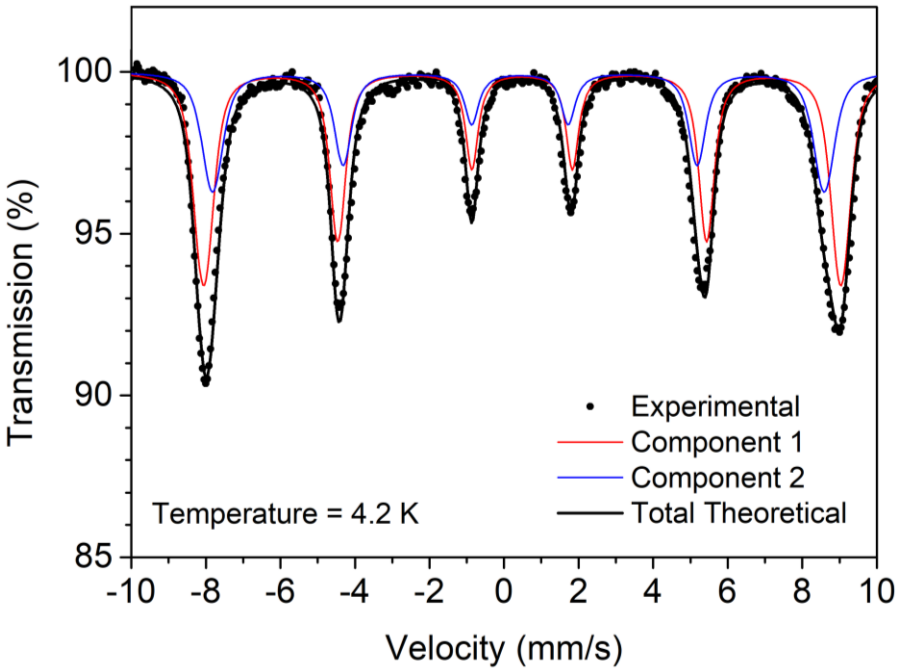

Figure 4.7 ^{57}Fe Mössbauer spectrum of CA-IONPs.

Table 4.1 Hyperfine parameters for CA-IONPs as per the best fits.

Magnetic component	δ **(mm/s)**	Δ **(mm/s)**	H_{hf} **(kOe)**	**Designation**
Component 1	0.487	0	531	B-site Fe^{3+}
Component 2	0.406	-0.047	510	A-site Fe^{3+}

4.3.5. Magnetic measurements

The magnetic properties of CA-IONPs were investigated by means of standard SQUID measurements. Figure 4.8a shows the hysteresis loop for CA-IONPs obtained at 300 K for a magnetic field range of ±50 kOe. The observed saturation magnetization (M_s) was found to be 66 emu/g. A zoomed view of the hysteresis loop in the low-field region (±4 kOe) is presented in Figure 4.8b. The absence of an observable hysteresis in the low-field region signifies the superparamagnetic nature of CA-IONPs at 300 K (i.e. zero-coercivity).

Figure 4.9a shows the ZFC and FC magnetizations (M_{ZFC} and M_{FC}, respectively) versus temperature (T) for CA-IONPs. As can be seen in Figure 4.9a, the M_{ZFC} curve exhibits a typical blocking process of an assembly of superparamagnetic nanoparticles with a distribution of blocking temperatures, which in fact confirms the polydisperse nature of the particles. Blocking temperature (T_B) is the temperature at which the transition between the "blocked state" and "superparamagnetic" regimes instantaneously occurs. The experimental T_B distribution was obtained from the normalized first derivative plot of the differential magnetization ($\Delta M = M_{FC} - M_{ZFC}$) divided by T as shown in Figure 4.9b [41]. The plot was fit with a Gaussian distribution (T_B);

$$f(T_B) = \frac{1}{\sigma\sqrt{2\pi}} \exp\left[-\frac{1}{2}\left(\frac{T_B - \langle T_B \rangle}{\sigma}\right)^2\right] \quad \text{(Equation 4.1)}$$

with a mean blocking temperature ($\langle T_B \rangle$) of 256 K, and a standard deviation (σ) of 27 K.

It can be clearly observed in Figure 4.9a that the M_{FC} curve exhibits a plateau (i.e. temperature-independent magnetization) below $\langle T_B \rangle$. This characteristic phenomenon is associated with high concentrations of interacting magnetic dipoles, which are often called *super-spin glasses* [42-44]. However, it is difficult to obtain quantitative information on the influence of magnetic dipolar interactions from DC magnetization measurements [42].

AC magnetization measurements, which are used to obtain quantitative information on the relaxation time (τ), have shown that τ diverges in the same manner as in a spin glass system when the sample is cooled towards the phase transition temperature (T_g) [45]. For $T > T_g$, τ is expected to obey the temperature dependence, which is expressed as follows

$$\tau(T) = \tau^* \left(\frac{T}{T_g} - 1\right)^{-zv} \quad \text{(Equation 4.2)}$$

where τ^* is the relaxation time of non-interacting particles, and zv is a critical exponent on the order of 10 [42, 45]. Finally, it should be realized that the investigation of the influence of the magnetic dipolar interactions on the magnetic properties of CA-IONPs is beyond the scope of this work, but it will be explored in the near future.

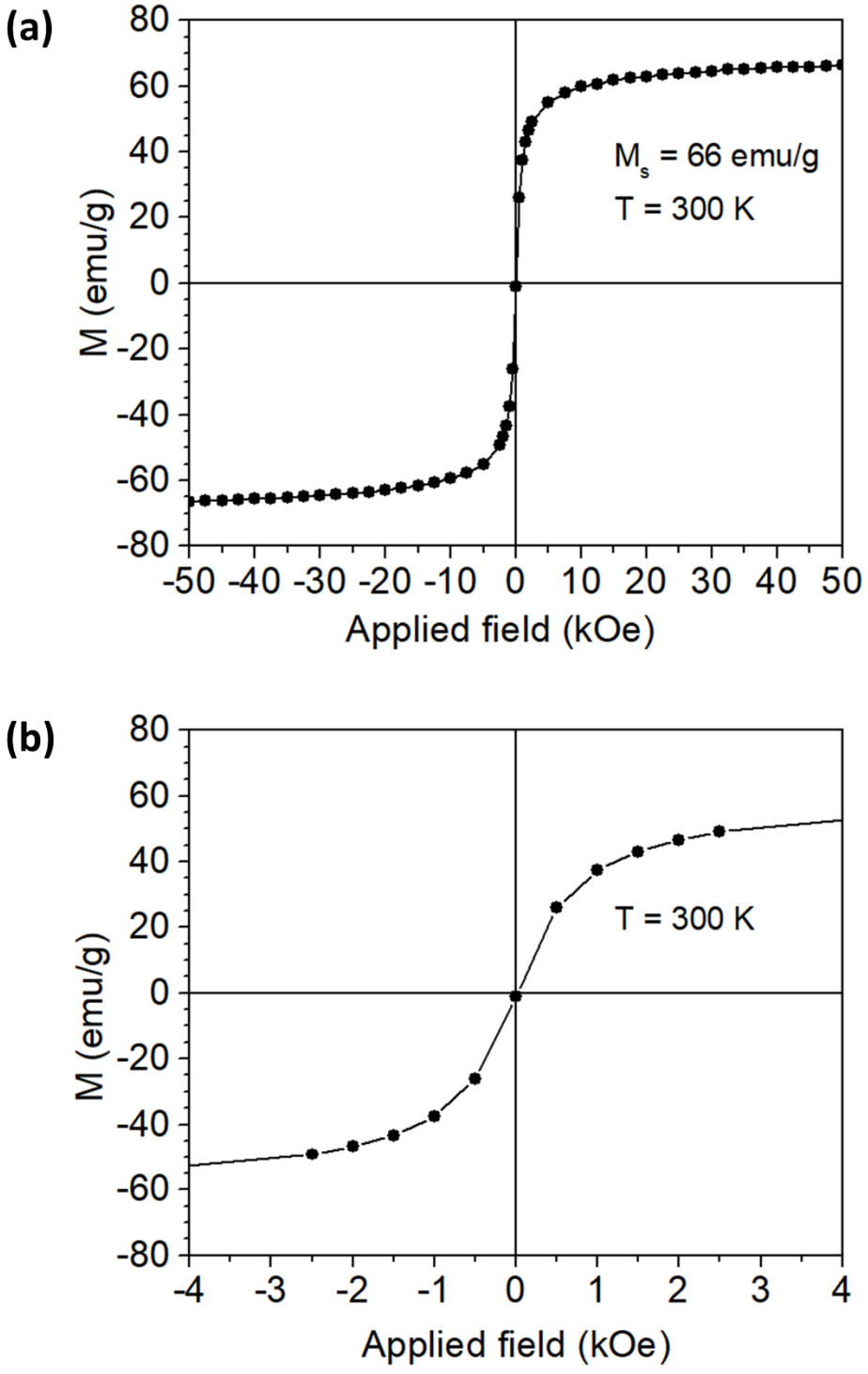

Figure 4.8 Hysteresis loop of CA-IONPs: Full loop (a) and zoomed view (b).

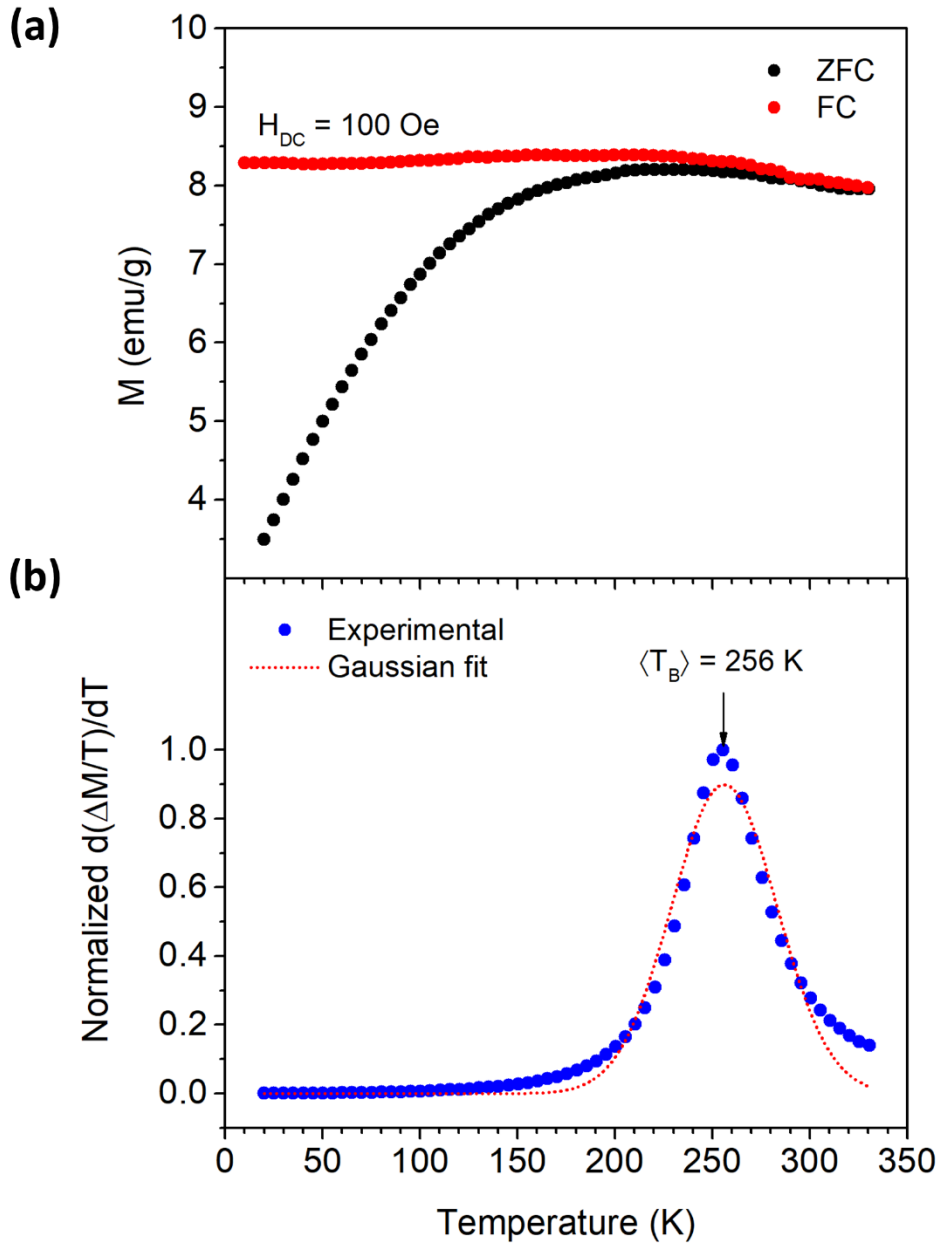

Figure 4.9 (a) M_{ZFC} and M_{FC} curves for CA-IONPs. (b) Experimental T_B distribution and its Gaussian fit.

4.4. Conclusions

A facile large-scale synthesis of hydrophilic MNPs (CA-IONPs) exhibiting high dispersibility at high-particle concentrations was achieved. The particles exhibit a high thermal stability, which is critical to endure the high-temperatures in the reservoirs. Moreover, the particles exhibit superparamagnetism at temperatures above 256 K with considerable magnetic dipolar interactions at high particle concentrations. It will be very interesting to explore the role of magnetic dipolar interactions on the colloidal stability of CA-IONPs at high-particle concentrations as we will see later in Chapter 6.

Chapter 5

Overview of Colloidal Phenomena: Electrostatics, Electrokinetics, and Colloidal Stability

5.1. Introduction

In a dispersion of colloidal particles (i.e. particles of submicron size), particles tend to approach each other with virtue of Brownian motion, and thus their stability is determined by the nature of interactions between them. Generally, there are two types of interparticle interactions: attractive (e.g. van der Waals) and repulsive (e.g. electrostatic) forces. When attractive forces dominate, colloidal particles associate with each other, whereas when repulsive forces are dominant, colloidal particles remain dispersed throughout the dispersion medium resulting in a stable colloid. In this chapter, a thorough overview of the colloidal phenomena associated with colloidal stability will be presented. This will be followed by a brief discussion on the thermodynamic and kinetic considerations of colloidal stability.

5.2. Surface-charging mechanisms

Most colloidal particles acquire a surface electric charge as soon as they are brought into contact with a polar dispersion medium (e.g. aqueous) via either of the following charging mechanisms: ionization, ion adsorption, or ion dissolution. This surface charge, as we will see later, leads to the formation of the *electric double layer*, which plays a major role in the stability of colloidal systems.

5.2.1. Ionization

The ionization process involves proton transfer reactions taking place between the colloidal particle and the surrounding aqueous medium. These reactions are strongly influenced by the pH of the aqueous medium. For example, proteins contain carboxyl (acidic) and primary amino (basic) functionalities; at low pH (i.e. acidic medium), the net molecular charge of a protein will be positive as the amino functionalities will be protonated to give $-NH_3^+$; however, at high pH (i.e. basic medium), the net molecular charge of a protein will be negative as the carboxyl functionalities will be deprotonated to give $-COO^-$ [46].

5.2.2. Ion adsorption

A surface of a colloidal particle can have a net surface charge due to unequal adsorption of oppositely charged ions. Surfaces in contact with aqueous media are more often negatively charged than positively charged. This is due to the fact that cations are usually more hydrated than anions, which implies that cations have a greater tendency to reside in the bulk aqueous medium while anions tend to be specifically adsorbed on the surface [46].

Surfaces that are already charged (e.g. by ionization) usually show a preferential tendency to adsorb ions of opposite charge (*counter ions*), especially highly charged ones. It is possible for counter ion adsorption to cause reversal of surface charge [46].

5.2.3. Ion dissolution

Ionic substances can acquire a surface charge by virtue of unequal dissolution of the oppositely charged ions of which they are composed. Let us consider the example of silver iodide (AgI) dissolution in an aqueous medium, which can be described in the following reaction:

$$\mathrm{AgI}(s) \rightleftharpoons \mathrm{Ag^+}(aq) + \mathrm{I^-}(aq)$$

The solubility product K_{sp} of this reaction at 25 °C is estimated to be

$$K_{sp} \approx a(\mathrm{Ag^+})\, a(\mathrm{I^-}) \cong 10^{-16} \qquad \text{(Equation 5.1)}$$

where a(Ag^+) and a(I^-) are the activities of silver (Ag^+) and iodide ions (I^-), respectively. Therefore, theoretically it can be deduced from Equation 5.1 that

$$a(\mathrm{Ag^+}) = a(\mathrm{I^-}) = 10^{-8}$$

and accordingly,

$$p\mathrm{Ag} = -\log a(\mathrm{Ag^+}) = -\log 10^{-8} = 8$$

$$p\mathrm{I} = -\log a(\mathrm{I^-}) = -\log 10^{-8} = 8$$

However, this is not the case; the experimental results have shown that pAg = 5.3. This is because the smaller and more mobile Ag^+ ions are held less strongly than the I^- ions in the AgI crystal lattice. In this example, the Ag^+ and I^- ions are referred to as *potential-determining ions* because their concentrations determine the electric potential at the surface of the AgI crystal [46].

5.3. The electric double layer

The surface charge of a colloidal particle influences the distribution of nearby ions in a polar medium, where counter ions are attracted towards the surface of the colloidal particle while ions of like charge (*co-ions*) are repelled away from it. This, together with the mixing effects due to

Brownian motion, leads to the formation of an electric double layer made up of two phases: the charged surface of the colloidal particle and a neutralizing excess of counter ions over co-ions distributed in a diffuse manner in the polar medium [46].

5.3.1. Poisson's equation of electrostatics

The variation of electric potential with distance from a charged surface of arbitrary shape is a classical problem in electrostatics. The general problem is described by *Poisson's equation of electrostatics*, which can be derived from Gauss's law and Gauss's divergence theorem.

Starting with Gauss's law, the net electric flux Φ of an electric field $\mathbf{E}$ permeating a closed Gaussian surface element dS is defined as follows

$$\Phi = \iint_S (\mathbf{E} \cdot \hat{\mathbf{n}})\, dS = \frac{q_{enc}}{\varepsilon_0 \varepsilon_r} \qquad \text{(Equation 5.2)}$$

where $\hat{\mathbf{n}}$, q_{enc}, ε_0, and ε_r are the outward pointing surface normal, charge enclosed by dS, vacuum permittivity, and relative permittivity of the medium enclosed by dS, respectively.

Let ρ^* be the *volume charge density* of the volume element dV enclosed by dS;

$$\rho^* = \frac{dq_{enc}}{dV} \qquad \text{(Equation 5.3)}$$

From Equation 5.3, it can be deduced that

$$q_{enc} = \iiint_V \rho^*\, dV \qquad \text{(Equation 5.4)}$$

Substituting Equation 5.4 into Equation 5.2 yields

$$\iint_S (\mathbf{E} \cdot \hat{\mathbf{n}})\, dS = \iiint_V \frac{\rho^*}{\varepsilon_0 \varepsilon_r} dV \qquad \text{(Equation 5.5)}$$

From Gauss's divergence theorem, we know that

$$\iint_S (\mathbf{E} \cdot \hat{\mathbf{n}})\, dS = \iiint_V (\text{div}\, \mathbf{E})\, dV \qquad \text{(Equation 5.6)}$$

where div $\mathbf{E}$ is the divergence of $\mathbf{E}$, which is defined as follows

$$\text{div}\, \mathbf{E} = \nabla \cdot \mathbf{E} \qquad \text{(Equation 5.7)}$$

By observing Equations 5.5-5.7, it can be deduced that

$$\iiint_V (\nabla \cdot \mathbf{E})\, dV = \iiint_V \frac{\rho^*}{\varepsilon_0 \varepsilon_r} dV \qquad \text{(Equation 5.8)}$$

Moving the right-hand side of Equation 5.8 to the left-hand side yields

$$\iiint_V \left(\nabla \cdot \mathbf{E} - \frac{\rho^*}{\varepsilon_0 \varepsilon_r}\right) dV = 0 \qquad \text{(Equation 5.9)}$$

Therefore, from Equation 5.9 we have

$$\nabla \cdot \mathbf{E} = \frac{\rho^*}{\varepsilon_0 \varepsilon_r} \qquad \text{(Equation 5.10)}$$

Note that substitution of Equation 2.5 into Equation 5.10 yields Maxwell's first equation (Equation 2.1); the generalized differential form of Gauss's law.

The electric field is defined as the negative gradient of electric potential ψ; therefore,

$$\mathbf{E} = -\nabla\psi \qquad \text{(Equation 5.11)}$$

Finally, substituting Equation 5.11 into Equation 5.10 yields the Laplacian of ψ;

$$\nabla^2\psi = \frac{-\rho^*}{\varepsilon_0\varepsilon_r} \qquad \text{(Equation 5.12)}$$

Equation 5.12 is referred as *Poisson's equation of electrostatics*. Table 5.1 shows Poisson's equation for different coordinate systems.

Table 5.1 Poisson's equation of electrostatics for different coordinate systems.

Coordinate system	**Equation**	**Equation #**
Rectangular (x, y, z)	$\frac{\partial^2\psi}{\partial x^2}+\frac{\partial^2\psi}{\partial y^2}+\frac{\partial^2\psi}{\partial z^2}=\frac{-\rho^*}{\varepsilon_0\varepsilon_r}$ $\rho^*=\rho^*(x,y,z)$	(Equation 5.13)
Cylindrical (r, θ, z)	$\frac{1}{r}\frac{\partial}{\partial r}\left(r\frac{\partial\psi}{\partial r}\right)+\frac{1}{r^2}\frac{\partial^2\psi}{\partial\theta^2}+\frac{\partial^2\psi}{\partial z^2}=\frac{-\rho^*}{\varepsilon_0\varepsilon_r}$ $\rho^*=\rho^*(r,\theta,z)$	(Equation 5.14)
Spherical (r, θ, ϕ)	$\frac{1}{r^2}\frac{\partial}{\partial r}\left(r^2\frac{\partial\psi}{\partial r}\right)+\frac{1}{r^2\sin\theta}\frac{\partial}{\partial\theta}\left(\sin\theta\frac{\partial\psi}{\partial\theta}\right)+\frac{1}{r^2\sin^2\theta}\frac{\partial^2\psi}{\partial\phi^2}=\frac{-\rho^*}{\varepsilon_0\varepsilon_r}$ $\rho^*=\rho^*(r,\theta,\phi)$	(Equation 5.15)

5.3.2. Poisson-Boltzmann equation

As can be seen in Table 5.1, ρ^* is basically a function of spatial coordinates, but it can be also expressed as a function of ψ, which would allow us solve Equations 5.13-5.15 for ψ. In order to do so, the ion concentrations should be described in terms of ψ according to Boltzmann distribution. Given that the work required to bring an ion from the bulk solution (i.e. infinitely far distance from the charged surface) to a position with potential ψ is equivalent to $z_i e\psi$; the Boltzmann distribution of ions can be expressed as follows

$$n_i = n_{i\infty} \exp\left(\frac{-z_i e\psi}{k_B T}\right) \qquad \text{(Equation 5.16)}$$

where $n_{i\infty}$, z_i, e, k_B, and T are the number of ions in the bulk solution (per cubic meter), ion valence number, elementary charge, Boltzmann constant, and absolute temperature (i.e. temperature in kelvins). It can be assumed that ρ^* is related to n_i as follows

$$\rho^* = \sum_i z_i e n_i \qquad \text{(Equation 5.17)}$$

Substituting Equation 5.16 into Equation 5.17 yields

$$\rho^* = \sum_i z_i e n_{i\infty} \exp\left(\frac{-z_i e\psi}{k_B T}\right) \qquad \text{(Equation 5.18)}$$

Finally, substituting Equation 5.18 into Equation 5.12 yields

$$\nabla^2\psi = \frac{-e}{\varepsilon_0 \varepsilon_r} \sum_i z_i n_{i\infty} \exp\left(\frac{-z_i e\psi}{k_B T}\right) \qquad \text{(Equation 5.19)}$$

Equation 5.19 is referred as *Poisson-Boltzmann equation*.

5.3.3. The Debye-Hückel approximation

It has been assumed in section 5.3.2 that ρ^* is made up of charges associated with various ion concentrations, which combine in an additive manner (as per Equation 5.17); nevertheless, Boltzmann distribution involves an exponential relationship between these charges and ψ. In this way, a fundamental inconsistency is introduced in the derivation of Poisson-Boltzmann equation (Equation 5.19), and as a result; Equation 5.19 does not have an explicit general solution anyhow and must be solved for certain limiting cases. These cases involve approximations that – at the same time – overcome the objection just stated [47]. The earliest of these approximations is the *Debye-Hückel approximation*.

The Debye-Hückel approximation is applicable for low $(z_i e\psi < k_B T)$. In this case, the exponential part of Equation 5.19 can be expanded as a power series, and provided that the power series expansion of $\exp(x)$ is given as

$$\exp(x) = \sum_{n=0}^{\infty} \frac{x^n}{n!} = 1 + x + \frac{x^2}{2!} + \frac{x^3}{3!} + \cdots$$

then expanding Equation 5.19 for the first two power series terms yields

$$\nabla^2\psi = \frac{-e}{\varepsilon_0 \varepsilon_r} \sum_i z_i n_{i\infty} \left(1 - \frac{z_i e\psi}{k_B T}\right)$$

$$\nabla^2\psi = \frac{-e}{\varepsilon_0 \varepsilon_r} \left[\sum_i z_i n_{i\infty} - \sum_i \frac{z_i^2 n_{i\infty} e\psi}{k_B T}\right] \qquad \text{(Equation 5.20)}$$

Because electroneutrality of solutions requires that

$$\sum_i z_i n_{i\infty} = 0$$

then Equation 5.20 becomes

$$\nabla^2\psi = \left[\frac{e^2}{\varepsilon_0\varepsilon_r k_B T}\sum_i z_i^2 n_{i\infty}\right]\psi \qquad \text{(Equation 5.21)}$$

Equation 5.21 is referred as the *linearized Poisson-Boltzmann equation*. It is convenient to identify the cluster of constants in Equation 5.21 by the symbol κ^2, which is defined as follows

$$\kappa^2 = \frac{e^2}{\varepsilon_0\varepsilon_r k_B T}\sum_i z_i^2 n_{i\infty} \qquad \text{(Equation 5.22)}$$

With this change in notation, Equation 5.21 simply becomes

$$\nabla^2\psi = \kappa^2\psi \qquad \text{(Equation 5.23)}$$

Table 5.2 shows the linearized Poisson-Boltzmann equation for different coordinate systems.

Table 5.2 Linearized Poisson-Boltzmann equation for different coordinate systems.

Coordinate system	**Equation**	**Equation #**
Rectangular (x, y, z)	$\frac{\partial^2\psi}{\partial x^2} + \frac{\partial^2\psi}{\partial y^2} + \frac{\partial^2\psi}{\partial z^2} = \kappa^2\psi$	(Equation 5.24)
Cylindrical (r, θ, z)	$\frac{1}{r}\frac{\partial}{\partial r}\left(r\frac{\partial\psi}{\partial r}\right) + \frac{1}{r^2}\frac{\partial^2\psi}{\partial\theta^2} + \frac{\partial^2\psi}{\partial z^2} = \kappa^2\psi$	(Equation 5.25)
Spherical (r, θ, ϕ)	$\frac{1}{r^2}\frac{\partial}{\partial r}\left(r^2\frac{\partial\psi}{\partial r}\right) + \frac{1}{r^2\sin\theta}\frac{\partial}{\partial\theta}\left(\sin\theta\frac{\partial\psi}{\partial\theta}\right) + \frac{1}{r^2\sin^2\theta}\frac{\partial^2\psi}{\partial\phi^2} = \kappa^2\psi$	(Equation 5.26)

5.3.4. Gouy-Chapman model of the double layer

Let us consider a uniformly-charged flat surface in contact with an aqueous solution of 1:1 symmetric electrolyte like sodium chloride (NaCl). Next, let us assume that the surface is infinitely extending in the positive and negative y and z directions, and ψ is varying only in the positive x-direction. Applying Equation 5.24 for this system yields

$$\frac{d^2\psi}{dx^2} = \kappa^2\psi \qquad \text{(Equation 5.27)}$$

Equation 5.27 is a homogenous linear second-order constant-coefficient ordinary differential equation (ODE). The characteristic equation associated with Equation 5.27 is

$$r^2 - \kappa^2 = 0$$

with the roots $r_1 = \kappa$ and $r_2 = -\kappa$, and hence Equation 5.27 has a general solution of the form

$$\psi(x) = c_1 \exp(\kappa x) + c_2 \exp(-\kappa x) \qquad \text{(Equation 5.28)}$$

Next, we need to apply the boundary conditions for Equation 5.28 in order to evaluate c_1 and c_2. Starting with c_1, $\psi \to \infty$ as $x \to \infty$; therefore, we should impose $c_1 = 0$. Next, $\psi \to \psi_0$ as $x \to 0$, and hence $c_2 = \psi_0$. Finally, we have

$$\psi(x) = \psi_0 \exp(-\kappa x) \qquad \text{(Equation 5.29)}$$

where ψ_0 is the potential at the charged surface.

5.3.5. Physical significance of the Debye-Hückel parameter κ

It has been shown in section 5.3.3 that parameter κ has evolved from the Debye-Hückel approximation without stating its physical interpretation. Since the exponent κx in Equation 5.29 is dimensionless, it can be inferred that κ must have the unit of reciprocal length (i.e. κ^{-1} has the unit of length). This κ^{-1} is known as *Debye length*; the distance over which the potential decreases by an exponential factor at low potentials [46]. It is also, imprecisely, called *thickness of the diffuse double layer* [46, 47]. All distances within the double layer are judged large or small relative to κ^{-1}.

As can be seen in Equation 5.22, κ depends on $n_{i\infty}$ (i.e. number of ions per cubic meter), and it would be practical if κ is expressed in terms of molarity (i.e. molar concentration; M = mol/L). Therefore, $n_{i\infty}$ can be related to the molar concentration of ions C_i and Avogadro's number N_A as follows

$$n_{i\infty} = 1{,}000\ C_i N_A \qquad \text{(Equation 5.30)}$$

where the number 1,000 is a conversion factor (1 m^3 = 1,000 L).

Substituting Equation 5.30 into Equation 5.22 yields

$$\kappa^2 = \frac{1{,}000\ N_A e^2}{\varepsilon_0 \varepsilon_r k_B T} \sum_i z_i^2 C_i \qquad \text{(Equation 5.31)}$$

Given that the ionic strength *I* of a solution is defined as follows

$$I = \frac{1}{2} \sum_i z_i^2 C_i \qquad \text{(Equation 5.32)}$$

then Equation 5.31 becomes

$$\kappa^2 = \frac{2{,}000\ N_A e^2 I}{\varepsilon_0 \varepsilon_r k_B T} \qquad \text{(Equation 5.33)}$$

Finally, κ^{-1} can be calculated as follows

$$\kappa^{-1} = \sqrt{\frac{\varepsilon_0 \varepsilon_r k_B T}{2{,}000\ N_A e^2 I}} \qquad \text{(Equation 5.34)}$$

5.3.6. Stern's model of the double layer

The treatment of the diffuse double layer according to the Gouy-Chapman model is based on assuming ions in the solution as if they were point charges. The nonzero-size of these ions will, however, limit the inner boundary of the diffuse part of the double layer because the hydrated radius of an ion prevents its center from approaching the charged surface without becoming specifically adsorbed [46].

In 1924, the German physicist Otto Stern proposed a model in which the double layer is divided into two parts; the *Stern layer* and *diffuse layer*. These two layers are virtually separated by a plane; the *Stern plane*, which is located at about a hydrated ion radius of magnitude δ from the charged surface followed by the diffuse layer that extends in the solution for a distance equivalent to κ^{-1}.

Furthermore, Stern also considered the possibility of specific ion adsorption. Specifically adsorbed ions are those attached to the charged surface with virtue of electrostatic and/or van der Waals forces strongly enough to overcome thermal agitation. The centers of these specifically adsorbed ions are located in the Stern layer (i.e. between the charged surface and the Stern plane) [46].

The Stern layer can be treated as if it were a parallel-plate capacitor; therefore, the potential changes linearly within it from ψ_0 (the surface or wall potential) to ψ_δ (the Stern potential) then decays exponentially from ψ_δ to zero within the diffuse layer as per Equation 5.29 (with ψ_0 replaced by ψ_δ) [46]. Figure 5.1 shows a schematic representation of Stern's model of the double layer.

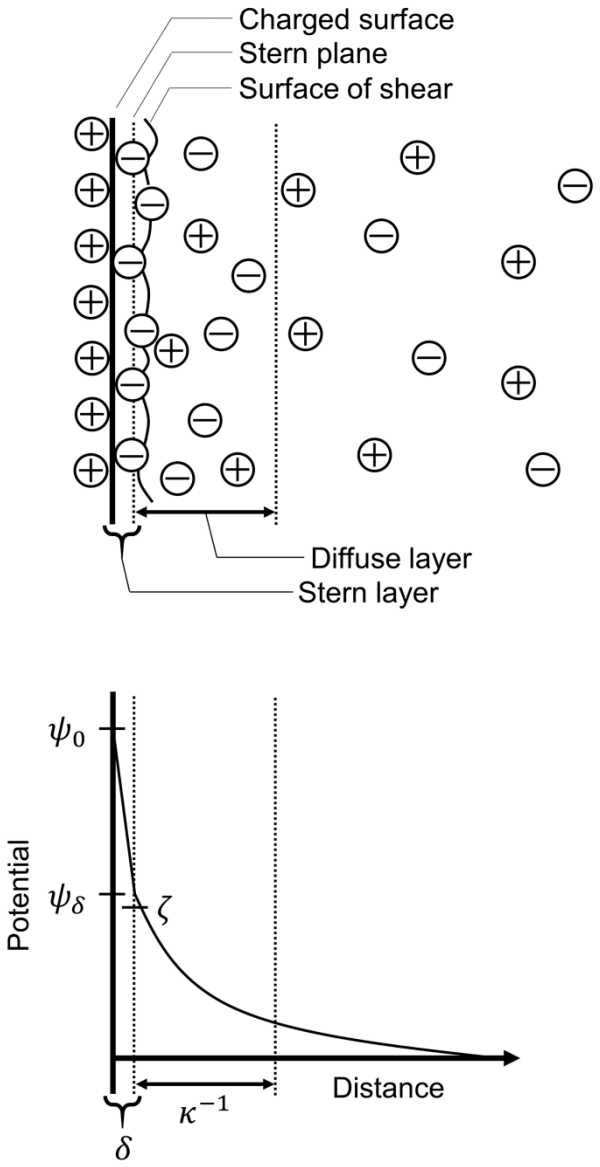

Figure 5.1 A schematic representation of the structure of the electric double layer according to Stern's theory.

As can be seen in Figure 5.1, when specific adsorption takes place, counter ion adsorption usually predominates over co-ion adsorption; nevertheless, it is possible for reversal of charge to take place within the Stern layer (i.e. ψ_0 and ψ_δ have opposite signs; Figure 5.2(a)) via adsorption of polyvalent or surface-active counter ions. Adsorption of surface-active co-ions could create a situation in which ψ_δ has the same sign as ψ_0 but is greater in magnitude as shown in Figure 5.2(b) [46].

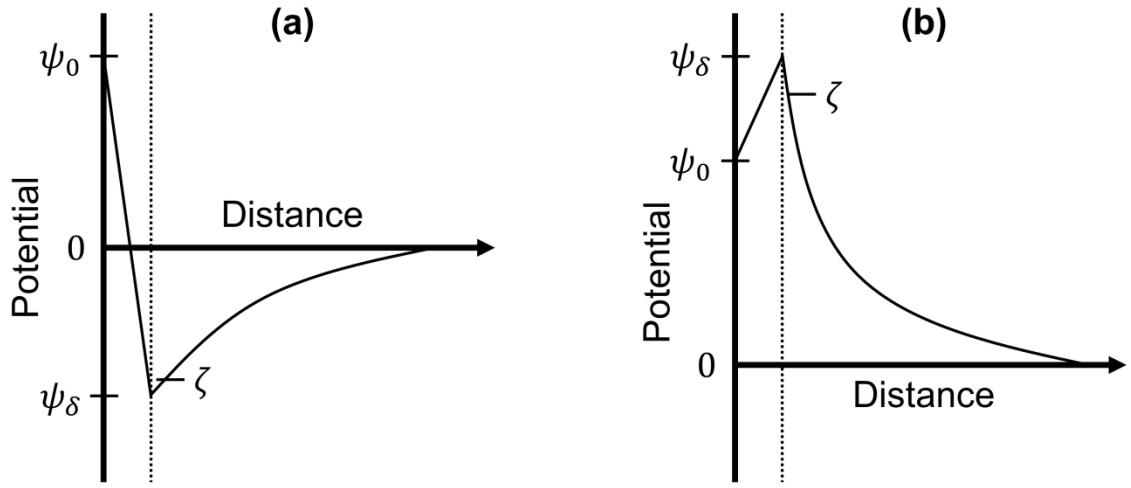

Figure 5.2 (a) Reversal of charge in the Stern layer due to adsorption of polyvalent or surface-active counter ions. (b) Effect of adsorption of surface-active co-ions in the Stern layer.

5.3.7. Electrokinetic potential

Let us consider a colloidal particle that is moving in a stagnant electrolyte solution. Part of the solution that is in contact with the surface of the colloidal particle is highly viscous and moves with it. At some distance from the surface, however, viscosity of the solution decreases and relative motion occurs giving rise to the *shear plane* (i.e. surface of shear; Figure 5.1) [48].

The relative motion of the particle and stagnant solution with respect to the outer portion of the diffuse layer and the bulk solution results in a potential difference across the shear plane [48]. This potential difference is referred as the *zeta potential*, which is usually denoted using the Greek letter zeta (ζ).

For curved surfaces, the shape of the double layer can be described in terms of the dimensionless parameter κa, which is the ratio of the radius of curvature a to the diffuse layer thickness κ^{-1}. As $\kappa a \to 0$, a charged particle tends to be a point charge, and as $\kappa a \to \infty$, the double layer becomes effectively flat. Let us consider a spherical Gaussian surface with radius r enclosing a spherical particle with radius a and surface charge q as shown in Figure 5.3. The net electric flux Φ of the electric field $\mathbf{E}$ permeating the Gaussian surface is given by Gauss's law;

$$\Phi = \oint \mathbf{E} \cdot d\mathbf{A} = \frac{q}{\varepsilon_0 \varepsilon_r} \qquad \text{(Equation 5.35)}$$

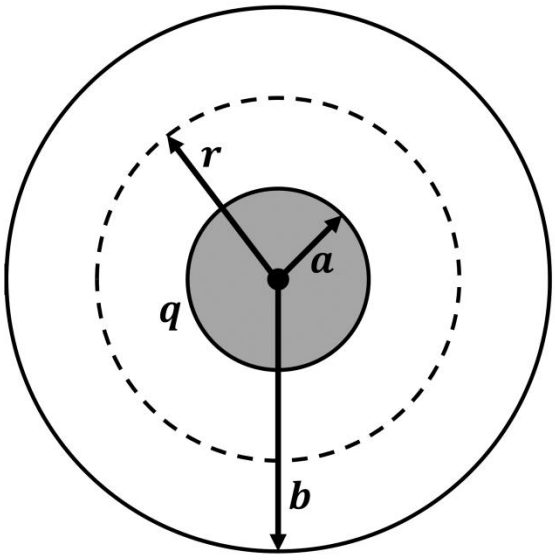

Figure 5.3 A cross-sectional diagram of a charged spherical particle of radius a bounded by a concentric spherical Gaussian surface of radius r ($a \leq r \leq b$).

The Gaussian surface will be such that whenever there is an electric flux through it, **E** will have a uniform magnitude E, and the vectors **E** and $d\mathbf{A}$ will be parallel. Therefore, Equation 5.35 becomes

$$E = \frac{q}{4\pi\varepsilon_0\varepsilon_r r^2} \qquad \text{(Equation 5.36)}$$

Assuming that the potential ψ changes only in the radial direction, and given that E is the negative gradient of ψ, Equation 5.36 becomes

$$\frac{d\psi}{dr} = \frac{-q}{4\pi\varepsilon_0\varepsilon_r r^2} \qquad \text{(Equation 5.37)}$$

Next, Equation 5.37 is a separable ODE, which can be integrated by imposing the following integration limits: $\psi \to \psi_0$ as $r \to a$, and $\psi \to 0$ as $r \to b$;

$$\int_{\psi_0}^{0} d\psi = \frac{-q}{4\pi\varepsilon_0\varepsilon_r}\int_{a}^{b}\frac{1}{r^2}dr$$

$$\psi_0 = \frac{q}{4\pi\varepsilon_0\varepsilon_r}\left(\frac{1}{a} - \frac{1}{b}\right) \qquad \text{(Equation 5.38)}$$

and given that

$$b = a + \kappa^{-1} = \frac{\kappa a + 1}{\kappa} \qquad \text{(Equation 5.39)}$$

then substituting Equation 5.39 into Equation 5.38 and setting $\psi_0 = \zeta$ yields

$$\zeta = \frac{q}{4\pi\varepsilon_0\varepsilon_r a(\kappa a + 1)} \qquad \text{(Equation 5.40)}$$

The stability of colloidal systems can be predicted by conducting electrokinetic studies. These studies involve various techniques that are aimed at calculating ζ. The most common of these techniques is *electrophoresis* in which ζ is determined by measuring the *electrophoretic velocity* v_E; the velocity at which the charged particles move in the solution when an electric field is applied. Figure 5.4 shows a schematic of the experimental setup of an electrophoresis cell.

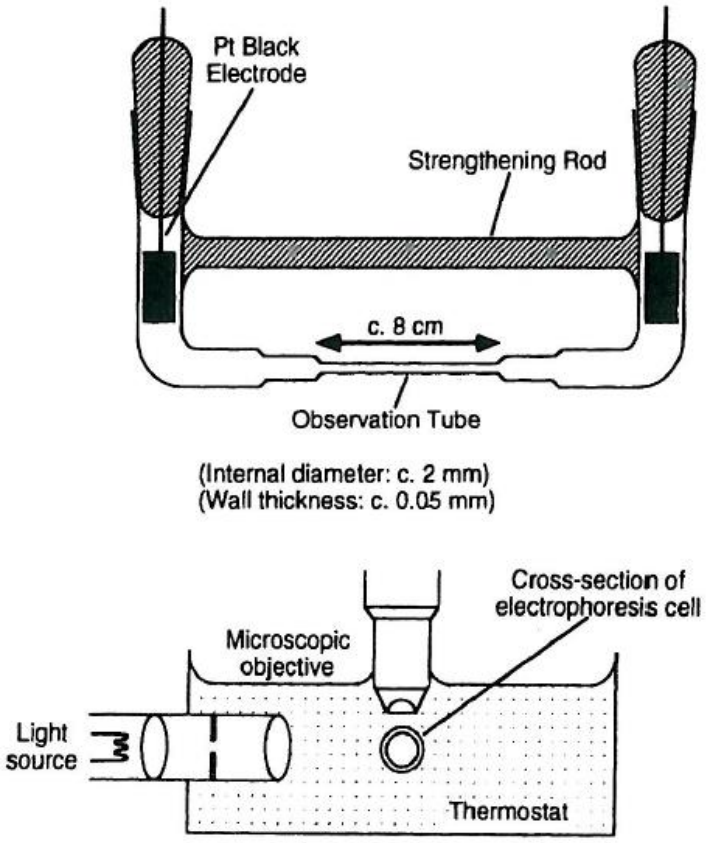

Figure 5.4 A schematic of a typical electrophoresis cell. [49]

The electric force on the charged particle due to E is given by $F_E = qE$, and the drag force resulting from the movement of the particle in the solution at very low Reynolds's number (laminar flow) is given by Stokes's law; $F_D = 6\pi a\eta v_E$, where η is the dynamic viscosity of the

solution. Assuming the particle is moving at constant velocity v_E, then F_E and F_D balance each other, and thus we have

$$q = \frac{6\pi a \eta v_E}{E} \qquad \text{(Equation 5.41)}$$

Substituting Equation 5.41 into Equation 5.40 yields

$$\zeta = \frac{3\eta v_E}{2\varepsilon_0 \varepsilon_r (\kappa a + 1) E} \qquad \text{(Equation 5.42)}$$

and given that the electrophoretic mobility u_E is defined as $u_E = v_E/E$, then Equation 5.42 finally becomes

$$\zeta = \frac{3\eta u_E}{2\varepsilon_0 \varepsilon_r (\kappa a + 1)} \qquad \text{(Equation 5.43)}$$

There are two approximations for Equation 5.43; the *Hückel approximation* ($\kappa a \ll 1$) and the *Smoluchowski approximation* ($\kappa a > 100$). Under the condition of the Hückel approximation, Equation 5.43 reduces to

$$\zeta = \frac{3\eta u_E}{2\varepsilon_0 \varepsilon_r} \qquad \text{(Equation 5.44)}$$

Equation 5.44 does not usually apply to particles in aqueous solutions; a particle of radius 10 nm in a 1:1 aqueous electrolyte would require an electrolyte concentration as low as 10^{-5} M so that $\kappa a = 0.1$. However, under the Smoluchowski approximation, it was found that Equation 5.43 could be best approximated as

$$\zeta = \frac{\eta u_E}{\varepsilon_0 \varepsilon_r} \qquad \text{(Equation 5.45)}$$

It is worth noting that Equation 5.45 applies to colloidal particles of arbitrary shape and size [50].

5.4. The interaction potential energy determines the kinetic behavior

Let us consider two spherical colloidal particles of the same material and size separated by a surface-to-surface distance h as illustrated in Figure 5.5. We can identify interaction potential energy curves of the two general types shown in Figure 5.6. In Figure 5.6a, a monotonically decreasing free energy persists up to a primary minimum. No energy barrier prevents the system from reaching this minimum where particles achieve the bound state. The extent to which the particle association is reversible depends on the depth of the potential well and on possible further processes in the aggregated state [49]. A reversible association is often called *flocculation*, while an irreversible association is called *coagulation*. The distinction between both terms can be best explained by the interaction potential energy curve in Figure 5.6b.

As can be seen in Figure 5.6b, the curve exhibits two minima; a shallow secondary minimum at large distances, and a primary minimum at shorter distances. The former minimum corresponds to the flocculated state of the particles whereas the latter corresponds to the coagulated state. The maximum between the two minima serves as an energy barrier, which when it far exceeds $k_B T$, the primary minimum becomes inaccessible, and the system is said to be "kinetically stable". Stable aggregates are formed for sufficiently deep or wide interaction wells at sufficiently high particles concentrations [49].

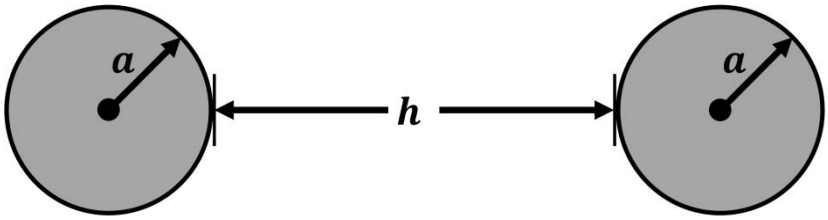

Figure 5.5 A schematic diagram of two spherical colloidal particles of radius a separated by a surface-to-surface distance h.

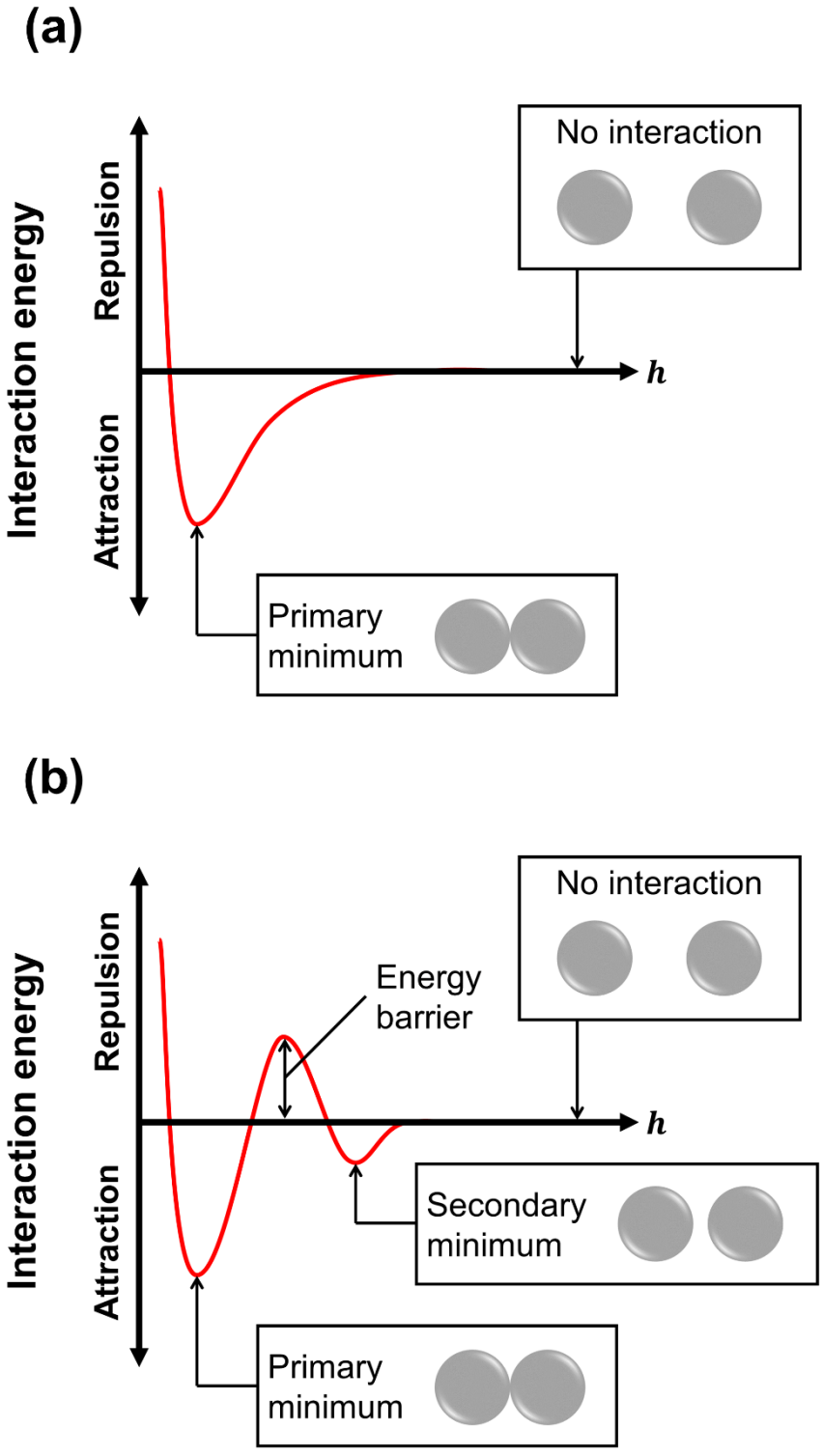

Figure 5.6 Interaction potential energy curves of two identical colloidal particles.

5.5. Extended DLVO theory

A major advance in colloid science occurred during the 1940s when two groups of scientists; Boris Derjaguin and Lev Landau, in the Soviet Union; Evert Verwey and Theo Overbeek, in the Netherlands; independently published a quantitative theoretical analysis of colloidal stability. The theory they proposed became known by the initial letters of their surnames; the DLVO theory [49].

In the classical DLVO theory, van der Waals interactions are the main attractive interactions that exist between colloidal particles, and the repulsive interactions exist between their similarly charged electric double layers. Nevertheless, the classical DLVO theory fails to model complex colloidal systems such as polymer-functionalized colloidal particles. Therefore, a more generic version of the DLVO theory had to be developed; the extended DLVO (XDLVO) theory, which takes into consideration other forms of interactions (e.g. magnetic, osmotic, and elastic-steric) in addition to the aforementioned van der Waals and electric double layer interactions [51].

In the case of CA-IONPs, we showed in Chapter 4 that CA-IONPs exhibit significant dipolar interactions when they are in dry powder form, and most probably in dense ferrofluids too. The magnetic energy of each particle i is composed of three parts: anisotropy energy, field energy, and interaction energy [52]. Table 5.3 lists the expressions for van der Waals interactions, electric double layer repulsions, and magnetic potential energy for two spherical superparamagnetic particles of radius a separated by a distance r_{ij}. Elastic-steric and osmotic interactions were not considered in this work due to the non-polymeric nature of the ligand [51]. The field energy is omitted under zero-field conditions. Finally, it should be realized that the many-body numerical simulation of the colloidal stability of CA-IONPs at high-particle concentrations is beyond the scope of this work. In the next chapter, we will solely focus on the

kinetic stability of CA-IONPs in high-salinity aqueous media, which is critical for subsurface applications.

Table 5.3 Interaction and potential energy equations for two identical spherical superparamagnetic particles.

Attribution	**Interaction/potential energy equation**	**Equation #**	**Reference**
Van der Waals attractive forces	$U_{VDW} = \frac{-A_{121}}{6}\left[\frac{2a^2}{r_{ij}(4a+r_{ij})} + \frac{2a^2}{(2a+r_{ij})^2} + \ln\frac{r_{ij}(4a+r_{ij})}{(2a+r_{ij})^2}\right]$	(Equation 5.46)†	[53]
Electric double layer repulsions	$U_{EDL} = 4\pi\varepsilon_0\varepsilon_r a\zeta^2 \frac{a+r_{ij}}{2a+r_{ij}} \ln\left[1+\frac{a}{a+r_{ij}}\exp(-\kappa r_{ij})\right]$	(Equation 5.47)††	[54]
Magnetic anisotropy	$U_{MA} = -\frac{4}{3}\pi K a^3 \left(\frac{\boldsymbol{\mu}_i \cdot \mathbf{n}_i}{\lvert\boldsymbol{\mu}_i\rvert}\right)^2$	(Equation 5.48)	[52]
Magnetic dipole in/with an applied magnetic field	$U_{DF} = -\boldsymbol{\mu}_i \cdot \mathbf{H}$	(Equation 5.49)	
Interacting magnetic dipoles	$U_{DD} = \frac{\boldsymbol{\mu}_i \cdot \boldsymbol{\mu}_j}{r_{ij}^3} - \frac{3(\boldsymbol{\mu}_i \cdot \mathbf{r}_{ij})(\boldsymbol{\mu}_j \cdot \mathbf{r}_{ij})}{r_{ij}^5}$	(Equation 5.50)	

†A_{121}: Hamaker constant.

††K: Magnetic anisotropy constant.

Chapter 6

Colloidal Stability of Citric Acid-functionalized Iron Oxide Nanoparticles in High-salinity Media

6.1. Introduction

The most pertinent challenge associated with the applicability of nanoparticles in subsurface applications is their colloidal stability in high-salinity environments [26]. This is because the high ionic strength of the constituent electrolytes compresses the electric double layers of the particles. Consequently, interparticle electric double layer repulsive forces are suppressed in favor of other attractive forces, such as van der Waals forces, and ultimately leading to particle coagulation. Moreover, we showed in Chapter 3 that high-magnetic susceptibilities (i.e. dense ferrofluids) are required to generate a considerable anomalous electromagnetic response. Therefore, the effect of magnetic dipolar interactions between CA-IONPs at high particle concentrations on their colloidal stability is of utmost importance, and thus it will be thoroughly investigated in this chapter.

6.2. Characterization and methodology

Dynamic light scattering (DLS) measurements were acquired with the Zetasizer Nano ZS (Malvern Panalytical) system using the non-invasive backscatter (NIBS) mode, the latter which was specifically developed for the analysis of dense particle dispersions [55]. For each measurement, 700 μL of an aqueous ferrofluid of CA-IONPs with a particle concentration twice the desired final value was freshly prepared, sonicated for 5 min, and mixed with 700 μL of a

sodium chloride (NaCl) solution with a concentration twice the desired salinity level. No significant pH variations were observed for all samples (pH = 5.5 ± 0.2). Then, 700 μL of the diluted saline ferrofluid was injected into a disposable folded capillary zeta cell (type DTS1060), and the cell was then immediately placed into the DLS chamber to collect the measurements.

For all size measurements, an equilibration time of 20 s was set prior to each measurement, and the data was collected every 15 s for 30 min at 25 °C. The z-average hydrodynamic radius (R_H) was then plotted against time (t) to generate the size evolution plots. The initial aggregation rate constant (k) was estimated by obtaining the initial slope of the size evolution plots [56, 57];

$$k \propto \frac{1}{N_0}\left(\frac{dR_H(t)}{dt}\right)_{t\to 0} \qquad \text{(Equation 6.1)}$$

where N_0 is the initial number concentration of the particles in the dispersion. The *attachment efficiency* (α), which is the reciprocal of the *stability ratio* (W), was used to quantify the aggregation kinetics of CA-IONPs, and it is given as follows

$$\alpha = \frac{1}{W} = \frac{k}{k_{\text{fast}}} \qquad \text{(Equation 6.2)}$$

where k_{fast} is the aggregation rate constant evaluated at the ionic strength (i.e. salinity level) where the slope of the size evolution plot is maximum, and nearly ceases to increase with further increase in ionic strength [58]. Conventionally, the ionic strength region where α approaches unity is referred to as the *fast aggregation* or *diffusion-limited cluster aggregation* (DLCA) regime, whereas the one where α is less than unity as the *slow aggregation* or *reaction-limited cluster aggregation* (RLCA) regime. In the cases where aggregation had already started before

the first measurement (i.e. measured R_H value at 15 s), k was estimated to be equivalent to the slopes of the size evolution plots for time periods between 200 and 1800 s.

For the zeta potential measurements, all samples were prepared using the same previous procedure. An equilibration time of 20 s was set prior to each measurement, and all measurements were recorded at 25 °C. The number of scans was adjusted according to the state of particle aggregation; high (10-100 scans) and low (10-25 scans) for slow and fast aggregation kinetics, respectively. Finally, we are assuming in this work the NaCl content of seawater to be 600 mM.

6.3. Results and discussion

6.3.1. Effect of particle concentration on aggregation kinetics

Figures 6.1a-d show the size evolutions of CA-IONPs with time over a broad range of NaCl concentrations (1 mM – 2 M), and at different particle concentrations (1, 100, 200 mg/L, and 1 g/L). A remarkable increase in the first measurements (Figure 6.2) is observed at salinity levels of 200 mM and above, which implies that aggregation has already progressed during the courses of equilibration and first measurement. The low-salinity (< 100 mM) size measurements shown in Figure 6.2 are notably higher than the values reported in the size distribution obtained from TEM analysis (Figure 4.3b). This can be attributed to the intrinsic tendency of IONPs to aggregate and form stable clusters, especially when the steric repulsions due the capping agent are weak [59, 60]. Furthermore, it seems that the cluster size evolution is proportional to the initial particle concentration, which is consistent with the theoretical prediction of the second-order dependence of the aggregation rate on the initial particle number concentration [49, 61]. Another notable observation is the sharp increase in R_H for the 1 g/L sample at 600 mM (Figure

6.1d). This suggests that the aggregation of CA-IONP clusters is, in fact, a two-regime process as illustrated in Figure 6.3 [61]. In the first regime, CA-IONP clusters aggregate to form micron-size aggregates, which, in the second regime, link into chains that can eventually form a percolated gel network.

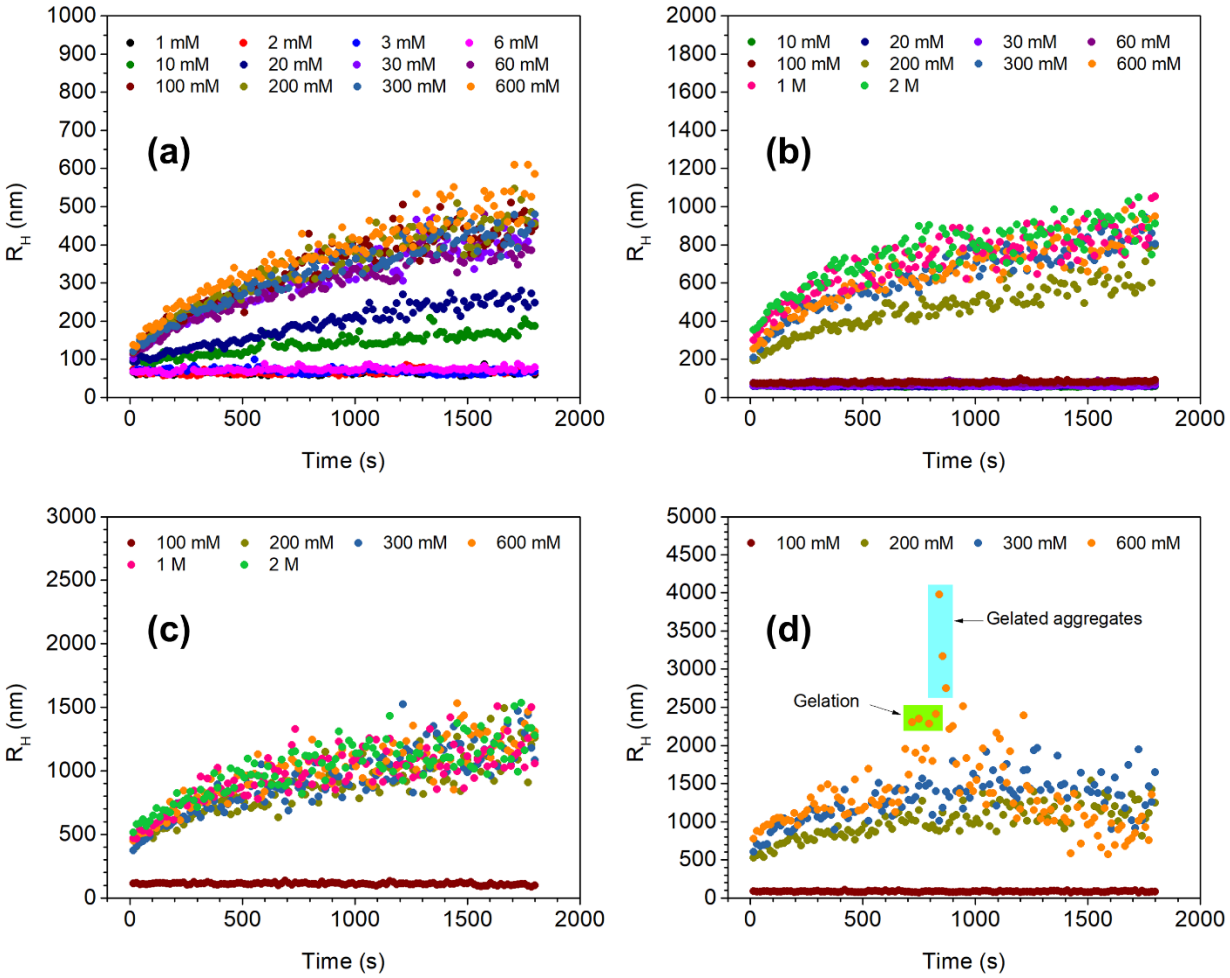

Figure 6.1 Size evolutions of CA-IONP clusters with time over a broad range of NaCl concentrations (1 mM – 2 M), and at different particle concentrations: 10 mg/L (a), 100 mg/L (b), 200 mg/L (c), and 1 g/L (d).

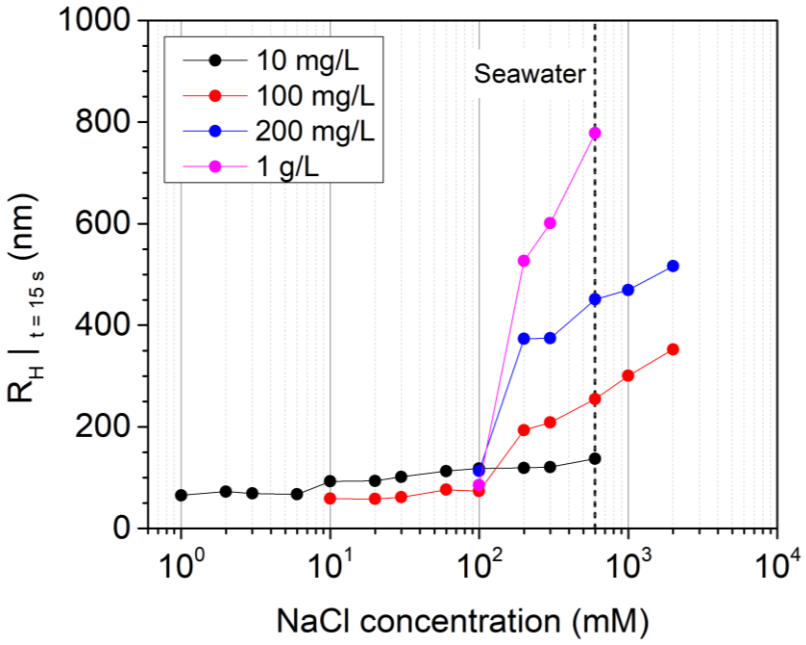

Figure 6.2 Hydrodynamic radius of CA-IONP clusters at t = 15 s as a function of NaCl concentration at different particle concentrations.

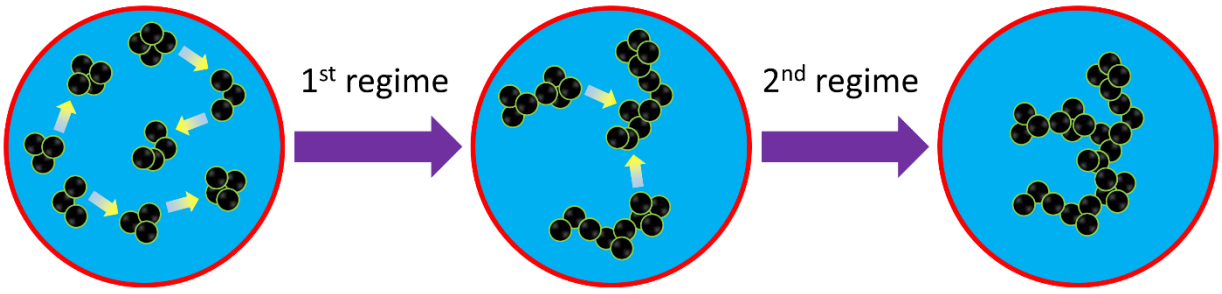

Figure 6.3 Proposed aggregation mechanism of CA-IONP clusters at sufficiently high particle concentrations.

The aggregation and gelation kinetics of CA-IONP clusters can be better quantitatively explained with the aid of the α-versus-NaCl concentration plot. As can be seen in Figure 6.4, at the lowest particle concentration (10 mg/L), the clusters exhibit no aggregation ($\alpha \approx 0$) when the salinity level is 6 mM and below. The intersection of the linear regression lines of the RLCA (10-30 mM) and DLCA (30-600 mM) regimes gives the *critical coagulation concentration* (CCC); the minimum concentration of counter ions (Na^+ in this case) required to induce the coagulation of the CA-IONP clusters. The CCC was found to be 34 mM, which is slightly above the value reported in the literature [58]. At higher particle concentrations, the upper limit of the no-aggregation regime is shifted to 100 mM. This is expected as more counter ions are required to suppress the electrostatic electric double layer repulsive forces in favor of van der Waals and magnetic dipolar interactions at high particle concentrations. Another interesting observation for the dense samples is that the ionic strength at gelation (300 mM) is independent of particle concentration, beyond which cluster-cluster aggregation eventually slows down with particle concentration. This is due to the fact that percolation time of gelated aggregates decreases with particle concentration, and accordingly slowing down the aggregate diffusion rate in highly percolated gel networks [62]. Figure 6.5 illustrates the percolation mechanisms in dilute and dense colloidal systems.

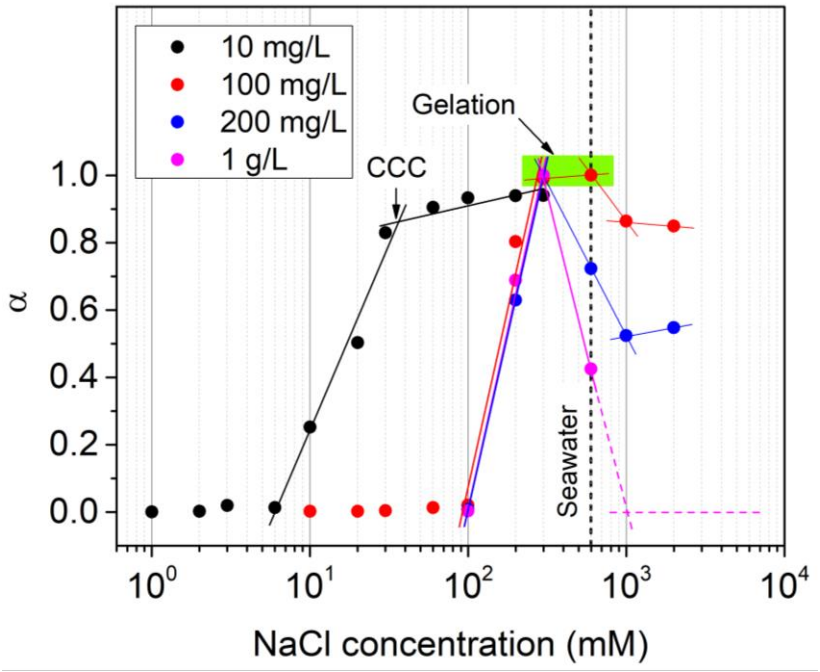

Figure 6.4 Plot of the CA-IONP cluster-cluster attachment efficiency α as a function of NaCl concentration at different particle concentrations.

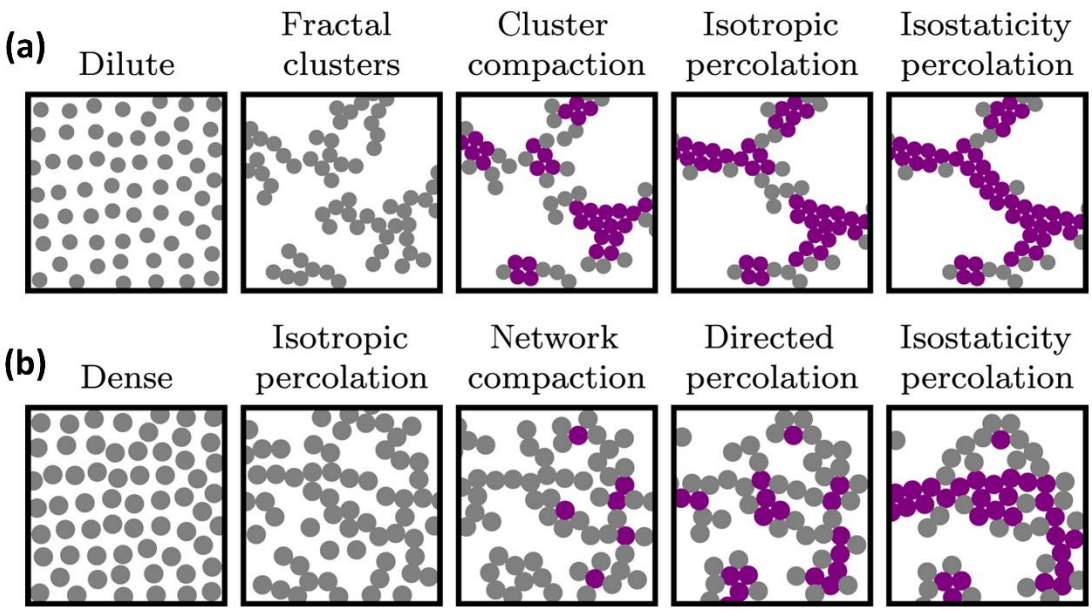

Figure 6.5 Proposed percolation mechanisms for the formation of a mechanically stable gel. (a) Dilute colloid. (b) Dense colloid. Isostatic particles are shown in purple, whereas non-isostatic particles are in gray [62].

6.3.2. Effect of particle concentration on zeta potential

In order to convert the measured electrophoretic mobilities to apparent zeta potentials (ζ), first we need to estimate the value of the κa parameter. However, due to the polydisperse nature of CA-IONPs, we are assuming in this work CA-IONP clusters with a mean radius (a) equivalent to R_H at 15 s (Figure 6.2). Debye length (κ^{-1}) was calculated using Equation 5.34, and plotted as a function of NaCl concentration as shown in Figure 6.6. The $\kappa R_H|_{t\,=\,15\,\mathrm{s}}$ plot corresponding to Figures 6.2 and 6.6 is shown in Figure 6.7. As can be seen in Figure 6.7, $\kappa R_H|_{t\,=\,15\,\mathrm{s}}$ deviates from unity by several orders of magnitude, and hence Smoluchowski's equation (Equation 5.45) was used to calculate ζ, which also applies to colloidal particles of arbitrary shape and size [50].

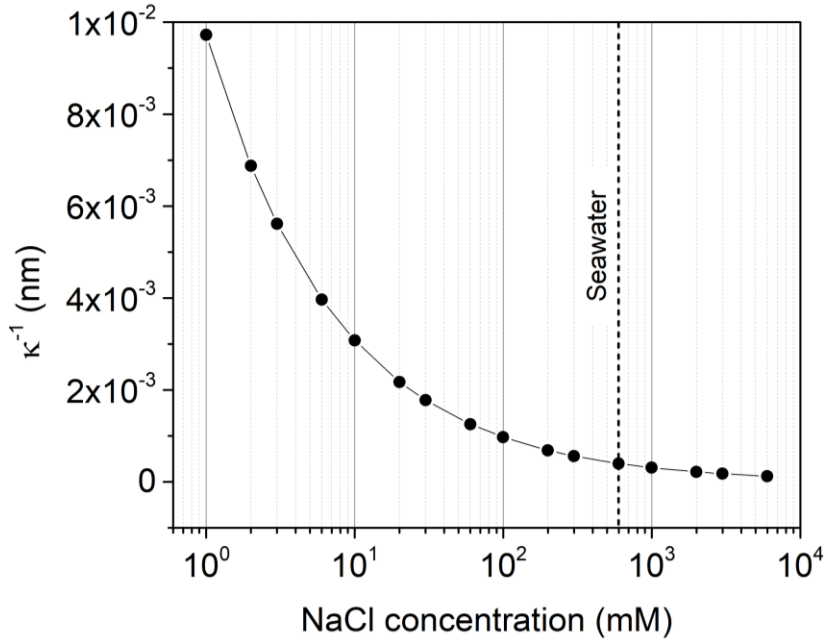

Figure 6.6 Debye length as a function of NaCl concentration.

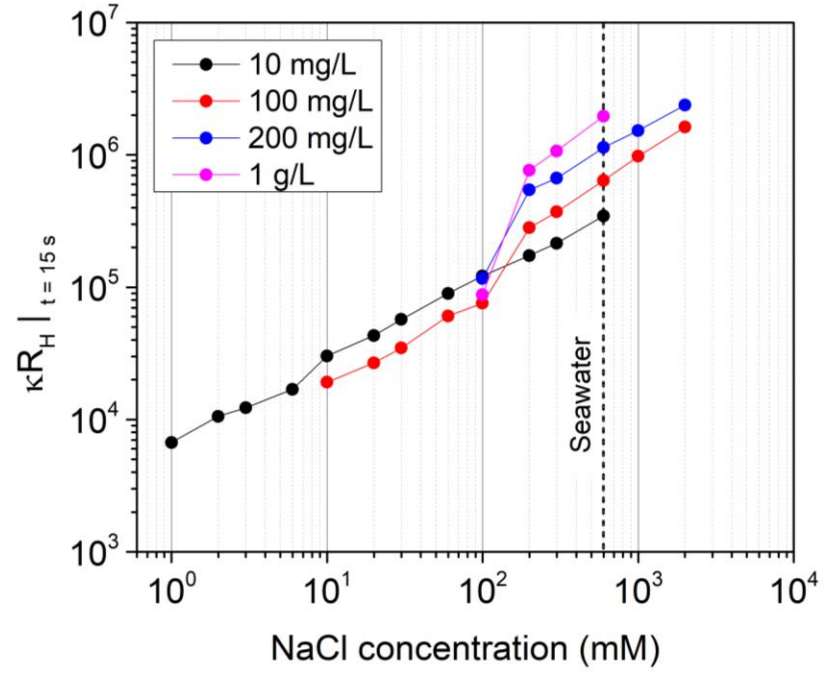

Figure 6.7 Plot of $\kappa R_H|_{t\,=\,15\,s}$ as a function of NaCl concentration at different particle concentrations.

As can be seen in Figure 6.8, for the diluted sample (10 mg/L), an increase in the concentration of Na^+ ions reduces the magnitude of ζ from an initial value of -15.0 ± 1.5 mV in the no-aggregation regime (1-6 mM) to a plateau value of -6.5 ± 0.8 mV in the DLCA regime (30-600 mM). Nevertheless, a significant increase in the magnitude of ζ can be observed with the increase of particle concentration, which seems to reach a maximum initial plateau value of -40.0 ± 1.6 mV at a particle concentration of 1 g/L. Evidently, this significant increase in ζ is due to the high particle concentration-to-counter ion concentration ratio. This results in the dominance of interparticle electrostatic electric double layer repulsive forces over van der Waals and magnetic dipolar interactions, which ultimately confirms our previous finding of the enhanced colloidal stability of the CA-IONP clusters at high particle concentrations and high NaCl concentrations (up to 100 mM).

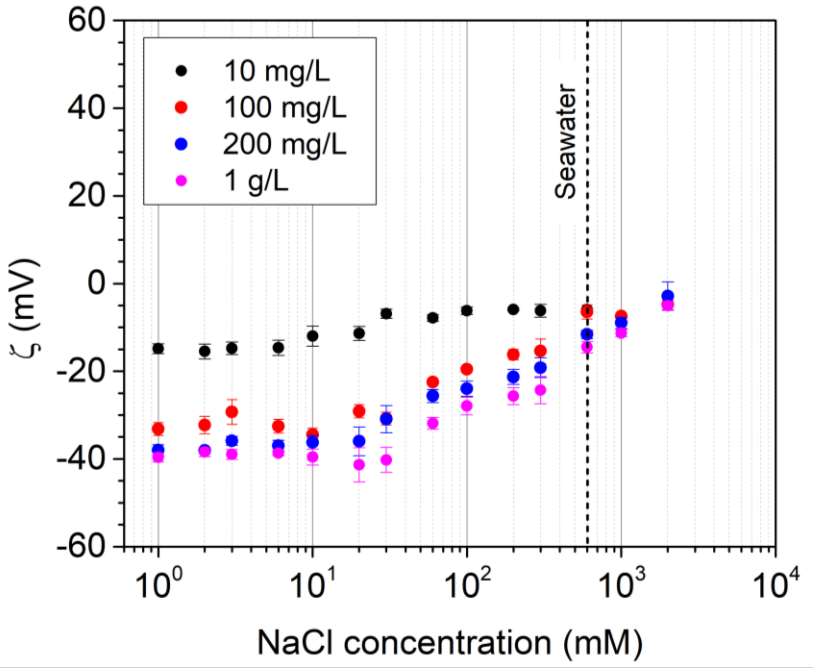

Figure 6.8 Plot of the zeta potential of CA-IONP clusters as a function of NaCl concentration at different particle concentrations.

6.4. Conclusions

The aggregation kinetics of CA-IONPs in high-salinity media have been thoroughly investigated. Magnetic dipolar interactions seem to diminish in favor of electrostatic electric double layer repulsions with the increase of particle concentration. This, in turn, enhances the colloidal stability of CA-IONP clusters in dense aqueous ferrofluids, and at salinity levels up to 100 mM (6-times diluted seawater). Therefore, low-salinity water-based dense ferrofluids of CA-IONP clusters are indeed economically feasible for potential subsurface applications owing to their remarkable high colloidal stability at low seawater dilutions [63].

Chapter 7

Summary and Future Prospects

7.1. Summary

In this work, the use of MNPs as contrast agents for large-scale imaging of reservoirs was thoroughly explored within the frameworks of electromagnetic theory, geophysical finite element simulations, and material development. Starting with the geophysical simulations, it was shown that magnetic permeability-based crosswell EMT is applicable at audio frequencies, and for crosswell distances of a minimum of one skin depth. Moreover, a semi-empirical model depicting the magnetic susceptibility of the injected ferrofluid as a function of residual oil saturation and rock porosity was developed. As a rule of thumb, this model predicts the minimum magnetic susceptibility of the injected ferrofluid required to generate an effective magnetic permeability twice that of the background.

It is also worth noting that the research presented in this dissertation is, in fact, the first to experimentally prove the feasibility of the proposed technology from a material development point of view. In this regard, a facile large-scale low-cost synthesis of CA-IONPs exhibiting excellent dispersibility in aqueous media at very high particle concentrations up to 2 kg/L (67 wt%) was reported. Furthermore, CA-IONP clusters were found to exhibit a remarkable colloidal stability at high particle concentrations, and at salinity levels up to 100 mM. This, in turn, facilitates the injection of dense ferrofluids of CA-IONPs into the reservoir, and makes it economically feasible due to the low number of seawater dilutions required to produce the aqueous carrier fluid.

7.2. Future prospects

7.2.1. Design optimization and imaging of complex structures

One of the proposed future studies is to investigate the signal sensitivity to the magnetic susceptibility of the propagating magnetic anomaly. The study will be aiming at determining the minimum effective permeability required to generate a detectable anomalous response for different crosswell distance-to-anomaly height aspect ratios. This will help us better optimize the proposed design of the crosswell EMT system to achieve detectability at low ferrofluid injection volumes and realistic particle concentrations, and thus making the deployment of the technology more economically feasible. The attainability of detectable particle concentrations can be justified with the aid of vibrating sample magnetometry (VSM) measurements to determine the initial magnetic susceptibility of the developed ferrofluid at different particle concentrations.

Another proposed future study is associated with the imaging of structurally complex reservoirs. This is because the imposition of a magnetic anomaly, whose dimensions are assumed to remain conserved during the course of propagation, is evidently very optimistic. Instead, complex geometries, such as fault arrays and fracture networks, should be taken into consideration in addition to variations in water and residual oil saturations.

7.2.2. One-borehole EMT system

Another interesting proposed future study is concerned with the potential application of a one-borehole magnetic permeability-based EMT system. Briefly, in this proposed EMT system, a single antenna on which both transmitting and receiver coils are mounted (Figure 7.1) is deployed in a borehole. The principle of operation lies in monitoring the propagation of a magnetic anomaly by monitoring the variations in the differential magnetic field amplitude (ΔH_{z0}), that is the measured magnetic field amplitude after background subtraction, with respect to the vertical scanning distance. Advanced inversion algorithms are employed for the inversion of the acquired 1D EM data as illustrated in Figure 7.2.

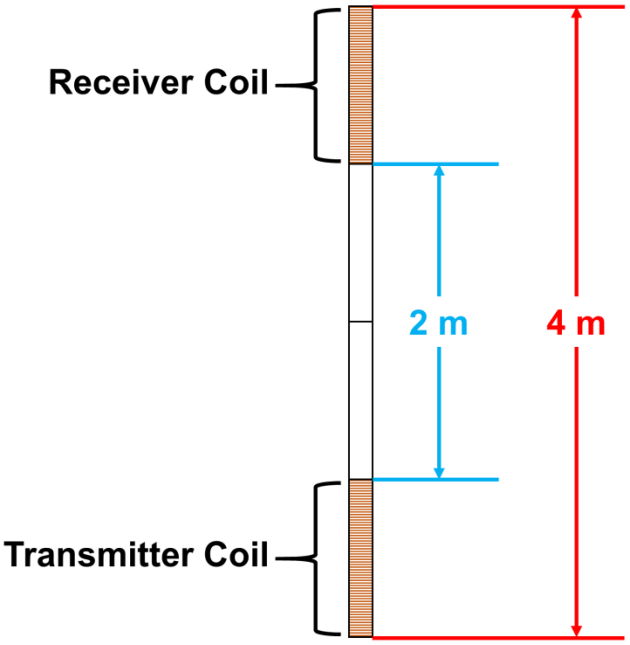

Figure 7.1 A proposed design of one-borehole EMT antenna.

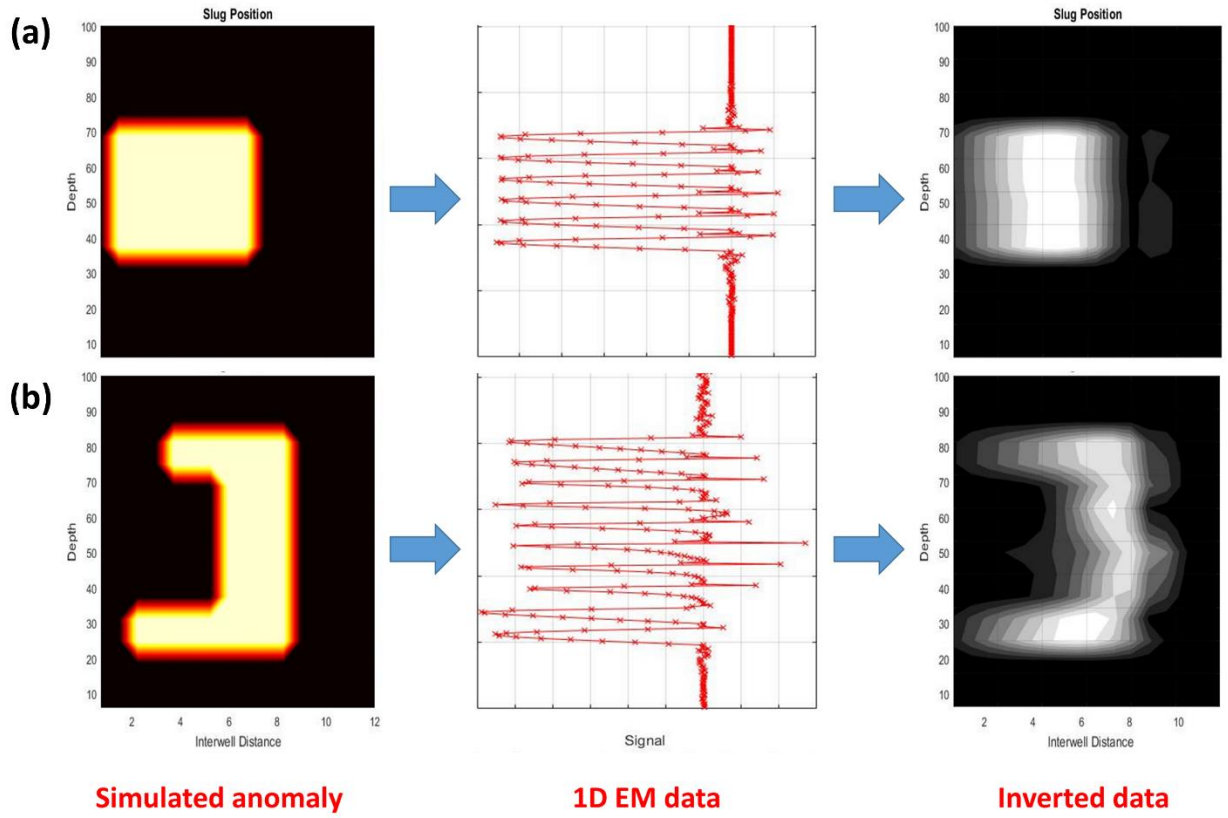

Figure 7.2 One-borehole EMT for the imaging of simple (a) and complex (b) reservoir structures.

7.2.3. Magnetic hyperthermia

The potential application of CA-IONPs in magnetic hyperthermia was briefly explored. Figure 7.3 shows the temperature increase in aqueous ferrofluids of CA-IONPs at various particle concentrations in a field intensity of 100 G oscillating at 267 kHz. The concentration dependence of the maximum temperature ($T_{\max}$) and specific absorption rate (SAR) are depicted in Figures 7.4 and 7.5, respectively. The influence of field intensity and frequency on the concentration dependence of $T_{\max}$ and SAR will be thoroughly examined in the future.

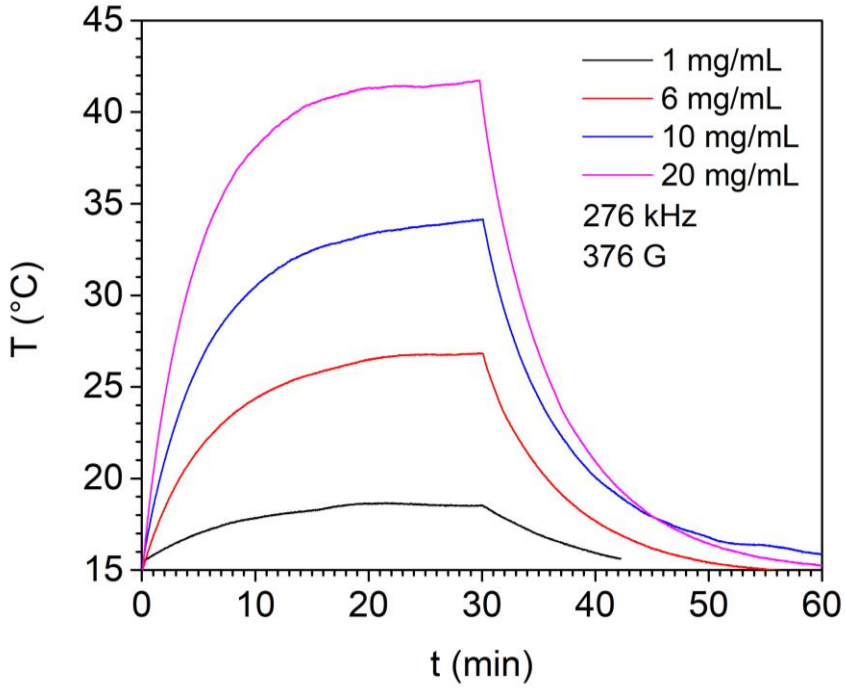

Figure 7.3 Temperature increase in aqueous ferrofluids of CA-IONPs at different particle concentrations.

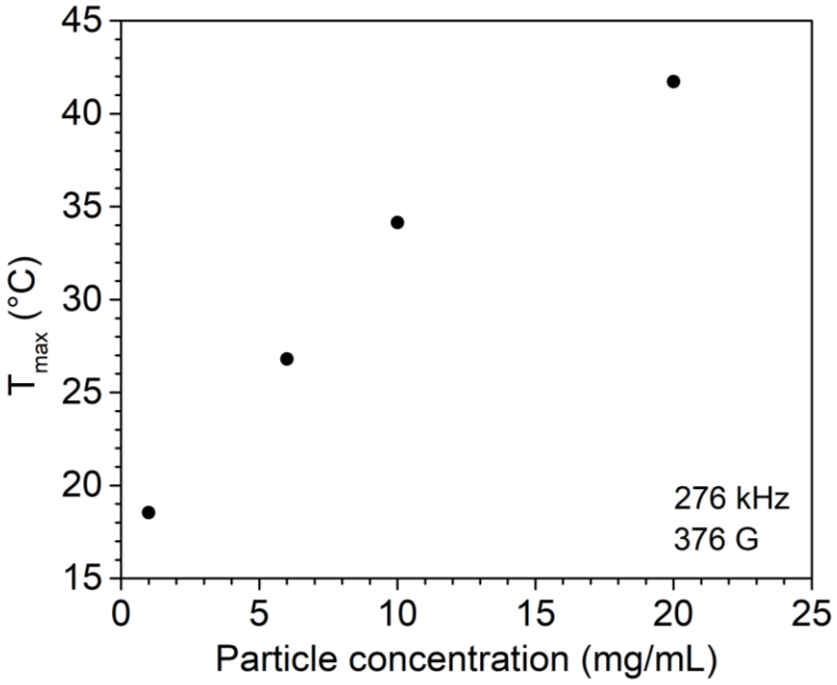

Figure 7.4 Concentration dependence of the maximum temperature.

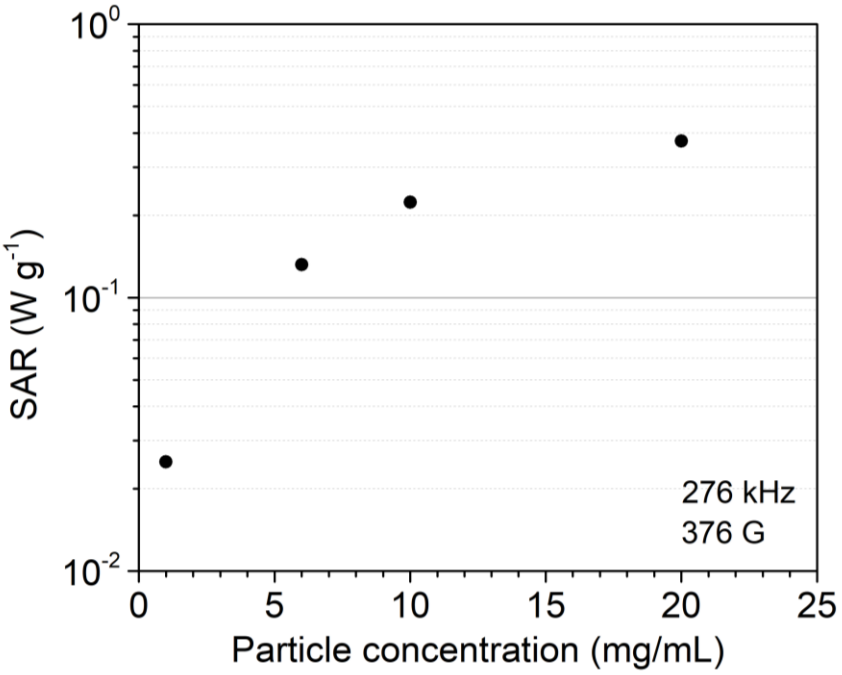

Figure 7.5 Concentration dependence of the specific absorption rate.

References

[1] D. Pouliquen, J. J. Le Jeune, R. Perdrisot, A. Ermias, and P. Jallet, "Iron oxide nanoparticles for use as an MRI contrast agent: Pharmacokinetics and metabolism," *Magnetic Resonance Imaging*, vol. 9, pp. 275-283, 1991/01/01/ 1991.

[2] Y.-X. J. Wang, S. M. Hussain, and G. P. Krestin, "Superparamagnetic iron oxide contrast agents: physicochemical characteristics and applications in MR imaging," *European Radiology*, vol. 11, pp. 2319-2331, 2001/11/01 2001.

[3] K. R. Wierzbinski, T. Szymanski, N. Rozwadowska, J. D. Rybka, A. Zimna, T. Zalewski, *et al.*, "Potential use of superparamagnetic iron oxide nanoparticles for in vitro and in vivo bioimaging of human myoblasts," *Scientific Reports*, vol. 8, p. 3682, 2018/02/27 2018.

[4] W. Tan and X. Fang, *Aptamers Selected by Cell-SELEX for Theranostics*: Springer Berlin Heidelberg, 2015.

[5] A. Rahmani, S. Bryant, C. Huh, A. Athey, M. Ahmadian, J. Chen, *et al.*, "Crosswell Magnetic Sensing of Superparamagnetic Nanoparticles for Subsurface Applications," *SPE Journal*, vol. 1, 09/30 2013.

[6] A. Rahmani, S. Bryant, C. Huh, M. Ahmadian, W. Zhang, and Q. Liu, "Characterizing Reservoir Heterogeneities Using Magnetic Nanoparticles," *Society of Petroleum Engineers - SPE Reservoir Simulation Symposium 2015*, vol. 1, pp. 74-102, 01/01 2015.

[7] G. J. Lichtenberger, "Field Applications of Interwell Tracers for Reservoir Characterization of Enhanced Oil Recovery Pilot Areas," presented at the SPE Production Operations Symposium, Oklahoma City, Oklahoma, 1991.

[8] S. H. Elahi and B. Jafarpour, "Dynamic Fracture Characterization From Tracer-Test and Flow-Rate Data With Ensemble Kalman Filter," *SPE Journal*, vol. 23, pp. 449-466, 2018/4/1/ 2018.

[9] L. Guan, Y. Du, S. G. Johnson, and M. K. Choudhary, "Advances of Interwell Tracer Analysis in the Petroleum Industry," *Journal of Canadian Petroleum Technology - J CAN PETROL TECHNOL*, vol. 44, 05/01 2005.

[10] C. Serres-Piole, H. Preud'homme, N. Moradi-Tehrani, C. Allanic, H. Jullia, and R. Lobinski, "Water tracers in oilfield applications: Guidelines," *Journal of Petroleum Science and Engineering*, vol. 98-99, pp. 22-39, 2012/11/01/ 2012.

[11] S. Semenov, R. Planas, M. Hopfer, A. Hamidipour, A. Vasilenko, E. Stoegmann, *et al.*, "Electromagnetic tomography for brain imaging: Initial assessment for stroke detection," in *2015 IEEE Biomedical Circuits and Systems Conference (BioCAS)*, 2015, pp. 1-4.

[12] M. Mallach, M. Gevers, P. Gebhardt, and T. Musch, "Fast and Precise Soft-Field Electromagnetic Tomography Systems for Multiphase Flow Imaging," *Energies*, vol. 11, p. 1199, 05/09 2018.

[13] B. R. Spies, "Survey design considerations for cross-well electromagnetics," *Seg Technical Program Expanded Abstracts*, vol. 11, 01/01 1992.

[14] A. G. Nekut, "Crosswell electromagnetic tomography in steel-cased wells," *GEOPHYSICS,* vol. 60, pp. 912-920, 1995.

[15] J. C. Maxwell, "VIII. A dynamical theory of the electromagnetic field," *Phil. Trans. R. Soc.,* vol. 155, 1865.

[16] D. J. Cichon and W. Wiesbeck, "The Heinrich Hertz wireless experiments at Karlsruhe in the view of modern communication," in *Proceedings of the 1995 International Conference on 100 Years of Radio,* 1995, pp. 1-6.

[17] M. N. O. Sadiku, *Principles of Electromagnetics*: Oxford University Press, 2015.

[18] M. Deszcz-Pan, "The Crosswell Electromagnetic Response of Layered Media," University of California, 1994.

[19] M. Wilt, D. L. Alumbaugh, K. H. Lee, M. Deszcz-Pan, H. F. Morrison, and A. Becker, "Crosswell electromagnetic tomography: System design considerations and field results," *Geophysics,* vol. 60, pp. 871-885, 05/01 1995.

[20] K. Vozoff, "THE MAGNETOTELLURIC METHOD IN THE EXPLORATION OF SEDIMENTARY BASINS," *GEOPHYSICS,* vol. 37, pp. 98-141, 1972.

[21] B. R. Spies and T. M. Habashy, "Sensitivity analysis of crosswell electromagnetics," *GEOPHYSICS,* vol. 60, pp. 834-845, 1995.

[22] J. D. Jackson, *Classical Electrodynamics*: John Wiley & Sons Canada, Limited, 1962.

[23] T. L. Chow, *Introduction to Electromagnetic Theory: A Modern Perspective*: Jones and Bartlett Publishers, 2006.

[24] F. Day-Lewis, R. Versteeg, and C. C. Casey, "Object-Based Inversion of Crosswell Radar Tomography Data to Monitor Vegetable Oil Injection Experiments," *Journal of Environmental and Engineering Geophysics - J ENVIRON ENG GEOPHYS,* vol. 9, 06/01 2004.

[25] A. H. Sihvola and I. o. E. Engineers, *Electromagnetic Mixing Formulas and Applications*: Institution of Electrical Engineers, 1999.

[26] S. Al-Anssari, M. Arif, S. Wang, A. Barifcani, and S. Iglauer, "Stabilising nanofluids in saline environments," *Journal of Colloid and Interface Science,* vol. 508, 08/15 2017.

[27] J. C. Bear, B. Yu, C. Blanco-Andujar, P. D. McNaughter, P. Southern, M.-K. Mafina, *et al.*, "A low cost synthesis method for functionalised iron oxide nanoparticles for magnetic hyperthermia from readily available materials," *Faraday Discussions,* vol. 175, pp. 83-95, 2014.

[28] S. Sabale, P. Kandesar, V. Jadhav, R. Komorek, R. K. Motkuri, and X.-Y. Yu, "Recent developments in the synthesis, properties, and biomedical applications of core/shell superparamagnetic iron oxide nanoparticles with gold," *Biomaterials Science,* vol. 5, pp. 2212-2225, 2017.

[29] A. P. LaGrow, M. O. Besenhard, A. Hodzic, A. Sergides, L. K. Bogart, A. Gavriilidis, *et al.*, "Unravelling the growth mechanism of the co-precipitation of iron oxide nanoparticles with the aid of synchrotron X-Ray diffraction in solution," *Nanoscale,* vol. 11, pp. 6620-6628, 2019.

[30] M. Abramoff, P. Magalhães, and S. J. Ram, "Image Processing with ImageJ," *Biophotonics International,* vol. 11, pp. 36-42, 11/30 2003.

[31] A. P. Douvalis, A. Polymeros, and T. Bakas, "IMSG09: A57Fe-119Sn Mössbauer spectra computer fitting program with novel interactive user interface," *Journal of Physics: Conference Series,* vol. 217, p. 012014, 2010/03/01 2010.

[32] J. Baumgartner, A. Dey, P. H. H. Bomans, C. Le Coadou, P. Fratzl, N. A. J. M. Sommerdijk, *et al.*, "Nucleation and growth of magnetite from solution," *Nature Materials,* vol. 12, p. 310, 02/03/online 2013.

[33] S. Iyengar, M. Joy, C. Ghosh, S. Dey, R. K. Kotnala, and D. Ghosh, "Magnetic, X-ray and M ¨ ossbauer studies on magnetite/maghemite core–shell nanostructures fabricated through an aqueous route †," *RSC Advances,* vol. 110, pp. 64919-64929, 11/18 2014.

[34] J. Baltrusaitis and V. H. Grassian, "Surface Reactions of Carbon Dioxide at the Adsorbed Water−Iron Oxide Interface," *The Journal of Physical Chemistry B,* vol. 109, pp. 12227-12230, 2005/06/01 2005.

[35] M. Răcuciu, D. Creanga, and A. Airinei, "Citric-acid-coated magnetite nanoparticles for biological applications," *The European physical journal. E, Soft matter,* vol. 21, pp. 117-21, 11/01 2006.

[36] J. Azadmanjiri, G. Simon, K. Suzuki, C. Selomulya, and J. Cashion, "Phase reduction of coated maghemite (g-Fe 2 O 3) nanoparticles under microwave-induced plasma heating for rapid heat treatment," *Journal of Materials Chemistry,* vol. 22, pp. 617-625, 10/17 2011.

[37] "Chapter Two - Rock Magnetism," in *International Geophysics*. vol. 73, M. W. McElhinny and P. L. McFadden, Eds., ed: Academic Press, 2000, pp. 31-77.

[38] M. M. Barbooti and D. A. Al-Sammerrai, "Thermal decomposition of citric acid," *Thermochimica Acta*, vol. 98, pp. 119-126, 1986/02/01/ 1986.

[39] I. S. Lyubutin, S. S. Starchikov, L. Chun-Rong, N. E. Gervits, N. Y. Korotkov, and T. V. Bukreeva, "Structural and Magnetic Properties of Iron Oxide Nanoparticles in Shells of Hollow Microcapsules Designed for Biomedical Applications," *Croatica Chemica Acta*, vol. 88, pp. 397-403, // 2015.

[40] M. Fardis, A. P. Douvalis, D. Tsitrouli, I. Rabias, D. Stamopoulos, T. Kehagias, *et al.*, "Structural, static and dynamic magnetic properties of dextran coated γ-Fe2O3nanoparticles studied by57Fe NMR, Mössbauer, TEM and magnetization measurements," *Journal of Physics: Condensed Matter*, vol. 24, p. 156001, 2012/03/15 2012.

[41] F. Tournus and A. Tamion, "Magnetic susceptibility curves of a nanoparticle assembly II. Simulation and analysis of ZFC/FC curves in the case of a magnetic anisotropy energy distribution," *Journal of Magnetism and Magnetic Materials*, vol. 323, pp. 1118-1127, 2011/05/01/ 2011.

[42] S. Mørup, M. F. Hansen, and C. Frandsen, "Magnetic interactions between nanoparticles," *Beilstein Journal of Nanotechnology*, vol. 1, pp. 182-190, 2010.

[43] H. Katori and A. Ito, "Experimental Study of the de Almeida-Thouless Line by Using Typical Ising Spin-Glass Fe_xMn_{1-x}TiO₃

with x = 0.41, 0.50, 0.55 and 0.57," *Journal of the Physical Society of Japan,* vol. 63, p. 3122, August 01, 1994 1994.

[44] F. Fabris, K.-H. Tu, C. A. Ross, and W. C. Nunes, "Influence of dipolar interactions on the magnetic properties of superparamagnetic particle systems," *Journal of Applied Physics,* vol. 126, p. 173905, 2019.

[45] C. Djurberg, P. Svedlindh, P. Nordblad, M. Hansen, F. Bødker, and S. Mørup, "Dynamics of an Interacting Particle System: Evidence of Critical Slowing Down," *Physical Review Letters,* vol. 79, 01/22 1997.

[46] M. Satake, Y. Hayashi, Y. Mido, S. A. Iqbal, and M. S. Sethi, *Colloidal and Surface Chemistry*: Discovery Publishing House, 1996.

[47] P. Hiemenz and R. Rajagopalan, *Principles of Colloid and Surface Chemistry,* Third Edition ed.: CRC Press, 1997.

[48] E. Matijevic and R. J. Good, *Surface and Colloid Science*: Springer US, 2012.

[49] D. F. Evans and H. Wennerström, *The Colloidal Domain: Where Physics, Chemistry, Biology, and Technology Meet*: Wiley, 1999.

[50] K. S. Birdi, *Handbook of Surface and Colloid Chemistry, Third Edition*: CRC Press, 2008.

[51] E. Hotze, T. Phenrat, and G. Lowry, "Nanoparticle Aggregation: Challenges to Understanding Transport and Reactivity in the Environment," *Journal of environmental quality,* vol. 39, pp. 1909-24, 11/01 2010.

[52] J. García-Otero, M. Porto, J. Rivas, and A. Bunde, "Influence of Dipolar Interaction on Magnetic Properties of Ultrafine Ferromagnetic Particles," *Physical review letters,* vol. 84, pp. 167-70, 02/01 2000.

[53] H. C. Hamaker, "The London—van der Waals attraction between spherical particles," *Physica,* vol. 4, pp. 1058-1072, 1937/10/01/ 1937.

[54] P. Somasundaran, *Encyclopedia of Surface and Colloid Science*: Taylor & Francis, 2006.

[55] M. Kaszuba, M. Connah, F. McNeil-Watson, and U. Nobbmann, "Resolving Concentrated Particle Size Mixtures Using Dynamic Light Scattering," *Particle & Particle Systems Characterization,* vol. 24, pp. 159-162, 09/01 2007.

[56] H. Holthoff, S. U. Egelhaaf, M. Borkovec, P. Schurtenberger, and H. Sticher, "Coagulation Rate Measurements of Colloidal Particles by Simultaneous Static and Dynamic Light Scattering," *Langmuir,* vol. 12, pp. 5541-5549, 1996/01/01 1996.

[57] S. E. Mylon, K. L. Chen, and M. Elimelech, "Influence of Natural Organic Matter and Ionic Composition on the Kinetics and Structure of Hematite Colloid Aggregation: Implications to Iron Depletion in Estuaries," *Langmuir,* vol. 20, pp. 9000-9006, 2004/10/01 2004.

[58] W. Sun, L. Wang, Z. Yang, T. Zhu, T. Wu, C. Dong, *et al.*, "Tuning the Oxidation Degree of Graphite toward Highly Thermally Conductive Graphite/Epoxy Composites," *Chemistry of Materials,* vol. 30, pp. 7473-7483, 2018.

[59] P. J. Vikesland, R. L. Rebodos, J. Y. Bottero, J. Rose, and A. Masion, "Aggregation and sedimentation of magnetite nanoparticle clusters," *Environmental Science: Nano,* vol. 3, pp. 567-577, 2016.

[60] M. L. Bruschi and L. d. A. S. de Toledo, "Pharmaceutical Applications of Iron-Oxide Magnetic Nanoparticles," *Magnetochemistry,* vol. 5, p. 50, 2019.

[61] T. Phenrat, N. Saleh, K. Sirk, R. D. Tilton, and G. V. Lowry, "Aggregation and Sedimentation of Aqueous Nanoscale Zerovalent Iron Dispersions," *Environmental Science & Technology,* vol. 41, pp. 284-290, 2007/01/01 2007.

[62] H. Tsurusawa, M. Leocmach, J. Russo, and H. Tanaka, "Direct link between mechanical stability in gels and percolation of isostatic particles," *Science Advances,* vol. 5, p. eaav6090, 2019.

[63] R. Nasralla, E. Sergienko, S. Masalmeh, H. Linde, N. Brussee, H. Mahani, *et al.*, "Potential of Low-Salinity Waterflood to Improve Oil Recovery in Carbonates: Demonstrating the effect by Qualitative Coreflood (SPE-172010-PA)," *SPE Journal,* vol. 21, 10/01 2016.